4-11-2024 2:00 PM

The Black-to-White Hole Transition

Farshid Soltani, *Western University*

Supervisor: Vidotto, Francesca, *The University of Western Ontario*
: Christensen, Dan, *The University of Western Ontario*

A thesis submitted in partial fulfillment of the requirements for the Doctor of Philosophy degree in Physics

Recommended Citation

Soltani, Farshid, "The Black-to-White Hole Transition" (2024). *Electronic Thesis and Dissertation Repository*. 10049.
https://ir.lib.uwo.ca/etd/10049

Abstract

Classically, an isolated black hole is a stable gravitational object. If however semiclassical effects are taken into account, an isolated black hole can be shown to slowly radiate its mass away in a process called evaporation. At the end of the evaporation process, when the size of the horizon becomes Planckian, the quantum nature of the gravitational field can no longer be neglected and the dynamics of the horizon is governed by quantum gravity. The main objective of this thesis is the systematic investigation of a tentative scenario for the "end of the life" of a black hole: the black-to-white hole transition.

Starting from the classical Oppenheimer-Snyder model, which is the simplest model of black hole formation by gravitational collapse, an effective metric that takes into account first-order quantum gravitational effects is derived using loop quantum gravity. In the resulting spacetime, the star undergoes a "bounce" at the end of its collapse and the interior trapped geometry of the black hole smoothly transitions into the anti-trapped geometry of the interior of a white hole. A natural assumption is then that, at the end of the evaporation process, the horizon of the black hole undergoes a quantum (tunneling) transition from trapping to anti-trapping consistently with the transition of geometry taking place in the interior of the hole. In this thesis, I construct and analyze a concrete effective metric describing the entire spacetime of this scenario, known as the black-to-white hole transition. This is a result of fundamental importance in improving our understanding of the physics of this phenomenon.

The quantum tunneling transition of the horizon in this scenario is a non-perturbative phenomenon that can only be studied using a background-independent theory of quantum gravity. I show that the covariant formulation of loop quantum gravity, also known as spin foam formalism, provides a clear framework to investigate this phenomenon and I compute the spin foam transition amplitude associated with it. A thorough investigation of this transition amplitude, which is currently out of reach due to the severe complexity of the latter, would allow us to give definitive answers to the remaining open questions about the black-to-white hole transition scenario.

Keywords: Black holes, white holes, horizons, Oppenheimer-Snyder model, quantum gravity, loop quantum gravity, spin foams.

Summary for Lay Audience

There is evidence in the sky of the presence of a huge number of black holes. We even took a few good pictures of them. However, it is surprising how much we still do not know or understand about them. Intuitively, a black hole is a region of spacetime where space is falling faster than the speed of light, and anything that tries to move outwards is nonetheless carried inwards by the faster-than-light inflow of space. This means that nothing can escape a black hole, not even light. This is bizarre. But it is not even its oddest feature. Black holes are formed when massive enough stars at the end of their life, that is when the nuclear reactions in their interior stop, collapse under their own gravitational force. After a black hole is formed, the star keeps collapsing until all of its mass is concentrated in a single point of infinite density. "Infinity" is a mathematical concept that has no counterpart in the physical world and it should not be predicted for any physical quantity. This point is then called a "singular" point of spacetime and it is taken to signal the breakdown of the classical theory of gravity.

However, the big revolution of modern physics of the twentieth century taught us that the microscopic world does not follow the (deterministic) rules of classical physics, but it actually follows the (probabilistic) rules of a new theory called quantum physics. The theory describing the quantum rules of the gravitational field is called quantum gravity, and we still do not have a complete understanding of it. Using a specific tentative theory of quantum gravity known as loop quantum gravity, I re-investigate the collapse of a star and the subsequent formation of a black hole in a quantum context. What I find is that the collapse of the star does not end in a singular point of infinite density anymore, but it reaches instead a point of maximum, but finite, density after which the star "bounces" and starts to expand. Furthermore, consistently with the bounce of the star, the black hole transitions into a white hole. The latter is the "opposite" of a black hole: a white hole is a region of spacetime where space is expanding faster than the speed of light, and so everything in its interior is bound to come out of it. I then compute the quantum probability for this process to take place.

Co-Authorship Statement

The original work presented in this thesis is based on the following published articles:

[1] F. Soltani. “Global Kruskal-Szekeres coordinates for Reissner–Nordström spacetime”. *Phys. Rev. D* **108** (2023), 124002. DOI: `10.1103/PhysRevD.108.124002.` Copyright © 2023 by American Physical Society. All rights reserved.

[2] M. Han, C. Rovelli and F. Soltani. “Geometry of the black-to-white hole transition within a single asymptotic region”. *Phys. Rev. D* **107** (2023), 064011. DOI: `10.1103/PhysRevD.107.064011.` Copyright © 2023 by American Physical Society. All rights reserved.

[3] F. Fazzini, C. Rovelli and F. Soltani. “Painlevé-Gullstrand coordinates discontinuity in the quantum Oppenheimer-Snyder model”. *Phys. Rev. D* **108** (2023), 044009. DOI: `10.1103/PhysRevD.108.044009.` Copyright © 2023 by American Physical Society. All rights reserved.

[4] F. D’Ambrosio, M. Christodoulou, P. Martin-Dussaud, C. Rovelli and F. Soltani. “End of a black hole’s evaporation”. *Phys. Rev. D* **103** (2021), 066015. DOI: `10.1103/PhysRevD.103.106014.` Copyright © 2021 by American Physical Society. All rights reserved.

[5] F. Soltani, C. Rovelli and P. Martin-Dussaud. “End of a black hole’s evaporation. II”. *Phys. Rev. D* **104** (2021), 106014. DOI: `10.1103/PhysRevD.104.066015.` Copyright © 2021 by American Physical Society. All rights reserved.

For each co-authored paper I will give a detail of the breakdown of duties between the following four categories: conceptualization, writing first draft, writing final draft, and formal analysis.

Article [2] has been published in collaboration with Dr. Muxin Han and Dr. Carlo Rovelli. The duties breakdown was: conceptualization (Han, Rovelli, Soltani), writing first draft (Rovelli), writing final draft (Han, Rovelli, Soltani), and formal analysis (Han, Rovelli, Soltani).

Article [3] has been published in collaboration with Mr. Francesco Fazzini and Dr. Carlo Rovelli. The duties breakdown was: conceptualization (Fazzini, Rovelli, Soltani), writing first draft (Soltani), writing final draft (Fazzini, Rovelli, Soltani), and formal analysis (Soltani).

Article [4] has been published in collaboration with Dr. Marios Christodoulou, Dr. Fabio D'Ambrosio, Dr. Pierre Martin-Dussaud, and Dr. Carlo Rovelli. The duties breakdown was: conceptualization (Christodoulou, D'Ambrosio, Martin-Dussaud, Rovelli, Soltani), writing first draft (Christodoulou, D'Ambrosio, Martin-Dussaud), writing final draft (Christodoulou, D'Ambrosio, Martin-Dussaud, Rovelli, Soltani), and formal analysis (Christodoulou, D'Ambrosio, Martin-Dussaud, Rovelli, Soltani).

Article [5] has been published in collaboration with Dr. Pierre Martin-Dussaud and Dr. Carlo Rovelli. The duties breakdown was: conceptualization (Martin-Dussaud, Rovelli, Soltani), writing first draft (Soltani), writing final draft (Martin-Dussaud, Rovelli, Soltani), and formal analysis (Soltani).

Acknowledgements

I would like to express my sincere gratitude to the following people who, in one way or another, helped me along the way. I have been fortunate enough to be surrounded by generous and caring people and I am tremendously grateful for all the help I received.

First and foremost, I wish to thank my thesis supervisors, Francesca and Dan, for their support and their invaluable guidance throughout this project and academic life in general. They are not only accomplished researchers but also wonderful people and I have been very lucky to have them as supervisors. I want to thank Carlo, my main collaborator in this project, for his help, for the endless sessions in front of a whiteboard we spent together, and for his genuine enthusiasm for the project.

I am extremely grateful to to my parents, Stefania and Hashem, whose many sacrifices have not been unnoticed, to my brother, Saman, for being a constant example and for setting the bar so high, and to my whole family for always being there for me. I am particularly indebted to my aunt and uncle, Sharareh and Kamran, for taking me in and spoiling me during Covid.

Elena deserves a special mention: she is my number one supporter and she has always been there for me when I needed it. Thank you for being my muse, proofreader, and best friend. But most of all, thank you for making me happy.

Last but not least, I wish to thank Adrien, Aishwarya, Alan, Alex, Alexis, Almu, Amgad, Annika, Anusha, Athanasios, Bavithra, Carlos, Charlotte, Charmi, Chiara, Chris, Daytn, Deepa, Diego, Dilanjan, Dongxue, Eleonora, Emily, Emmanuel, Enzo, Erwan, Ethan, Eugenia, Eva, Fabio, Gabriel, George, Ghazal, Hadi, Hannah, Homa, James, Jamie, Jared, Kasia, Katharina, Kundan, Iain, Indrani, Louis, Maddalena, Mark, Mateo, Matheus, Matteo, Max, Megan, Michaela, Mohammed, Nadia, Navid, Niels, Niloufar, Pascal, Peeyush, Pe-

ter, Pietro, Pietropaolo, Priya, Ramtin, Roberto, Sheyda, Shubhankar, Shuwei, Sina, Sofie, Teagen, Varun, Victor, Victoria, Yasamin, Yichen, Yifey, and Yung for making this journey unforgettable.

Table of Contents

List of Figures

Chapter 1

Introduction

There is evidence in the sky of the presence of a huge number of black holes. The prototypical example of black hole formation by gravitational collapse is the Oppenheimer-Snyder model, which predicts that a black hole horizon is formed once a star collapses within its own Schwarzschild radius. After that, the collapsing matter reaches Planckian densities in a short proper time. What happens next is outside the reach of general relativity, as it involves the quantum behavior of the gravitational field in the strong field regime. The quantum physics of the gravitational field is however relevant not only for the interior of a black hole but also for its exterior. Hawking in fact famously showed that black holes slowly radiate their mass away in a process called evaporation. When the mass of the black hole becomes Planckian, quantum gravitational effects around its horizon can no longer be neglected and the physics of the horizon must now be described using quantum gravity.

The quantum physics of the interior of the black hole can be studied using loop quantum gravity. The resulting quantum-corrected Oppenheimer-Snyder model predicts a "bounce" of the star at the end of its collapse, followed by a phase of expansion, and a smooth non-singular transition of the interior trapped geometry of the black hole into the anti-trapped geometry of the interior of a white hole. This model however does not take into account the quantum physics of the horizon. A natural assumption is that, at the end of the evaporation process, the horizon of the black hole undergoes a quantum (tunneling) transition from trapping to anti-trapping consistently with the transition of geometry taking place in the interior of the hole. In this scenario, known as the *black-to-white hole transition*, the black hole evolves into a white hole "remnant" living in the future of the parent black hole, in its same asymptotic region and location.

Confusing coordinate artifacts are common in general relativity and working in a specific coordinate system can thus be deceiving, especially in an "effective" context where the spacetime metric is corrected to take into account first-order quantum effects. Being able to keep track of the causal and global structure of spacetime becomes then very important. Luckily, there is an incredibly powerful tool to do just that: the Carter-Penrose diagram of spacetime. In section 1.1 I introduce the theory of Carter-Penrose diagrams starting from Minkowski spacetime and then moving on to a class of spacetimes, known as strongly spherically symmetric spacetimes, that will be particularly relevant for the description of black holes. These diagrams will be instrumental in the construction and in the understanding of the black-to-white hole transition.

In section 1.2 I introduce the concepts of black holes and white holes and I review all the properties of these objects that will be useful for the construction of the black-to-white hole spacetime. All the work presented in this thesis is carried out under the simplifying assumption of spherical symmetry. While astrophysical black holes do rotate, the spherically symmetric scenario provides a good testing ground to formulate the black-to-white hole paradigm and investigate its physics. A spherically symmetric and uncharged black hole is described by Schwarzschild spacetime. The Oppenheimer-Snyder model describes the formation of a Schwarzschild black hole by gravitational collapse of a spherical ball of uniform density with no pressure. I will examine the evaporation process of black holes and give a brief overview of the resulting information-loss paradox pointing out how the black-to-white hole transition fits in the discussion. Finally, I identify the three physically distinct regions of spacetime where quantum gravitational effects cannot be neglected and where therefore the classical theory is no longer reliable.

The quantum physics of the gravitational field will be explored using loop quantum gravity, a tentative theory for the quantization of general relativity. A minimal introduction to the salient features of the theory needed to understand the analysis of the black-to-white hole transition is given in section 1.3. I introduce the canonical formulation of the theory and the spin-network states, which are quantum states of the gravitational field with a particularly simple and suggestive physical interpretation. I then use the canonical theory to heuristically construct a path integral formulation of the theory, also known as covariant loop quantum gravity, which is later properly defined in the context of spin foam models.

This concludes the review of the background material and brings us to the original work presented in this thesis. In chapter 2 I construct a global Kruskal-Szekeres coordinate chart for strongly spherically symmetric spacetimes using Reissner-Nordström spacetime as a working example. These coordinates will be used to draw the Carter-Penrose diagrams of the quantum-corrected Oppenheimer-Snyder model and the black-to-white hole spacetime, whose construction, together with the investigation of their physics, is given in chapter 3. The analysis of the quantum physics of the horizon tunneling region in the black-to-white hole spacetime is performed in chapter 4 using covariant loop quantum gravity.

1.1 Carter-Penrose diagrams

In general relativity *spacetime* is a pair $(\mathscr{M}, \boldsymbol{g})$, where $\mathscr{M}$ is a smooth four-dimensional manifold and $\boldsymbol{g}$ is a Lorentzian metric of $(-,+,+,+)$ signature on $\mathscr{M}$. Coordinates on $\mathscr{M}$ are labeled as x, where $x = (x^0, x^1, x^2, x^3) = (x^\mu)$.

All the geometric information of spacetime (e.g. distances, angles, volumes, etc.) and its causal structure are encoded in the metric tensor $\boldsymbol{g}$. For instance, the square of the distance $\mathrm{d}s$ between two infinitesimally closed points $p = (x^0, x^1, x^2, x^3)$ and $p' = (x^0 + \mathrm{d}x^0, x^1 + \mathrm{d}x^1, x^2 + \mathrm{d}x^2, x^3 + \mathrm{d}x^3)$ is given by the so-called *line element*

$$\mathrm{d}s^2 = g_{\mu\nu}\, \mathrm{d}x^\mu\, \mathrm{d}x^\nu\, . \tag{1.1}$$

This information, especially the causal structure of spacetime, is however not readily discernible just by looking at the different metric components in general. The ability to visualize such information is then crucial to help the physical intuition.

Being spacetime a curved four-dimensional manifold, this is clearly not an easy task. It turns out however that for highly symmetric situations, like spherically symmetric spacetimes, there is a tremendously powerful tool called *Carter-Penrose diagram*, or conformal diagram, that provides the desired visual representation of spacetime. There is no unique and agreed-upon definition of a Carter-Penrose diagram. And in most cases, such a definition is not really needed. I will take the point of view that Carter-Penrose diagrams are genuine spacetime diagrams that are drawn in particularly advantageous coordinates. I will comment on different definitions later on. These diagrams were born out of Penrose's idea [6] of using conformal transformations to map the regions of spacetime at coordinate "infinity" into a hypersurface at a finite coordinate position whose properties could then be studied locally. Carter [7] soon realized that the same techniques could be used to effectively visualize the causal and global structure of spacetime.

I will discuss the Carter-Penrose diagram techniques only for the class of spacetimes whose line element can be locally written as

$$\mathrm{d}s^2 = -f(r)\,\mathrm{d}t^2 + f^{-1}(r)\,\mathrm{d}r^2 + r^2\,\mathrm{d}\Omega^2\,, \tag{1.2}$$

where $\mathrm{d}\Omega^2 = \mathrm{d}\theta^2 + \sin^2\theta\,\mathrm{d}\phi^2$ is the metric of a unit two-sphere and $f(r)$ is the function characterizing the different spacetimes in this class. These spacetimes are clearly spherically symmetric, but they also possess an additional Killing vector field ∂_t normal to the angular directions. This is the reason why $f(r)$ is a function of the radius only. The coordinate system (t, r, θ, ϕ) is the spherical coordinate system adapted to observers moving along the Killing vector field ∂_t.

Following the nomenclature in Schindler [8] I will refer to these spacetimes as *strongly spherically symmetric spacetimes*. Carter-Penrose diagram techniques can be applied to a larger class of spacetimes. However, only the strongly spherically symmetric spacetimes will be relevant for the work presented in this thesis. I will furthermore assume $f(r)$ to be a C^1 function in $r \in (0, +\infty)$ with a finite number of isolated zeroes.

1.1.1 Minkowski spacetime

Before discussing the general case, it is useful to introduce these techniques in a simple case to lay the groundwork. Consider then Minkowski spacetime in spherical coordinates

$$\mathrm{d}s^2 = -\,\mathrm{d}t^2 + \mathrm{d}r^2 + r^2\,\mathrm{d}\Omega^2\,, \tag{1.3}$$

where the speed of light c has been set to $c = 1$. Comparison with eq. (1.2) clearly shows that Minkowski spacetime can be seen as the strongly spherically symmetric spacetime characterized by the function $f(r) = 1$.

The local causal structure of spacetime is visually represented by the light cones. Minkowski spacetime in (t, r, θ, ϕ) coordinates has the very nice property of having radial light cones tilted at $\pm 45°$. Namely, radial null geodesics satisfy $\mathrm{d}r/\,\mathrm{d}t = \pm 1$, making the causal structure of the spacetime readily apparent in a spacetime diagram. This is the first fundamental property that a Carter-Penrose diagram must satisfy.

The second fundamental property that a Carter-Penrose diagram must implement is to bring regions of spacetime at coordinate “infinity” to a finite position on the diagram. This allows the entire spacetime to be seen at once. The second requirement is easily accomplished by mapping the original infinite coordinate interval into a finite interval using any monotonic bounded function. The standard function for the job is the inverse tangent. However, a direct application of this transformation does not ensure the light cone condition to be, or even to remain, satisfied. The change of coordinates

$$\tilde{t} = \tan^{-1}(t)\,, \qquad \tilde{r} = \tan^{-1}(r)\,, \tag{1.4}$$

does indeed map the original infinite coordinate intervals

$$-\infty < t < +\infty\,, \qquad 0 < r < +\infty\,, \tag{1.5}$$

to the finite intervals

$$-\pi/2 < \tilde{t} < \pi/2\,, \qquad 0 < \tilde{r} < \pi/2\,, \tag{1.6}$$

but the radial light cones now satisfy $\mathrm{d}\tilde{r}/\,\mathrm{d}\tilde{t} = \pm\cos^2\tilde{r}/\cos^2\tilde{t} \neq \pm 1$. A spacetime diagram in these coordinates would thus allow the entire spacetime to be seen at once. But the light cone tilting at different points in the diagram, and with it the causal structure of spacetime, would not be discernible.

The way to satisfy both conditions at the same time is to change to coordinates adapted to the radial null geodesics before mapping coordinate "infinity" to a finite position. Radial null geodesics in Minkowski spacetime are given by the curves

$$t - r = u, \qquad t + r = v\,, \tag{1.7}$$

where u and v are constants identifying respectively the different outgoing and ingoing geodesics. If eq. (1.7) is then interpreted as a change of coordinates from (t, r) to (u, v), the line element becomes

$$\mathrm{d}s^2 = -\,\mathrm{d}u\,\mathrm{d}v + r^2(u,v)\,\mathrm{d}\Omega^2\,, \tag{1.8}$$

with $r(u,v) = (v-u)/2$, and the coordinate intervals reads

$$-\infty < u < +\infty\,, \qquad -\infty < v < +\infty\,, \qquad u \leq v\,. \tag{1.9}$$

From the expression of the line element in eq. (1.8) it is clear that the coordinate basis vectors ∂_u and ∂_v are null. Radial null geodesics are now given by the solutions of the equation $\dot{u}\dot{v} = 0$.

Interestingly, the "*double-null*" form of the metric in eq. (1.8), and with it the relationship of the coordinates with the radial light cone structure, is preserved under arbitrary transformations

$$u = u(\tilde{u})\,, \qquad v = v(\tilde{v})\,. \tag{1.10}$$

This means that the inverse tangent mapping to bring "infinity" to a finite position can be applied to these coordinates without messing up the lightcone structure. Consider in fact the change of coordinate

$$U = \tan^{-1}(u)\,, \qquad V = \tan^{-1}(v)\,, \tag{1.11}$$

resulting in the following coordinate intervals:

$$-\pi/2 < U < \pi/2\,, \qquad -\pi/2 < V < \pi/2\,, \qquad U \leq V\,. \tag{1.12}$$

The line element in these coordinates reads

$$\mathrm{d}s^2 = \frac{1}{4\cos^2(U)\cos^2(V)}\Bigg[-4\,\mathrm{d}U\,\mathrm{d}V + \sin^2(V-U)\,\mathrm{d}\Omega^2\Bigg]\,. \tag{1.13}$$

The entire spacetime has been once again mapped to a finite coordinate region. But this time the light cone structure has not been altered: radial null geodesics are still given by the solutions of the equation $\dot{U}\dot{V} = 0$. To see this more clearly, it is possible to define new temporal and spatial coordinates (T, R) via the change of coordinates

$$T = U + V, \qquad R = V - U\,, \tag{1.14}$$

resulting in the new coordinate intervals

$$|T| + R < \pi\,, \qquad 0 \leq R < \pi\,. \tag{1.15}$$

The line element becomes

$$\mathrm{d}s^2 = (\cos T + \cos R)^{-2}\Bigg[-\mathrm{d}T^2 + \mathrm{d}R^2 + \sin^2 R\,\mathrm{d}\Omega^2\Bigg]\,, \tag{1.16}$$

giving radial null geodesics satisfying $\mathrm{d}R/\,\mathrm{d}T = \pm 1$ as required.

The final step to draw the Carter-Penrose diagram of the spacetime is to suppress the angular coordinates. The idea behind this is that by restricting the attention to spherically symmetric spacetimes and working in angular coordinates adapted to this symmetry, the angular information of the metric can be safely neglected without compromising the global and causal structure of spacetime. A two-dimensional projection $\mathrm{d}\bar{s}^2$ of the line element in eq. (1.16) over the space perpendicular to the angular directions can be simply defined as

$$\mathrm{d}\bar{s}^2 = (\cos T + \cos R)^{-2}\Big[-\mathrm{d}T^2 + \mathrm{d}R^2\Big]\,. \tag{1.17}$$

The Carter-Penrose diagram of Minkowski spacetime, represented in fig. 1.1, is the genuine spacetime diagram of the metric in eq. (1.17). Let me briefly unpack all the information contained in this diagram. Minkowski spacetime is represented by the interior of this funny-looking triangle. All points in the diagram, except the ones at $r = 0$, represent two-spheres in Minkowski spacetime with radius $r(T, R) = \sin R/(\cos T + \cos R)$. Radial null geodesics and light cones are everywhere given by straight lines at ±45°. The radial light cones along a curve of constant radius r are shown in red in fig. 1.1. The boundary of the diagram, except for the vertical line representing $r = 0$, is not part of Minkowski spacetime. This boundary can however be given a clear physical interpretation in terms of the "infinities" of the spacetime in the original coordinates:

i^+ (*future timelike infinity*) is the region of spacetime where curves of constant radius r (in violet in fig. 1.1) asymptote to for $t \to +\infty$.
$i^+ = \{(T, R) = (\pi, 0)\}$.

i^- (*past timelike infinity*) is the region of spacetime where curves of constant radius r (in violet in fig. 1.1) asymptote to for $t \to -\infty$.
$i^- = \{(T, R) = (-\pi, 0)\}$.

i^0 (*spacelike infinity*) is the region of spacetime where curves of constant time t (in light blue in fig. 1.1) asymptote to for $r \to +\infty$.
$i^0 = \{(T, R) = (0, \pi)\}$.

$\mathscr{I}^+$ (*future null infinity*, $T + R = \pi$ and) is the region of spacetime where outgoing radial light rays (null geodesics) asymptote to in the future, that is $t, r \to +\infty$ at constant u.
$\mathscr{I}^+ = \{(T, R) : T + R = \pi, 0 < R < \pi\}$.

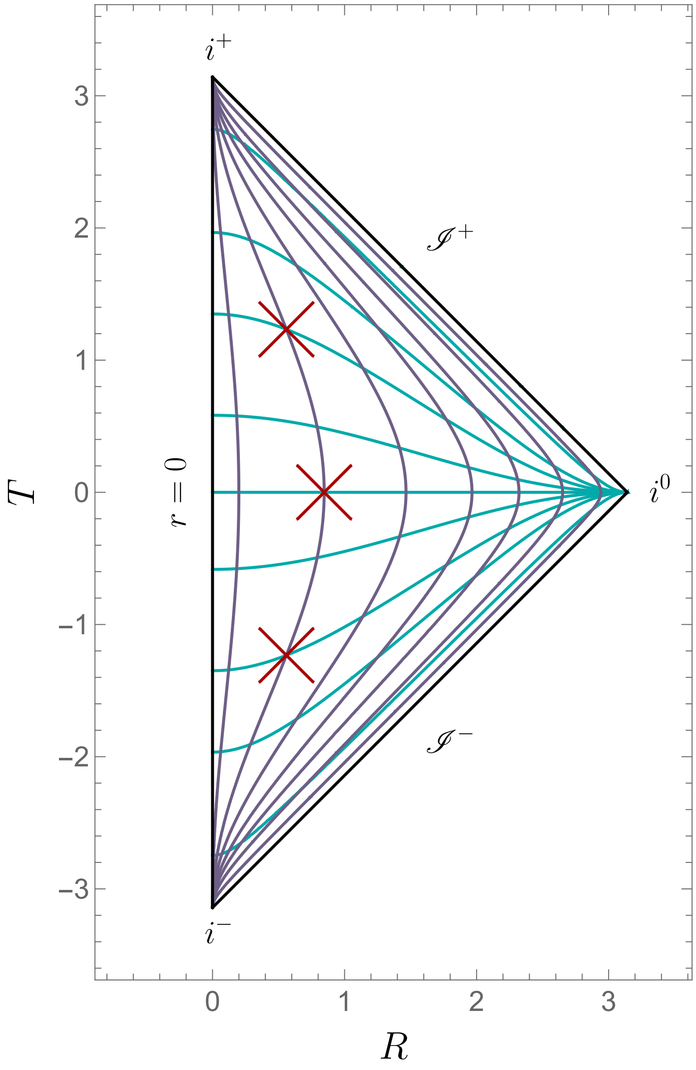

Figure 1.1: Carter-Penrose diagram of Minkowski spacetime. In light blue curves of constant t, in violet curves of constant r, and in red light cones along a curve of constant r.

$\mathscr{I}^-$ (*past null infinity*) is the region of spacetime where ingoing radial light rays (null geodesics) asymptote to in the past, that is $t \to -\infty$ and $r \to +\infty$ at constant v.
$\mathscr{I}^- = \{(T, R) : T - R = -\pi, 0 < R < \pi\}$.

All timelike geodesics begin at i^- and end at i^+. All spacelike geodesics begin at i^0, are "reflected" at $r = 0$ and end again at i^0. All null geodesics begin at $\mathscr{I}^-$, are "reflected" at $r = 0$, and end at $\mathscr{I}^+$. Notice however that also non-geodesic timelike curves can begin or end at respectively $\mathscr{I}^-$ and $\mathscr{I}^+$. An example of such a curve is the wordline of a uniformly accelerated observer. Furthermore, only radial null geodesics are given by straight lines at ±45°. Non-radial null geodesics with angular momentum will look like timelike curves in a Carter-Penrose diagram.

The Carter-Penrose diagram provides a clever visual representation of Minkowski spacetime in its entirety. The causal structure of the spacetime is readily apparent, albeit this was true also in the original (t, r) coordinates, and its global structure is easily accessible at a finite coordinate distance. Being Minkowski spacetime quite trivial (and dull), nothing new about it is uncovered by this construction. The latter will however prove tremendously useful in more complex settings.

A concept that will come in handy in the discussion of black holes is the one of *asymptotically flat spacetimes*. The idea behind the definition of this class of spacetimes is quite straightforward: an asymptotically flat spacetime is a spacetime whose asymptotic behavior at "infinity" is similar to the behavior of Minkowski spacetime. The mathematically rigorous implementation of this idea is however not as straightforward and I will not discuss it. It can be found in Frolov and Novikov [9]. Nevertheless, it is reasonable to assume that whatever the exact definition is, it will result in a class of spacetimes whose Carter-Penrose diagram has the same boundary structure as the Carter-Penrose diagram of Minkowski spacetime in fig. 1.1. I will heuristically use 'asymptotically flat spacetime' to mean exactly this in the following.

Before moving on to the general case, let me comment on the structure of the metrics in eqs. (1.16) and (1.17). Defining a new line element

$$\mathrm{d}\tilde{s}^2 = -\,\mathrm{d}T^2 + \mathrm{d}R^2 + \sin^2 R\,\mathrm{d}\Omega^2\,, \tag{1.18}$$

eq. (1.16) can be rewritten as

$$\mathrm{d}s^2 = \omega^2(T,R)\,\mathrm{d}\tilde{s}^2 \tag{1.19}$$

with $\omega(T,R) = (\cos T + \cos R)^{-1}$. That is, the two different metrics defined by $\mathrm{d}s^2$ and $\mathrm{d}\tilde{s}^2$ are related by a conformal transformation of parameter $\omega(T,R)$. Conformal transformations are particularly useful because they "preserve the causal structure of spacetime": They leave angles between any two vectors invariant under the transformation. In particular, a null curve as defined by the original metric is mapped into a null curve as defined by the conformally related metric.

Thus, if the interest of this construction is only in the causal and global structure of spacetime, the Carter-Penrose diagram in fig. 1.1 can be seen as the spacetime diagram of the two-dimensional projection of the unphysical metric defined in eq. (1.18). The diagram looks exactly the same, but the prefactor $\omega^2(T,R)$ has now been dropped. This simple step has profound consequences for the boundary structure of the diagram. When interpreted as the diagram of Minkowski spacetime written in (T,R) coordinates, the boundary of the Carter-Penrose diagram in fig. 1.1 is not part of spacetime. The conformal factor $\omega(T,R)$ in eq. (1.19) is in fact divergent as the boundary is approached, consistently with the fact that "infinity" is an infinite proper distance away even though it is at finite coordinate distance. The boundary is however a perfectly well-defined hypersurface with respect to the metric $\mathrm{d}\tilde{s}^2$, and it can thus be added to spacetime in this new interpretation of the diagram. The union of the original spacetime and the boundary, usually called *conformal boundary* in this context, is referred to as *conformal compactification* of spacetime, and its diagram is called conformal diagram.

The (conformal) properties of "infinity" and the asymptotic properties of fields there can now be studied locally in the conformal compactification of spacetime. While a very powerful technique, it will be of no use in the following. Furthermore, this interpretation of Carter-Penrose diagrams is strictly dependent on the form of the spacetime metric obtained in eq. (1.16). For more complicated spacetimes, coordinates satisfying the two conditions required for obtaining a Carter-Penrose diagram will not in general also provide an expression for the spacetime metric in terms of a well-defined conformally related metric.[1] For these reasons, I will consider Carter-Penrose diagrams as genuine diagrams of physical spacetime in convenient coordinates and conformal infinity to not be part of spacetime.

1.1.2 Strongly spherically symmetric spacetimes

I will now sketch the steps for the construction of Carter-Penrose diagrams for strongly spherically symmetric spacetimes. The actual construction of specific diagrams will be performed case by case in the following sections. The metric of a strongly spherically symmetric spacetime can be locally written as

$$\mathrm{d}s^2 = -f(r)\,\mathrm{d}t^2 + f^{-1}(r)\,\mathrm{d}r^2 + r^2\,\mathrm{d}\Omega^2 \tag{1.20}$$

in spherical coordinates (t, r, θ, ϕ) adapted to the Killing vector field ∂_t. This coordinate system is ill-defined wherever the defining function $f(r)$ has a zero. For Minkowski spacetime, where $f(r) = 1$ has no zeroes, the coordinate system (t, r, θ, ϕ) covers the entire spacetime. For a generic $f(r)$ having a finite number N of isolated zeroes at r_i, $i = 1, 2, \ldots, N$, the coordinate system (t, r, θ, ϕ) can be used to separately cover all regions of spacetime such that

$$-\infty < t < +\infty\,, \qquad r_j < r < r_{j+1}\,, \tag{1.21}$$

where $j = 0, 1, \ldots, N$ and I set $r_0 = 0$ and $r_{N+1} = +\infty$.

Notice that t is a timelike coordinate and r is a spacelike coordinate in

---

[1] This is however always possible for the two-dimensional projection of the metric on the space perpendicular to the angular directions. The two-dimensional projection of the metric is always conformally related to two-dimensional Minkowski spacetime

all the spacetime regions where $f(r) > 0$. In these regions the Killing vector field ∂_t is timelike and the metric is static. However, in the spacetime regions where $f(r) < 0$ the coordinate t is spacelike and the coordinate r is timelike. In these regions, the Killing vector field ∂_t is thus spacelike and the metric is homogeneous but neither static nor stationary.

A Carter-Penrose diagram for this spacetime is a genuine spacetime diagram drawn in particular coordinates satisfying the following two properties:

1. The radial light cones are tilted at ±45°.

2. Spacetime "infinity" is at a finite coordinate position.

The analysis of Minkowski spacetime showed that the implementation of the second desideratum is quite straightforward. Any mapping under a monotonic bounded function will do the job. However, the implementation of both desiderata at the same time is trickier. An intermediate step that often proves to be useful is to rewrite the metric in double-null form by using coordinates that are adapted to the radial null geodesics. Radial null geodesics in strongly spherically symmetric spacetimes satisfy the equations

$$\frac{\mathrm{d}t}{\mathrm{d}r} = \pm\frac{1}{f(r)}\,. \tag{1.22}$$

Defining the *tortoise coordinate* $r_*(r)$ as

$$r_*(r) = \int \frac{\mathrm{d}r}{f(r)}\,, \tag{1.23}$$

radial null geodesics take the form

$$t - r_*(r) = u\,, \qquad\qquad t + r_*(r) = v\,, \tag{1.24}$$

where u and v are constants identifying respectively the different outgoing and ingoing geodesics.

When promoted to coordinates, u and v are usually referred to respectively as the retarded and the advanced time coordinates. Changing from (t, r, θ, ϕ) coordinates to (v, r, θ, ϕ) coordinates, also known as ingoing Eddington-Finkelstein coordinates [10, 11], the metric becomes

$$\mathrm{d}s^2 = -f(r)\,\mathrm{d}v^2 + 2\,\mathrm{d}v\,\mathrm{d}r + r^2\,\mathrm{d}\Omega^2\,. \tag{1.25}$$

Being the metric independent from the coordinate v, it is clear that the non-spherical Killing vector field is given by ∂_v in these coordinates. Furthermore, this metric is non-singular and non-degenerate for all $r > 0$, thus showing that the singularities of the metric in eq. (1.20) for $f(r) = 0$ are just coordinate singularities. This also means that ingoing Eddington-Finkelstein coordinates cover all spacetime regions such that

$$-\infty < v < +\infty\,, \qquad 0 < r < +\infty\,. \tag{1.26}$$

It would be tempting to say that these coordinates cover the entire spacetime. But it is easy to prove that there exist outgoing radial null geodesics (ingoing Eddington-Finkelstein coordinates are adapted to ingoing radial null geodesics) that asymptote to $v \to \pm\infty$ for a finite value of their affine parameter (see section 1.2.1). This shows that the portion of spacetime covered by these coordinates is geodesically incomplete and there is still more spacetime to be covered.

The hypersurfaces where $f(r) = 0$ are implicitly defined by $C(r) = r - r_i = 0$ and their normal $n_\mu := \partial_\mu C(r)$ satisfies $n^\mu n_\mu = f(r) = 0$. This shows that $r = r_i$ is a null hypersurface. It is actually a null geodesic congruence generated by outgoing radial null geodesics. All null surfaces behave as one-way membranes for physical observers since they are bound to move inside their light cone. The peculiarity of the $r = r_i$ surfaces in strongly spherically symmetric spacetimes is that besides being null they are also surfaces of constant radius. As a result, no information inside the spacetime region at $r < r_i$ can ever reach the region at $r > r_i$. A surface partitioning spacetime in this way is called an *horizon*.

There are several different types of horizons. A *Killing horizon* is a null hypersurface defined by the vanishing of a Killing vector field. As clearly shown by the vanishing of the g_{vv} component of the metric in eq. (1.25) for $r = r_i$, all surfaces $r = r_i$ are a Killing horizon. More about horizons will be said later on.

The metric in outgoing Eddington-Finkelstein coordinates (u, r, θ, ϕ) reads

$$\mathrm{d}s^2 = -f(r)\,\mathrm{d}u^2 - 2\,\mathrm{d}v\,\mathrm{d}r + r^2\,\mathrm{d}\Omega^2\,, \tag{1.27}$$

where the non-spherical Killing vector field is given by ∂_u. Also, this metric is non-singular and non-degenerate for all $r > 0$, and ingoing Eddington-Finkelstein coordinates thus cover all spacetime regions such that

$$-\infty < u < +\infty\,, \qquad 0 < r < +\infty\,. \tag{1.28}$$

It can be proven that this portion of spacetime is geodesically incomplete with respect to ingoing radial null geodesics. Although both ingoing and outgoing Eddington-Finkelstein coordinates cover spacetime regions for which $0 < r < +\infty$, these are not the same spacetime regions. The hypersurfaces where $f(r) = 0$ in these coordinates are still null, but this time they are a null geodesic congruence generated by ingoing radial null geodesics. They also are Killing horizons.

Both ingoing and outgoing Eddington-Finkelstein coordinates are thus able to extend the spacetime coverage of the (t, r, θ, ϕ) coordinates to the full radial interval $0 < r < +\infty$. They do so however extending different sets of radial null geodesics and thus covering different spacetime horizons and regions. This notwithstanding, it is possible to cover the maximal extension of spacetime by appropriately using several Eddington-Finkelstein charts.

Horizon spacetime points, that is the points of spacetime for which $f(r) = 0$, cannot be covered by the (t, r, θ, ϕ) coordinate system. It would thus be best to define strongly spherically symmetric spacetimes in terms of Eddington-Finkelstein coordinates instead of the (t, r, θ, ϕ) coordinates.

Finally, the metric in the double-null coordinate system (u, v, θ, ϕ) takes the following form:

$$\mathrm{d}s^2 = -f(r)\,\mathrm{d}u\,\mathrm{d}v + r^2\,\mathrm{d}\Omega^2\,, \tag{1.29}$$

where $r = r(u, v)$ is implicitly defined by

$$r_*(r) = \frac{v - u}{2} \tag{1.30}$$

and the coordinate intervals are

$$-\infty < u < +\infty\,, \qquad -\infty < v < +\infty\,. \tag{1.31}$$

Interestingly, although the coordinates u and v are separately able to cover several spacetime horizons, one or the other is not defined on every given horizon, and thus the double-null coordinate system (u, v, θ, ϕ) does not improve the spacetime coverage of the coordinate system (t, r, θ, ϕ). This can be shown in a few different ways. The metric in eq. (1.29) is degenerate whenever $f(r)$ has a zero, thus confirming that the double-null coordinates are not well defined on any horizon. Furthermore, the metric is well defined only as long as $r = r(u, v)$ is a well-defined function of u and v. Given eq. (1.30), this requires $r_*(r)$ to be an invertible function. Since however $\mathrm{d}r_*/\,\mathrm{d}r = 1/f(r)$, $r_*(r)$ is separately monotonic and invertible in each interval $r_j < r < r_{j+1}$ $(j = 0, 1, \ldots, N)$, but not globally. Accordingly, the double-null coordinate chart (u, v, θ, ϕ) can only separately cover each spacetime region satisfying $r_j < r < r_{j+1}$ $(j = 0, 1, \ldots, N)$.

Unlike what happens in Minkowski spacetime, the double-null coordinates (u, v, θ, ϕ) do not provide a global coordinate chart for a generic strongly spherically symmetric spacetime and a direct compactification of them would not produce a Carter-Penrose diagram. Starting from these coordinates, there are two different ways to obtain a Carter-Penrose diagram. The first one is to separately construct a Carter-Penrose diagram for each spacetime region satisfying $r_j < r < r_{j+1}$ $(j = 0, 1, \ldots, N)$, and then appropriately glue them together. The second one is to take advantage of the freedom in performing a change of double-null coordinates (see eq. (1.10)) without messing up the light cone structure to find global double-null coordinates for spacetime. The Carter-Penrose diagram is then obtained by compactification of this global coordinate chart.

The analysis of spacetime in Eddington-Finkelstein coordinates showed that a strongly spherically symmetric spacetime can be seen as a collection of regions

$r_j < r < r_{j+1}$ separated by horizons. Let each region $r_j < r < r_{j+1}$ be called a *block*. Spacetime is thus a collection of blocks separated by horizons. A compactification of the double-null coordinates (u, v, θ, ϕ) results in a Carter-Penrose diagram for a single block. A block delimited by two zeroes of $f(r)$ is bounded by only horizons. Furthermore, since horizons are generated by either ingoing or outgoing radial null geodesics, they will look like lines at ±45° in a Carter-Penrose diagram. Internal blocks, i.e. blocks delimited by two zeroes of $f(r)$, will then necessarily look like diamonds. The Carter-Penrose diagram of blocks such that $0 < r < r_1$ will roughly look like the Carter-Penrose diagram of Minkowski spacetime in fig. 1.1. The shape of the Carter-Penrose diagram of blocks such that $r_N < r < +\infty$ will depend on the asymptotic behavior of $f(r)$. In asymptotically flat spacetimes they will also look like a diamond. A clear display of this block division of spacetime is given by the Carter-Penrose diagram of Reissner-Nordström spacetime in chapter 2.

Walker [12] realized that if the causal and the global structure of spacetime are the only properties of interest, then it would suffice to construct a diagram out of all the separate Carter-Penrose diagrams of each block where connected blocks are drawn sharing the appropriate horizon. Such a diagram is called *block diagram* of the spacetime. The block diagram of a spacetime region covered by ingoing (outgoing) Eddington-Finkelstein coordinates is given by $N + 1$ blocks, one for each region $r_j < r < r_{j+1}$, $j = 0, \ldots, n$, appropriately connected by their shared horizons lines at $45°$ $(-45°)$. Since there is no global coordinate chart associated to this diagram, a block diagram is not a Carter-Penrose diagram according to the definition of the latter given above. This notwithstanding, they are a tremendously useful tool to visualize spacetime and study its causal and global aspects. If however the diagram is needed to analyze more than just the causal structure of spacetime, like plotting a geodesic or a wordline intersecting one or more horizons or studying some geometric property of spacetime, then a global coordinate chart is needed.

An algorithm to define global coordinates for the Carter-Penrose diagram of strongly spherically symmetric spacetimes starting from the compact coordinates of each block was recently defined by Schindler and Aguirre [8, 13]. This algorithm applies to all strongly spherically symmetric spacetimes with a defining function $f(r)$ that is analytic at its zeroes and whose zeroes are all simple (order one).

The second road to a global coordinate chart for the Carter-Penrose diagram of a strongly spherically symmetric spacetime is to find global double-null coordinates before compactification. The best-known example of such a construction is the Kruskal-Szekeres coordinates [14, 15] for Schwarzschild spacetime which will be discussed in the next section. In chapter 2 I will introduce a generalization of the Kruskal-Szekeres coordinates that provides a global double-null coordinate chart for strongly spherically symmetric spacetimes and with it a global coordinate chart for their Carter-Penrose diagram. Although these generalized Kruskal-Szekeres coordinates will be introduced in the specific context of Reissner-Nordström spacetime [16, 17], as long as the tortoise coordinate $r_*(r)$ can be explicitly computed their generalization to an arbitrary strongly spherically symmetric spacetime is straightforward. These coordinates will be in fact also used in chapter 3 to draw the Carter-Penrose diagrams of the black-to-white hole spacetime.

1.2 Black holes

Black holes are very common astrophysical objects in contemporary physics. Astronomers routinely observe quasars powered by super-massive black holes, Virgo and LIGO interferometers regularly measure the gravitational waves produced by the merger of two spiraling black holes [18], we even took a few good pictures of them [19, 20]. This notwithstanding, there is still whatsoever no consensus upon their exact theoretical definition [21]. Several different, and often conflicting, definitions of black holes exist. Each one is useful to study different properties of these objects, and none of them is free from undesirable features.

The most common definition of a black hole, the one found in most textbooks on general relativity, is given in terms of the global causal structure of spacetime introduced in the last section: a black hole in an asymptotically flat spacetime is a region $\mathscr{V}$ in spacetime which is not contained in the causal past of future null infinity $\mathscr{I}^+$. The boundary $\partial\mathscr{V}$ of the region $\mathscr{V}$ is called the *event horizon* of the black hole.

This is a perfectly good definition that mathematically formalizes the heuristic idea of a black hole as a region of spacetime that can be entered but never exited, a so-called “region of no escape”. However, while it provides a useful notion of horizon in highly symmetrical and non-dynamical black hole models, it becomes quite unpractical in the general case. Its main drawback is that the definition of event horizon requires the knowledge of all the information reaching future null infinity to determine its location. It is thus a highly non-local definition that cannot be used either experimentally or in numerical simulations. Furthermore, this definition is not compatible with the black-to-white hole scenario and any other non-singular black hole scenario in which no event horizon ever forms. According to this definition, the black-to-white hole spacetime does not contain any black hole at all. Luckily, a different definition of a black hole better suited for describing local physics and consistent with the black-to-white hole scenario can be given using quasi-local geometric properties of spacetime.

Let $\mathscr{S}$ be an orientable two-dimensional spacelike surface in spacetime. Two future-directed null vectors orthogonal to $\mathscr{S}$ can be defined at each point $p \in \mathscr{S}$. These vectors can be used to locally construct two congruences, the *ingoing congruence* and the *outgoing congruence*, of future-directed null geodesics orthogonal to $\mathscr{S}$. It is then possible to investigate the behavior of infinitesimally close geodesics in these congruences in the local future of $\mathscr{S}$. Specifically, it can be studied if these geodesics converge toward each other or if they drift apart. The expansion Θ of a congruence is the parameter that measures this property: If Θ is negative nearby geodesics converge toward each other while if Θ is positive nearby geodesics drift apart.

The surface $\mathscr{S}$ is called a *trapped surface* if the expansion Θ of both ingoing and outgoing congruences of null geodesics is negative on the whole surface. If Θ is instead negative for one of the congruences and vanishing on the other, the surface is called *marginally trapped*. A black hole can then be defined as a *trapped region*, that is a region in which every point belongs to a trapped surface. The boundary of the trapped region, which is a marginally trapped surface, is called *apparent horizon*. This is the definition of a black hole used in this manuscript. See Faraoni [22] and references therein for a review of all the different notions of horizon.

1.2.1 Schwarzschild spacetime

Schwarzschild [23] found the exact solution of Einstein field equations describing a non-rotating and uncharged black hole of mass m soon after Einstein published his famous equations. In Planck natural units $c = G = \hbar = 1$ and spherical coordinates (t, r, θ, ϕ), the metric of this spacetime reads

$$\mathrm{d}s^2 = -\left(1 - \frac{2m}{r}\right) \mathrm{d}t^2 + \left(1 - \frac{2m}{r}\right)^{-1} \mathrm{d}r^2 + r^2\, \mathrm{d}\Omega^2\,. \tag{1.32}$$

It is thus a strongly spherically symmetric spacetime with defining function $f(r) = 1 - 2m/r$. This means that all the results obtained in section 1.1.2 for arbitrary spherically symmetric spacetimes can be used for the description of this spacetime.

The function $f(r)$ has only one zero in $r_1 = 2m$, which is thus a Killing horizon. The coordinate chart (t, r, θ, ϕ) can be used to separately cover all spacetime regions such that $0 < r < 2m$ or $2m < r < +\infty$. The coordinates t and r are respectively timelike and spacelike in the spacetime regions where $2m < r < +\infty$. These regions are also static since ∂_t is timelike. On the contrary, in the spacetime regions where $0 < r < 2m$ the coordinate t is spacelike and the coordinate r is timelike. The metric in these regions is homogeneous but neither static nor stationary.

The metric in eq. (1.32) has a coordinate singularity at $r = 2m$ and a true curvature singularity in $r = 0$, where the curvature invariants become infinite.

The tortoise coordinate $r_*(r)$ satisfying $\mathrm{d}r_* = \mathrm{d}r/f(r)$ is given by

$$r_*(r) = r + 2m \log \left| r/2m - 1 \right|, \tag{1.33}$$

where the integration constant has been fixed such that $r_*(0) = 0$. The retarded and advanced time coordinates u and v then reads

$$\begin{aligned} u &= t - r - 2m \log\left|r/2m - 1\right| , \\ v &= t + r + 2m \log\left|r/2m - 1\right| , \end{aligned} \tag{1.34}$$

and the Schwarzschild line element in double-null form becomes

$$\mathrm{d}s^2 = -\left(1 - \frac{2m}{r}\right) \mathrm{d}u\,\mathrm{d}v + r^2\,\mathrm{d}\Omega^2 , \tag{1.35}$$

where $r = r(u, v)$. As already pointed out in the last section, the metric in eq. (1.35) is still ill-defined on the horizon and the coordinate chart (u, v, θ, ϕ) does not improve the spacetime coverage of the Schwarzschild coordinates (t, r, θ, ϕ).

A global double-null coordinate chart for Schwarzschild spacetime is given by the Kruskal-Szekeres coordinates [14, 15]. These coordinates can be derived in several different ways. One of the derivations that I find most informative, and that will be at the center of the construction of the generalized Kruskal-Szekeres coordinates in chapter 2, is based on the analysis of the behavior of radial null geodesics in Eddington-Finkelstein coordinates.

The Schwarzschild line element in ingoing Eddington-Finkelstein coordinates reads

$$\mathrm{d}s^2 = -\left(1 - \frac{2m}{r}\right) \mathrm{d}v^2 + 2\,\mathrm{d}v\,\mathrm{d}r + r^2\,\mathrm{d}\Omega^2 . \tag{1.36}$$

These coordinates are able to cover an entire spacetime region for which $0 < r < +\infty$. Radial null geodesics in these coordinates satisfy

$$f(r)\dot{v}^2 - 2\dot{v}\dot{r} = 0 \tag{1.37}$$

(normalization of 4-velocity) and

$$f(r)\dot{v} - \dot{r} = E \tag{1.38}$$

(due to v-translation invariance), where the overdot means differentiation with respect to an affine parameter λ and E is the constant of motion associated with the Killing vector field ∂_v. A first set of solutions is given by geodesics satisfying

$$\dot{v} = 0\,, \qquad\qquad \dot{r} = -E\,, \tag{1.39}$$

that is

$$v(\lambda) = v_0\,, \qquad r(\lambda) = r_0 - E\lambda\,, \tag{1.40}$$

with v_0 and r_0 constants of integration. For $E > 0$ these solutions, which are valid for $-\infty < \lambda < r_0/E$, describe future-oriented ingoing radial null geodesics starting out at an infinite radius for $\lambda \to -\infty$, crossing the horizon at $r = 2m$ and then finally hitting the $r = 0$ curvature singularity for $\lambda = r_0/E$.

A different set of solutions, which by exclusion will describe outgoing radial null geodesics, satisfy

$$\dot{v} = \frac{2E}{f(r)}\,, \qquad\qquad \dot{r} = E\,. \tag{1.41}$$

For future-oriented geodesics E must be taken negative in $0 < r < 2m$ and positive in $2m < r < +\infty$. Focusing on the exterior region $2m < r < +\infty$ and choosing $r_0 = 2m$ for simplicity, outgoing radial null geodesics are given by

$$r(\lambda) = 2m + E\lambda\,, \qquad \lambda \in \big(0, +\infty\big)\,, \tag{1.42}$$

$$v(\lambda) = 2E\lambda + 4m\log|\lambda| + K\,, \tag{1.43}$$

where K is a constant identifying different geodesics. These curves suddenly start at the horizon $r = 2m$, that is $r \to 2m$ for $\lambda \to 0^+$, and then keep moving towards increasing radius, asymptotically going to $r \to +\infty$ for $\lambda \to +\infty$. Notice that the horizon these geodesics start at is different from the horizon the ingoing radial null geodesics pass through. This horizon is at $v \to -\infty$ and finite $u = v - 2r_*(r)$, while the horizon intersected by ingoing geodesics is at finite $v = v_0$ and infinite u.

This analysis perfectly displays the physics of ingoing Eddington-Finkelstein coordinates. They are able to cover the full range of the affine parameter of ingoing radial null geodesics, as they are adapted to them, and so they extend the spacetime coverage to all the regions where these geodesics go trough. Specifically, starting from the exterior region $2m < r < +\infty$, they extend spacetime coverage through the horizon in the future of the ingoing geodesics. Notice that although the range of the affine parameter of the ingoing geodesics in eq. (1.40) abruptly stops at $\lambda = r_0/E$, this is because the geodesics hit the curvature singularity in $r = 0$ there. So this geodesic incompleteness is an actual property of spacetime, not a coordinate artifact. On the contrary, the abrupt start of the radial outgoing geodesics in eqs. (1.42) and (1.43) at the past horizon is indeed a coordinate artifact. Since the horizon is a well-defined hypersurface and spacetime smoothly continues beyond it, so must these geodesics. The ingoing Eddington-Finkelstein coordinates are not able to follow outgoing radial null geodesics past this horizon.

The same analysis performed in outgoing Eddington-Finkelstein coordinates shows that future-oriented outgoing radial null geodesics are given by

$$u(\sigma) = u_0\,, \qquad r(\sigma) = r_0 + E\sigma\,, \tag{1.44}$$

for an affine parameter $\sigma \in (-r_0/E, +\infty)$ and $E > 0$, while future-oriented ingoing radial null geodesics in region $2m < r < +\infty$ are given by

$$r(\sigma) = 2m - E\sigma\,, \qquad \sigma \in (-\infty, 0)\,, \tag{1.45}$$

$$u(\sigma) = 2E\sigma - 4m\log|\sigma| + K'\,, \tag{1.46}$$

where K' is a constant identifying different geodesics and r_0 has been set to $r_0 = 2m$ for simplicity. These coordinates are perfectly able to retrace the steps of outgoing radial null geodesics through the past horizon at $v \to -\infty$ and cover the full range of their affine parameter up to a past singularity at $r = 0$. But they cannot follow ingoing radial null geodesics through the future horizon at $u \to +\infty$

This investigation clearly shows how ingoing and outgoing Eddington-Finkelstein coordinates extend the spacetime coverage of the coordinates (t, r, θ, ϕ) in different directions and why the double-null coordinate system (u, v, θ, ϕ) still fails at every horizon like the original Schwarzschild coordinates. The analysis itself however suggests a solution to the last issue: the affine parameters λ and σ are the natural coordinates to extend v and u beyond the horizons.

Keeping only the leading term near the horizon of eqs. (1.43) and (1.46), Kruskal-Szekeres coordinates $u_{\rm KS}$ and $v_{\rm KS}$ are defined as

$$\begin{aligned} u &= -\,4m \log |u_{\rm KS}|\,, \\ v &= 4m \log |v_{\rm KS}|\,. \end{aligned} \tag{1.47}$$

The Schwarzschild line element in these coordinates reads

$$\mathrm{d}s^2 = \frac{16m^2}{u_{\rm KS}\, v_{\rm KS}} f(r)\; \mathrm{d}u_{\rm KS}\, \mathrm{d}v_{\rm KS} + r^2\; \mathrm{d}\Omega^2\,, \tag{1.48}$$

with $r = r(u_{\rm KS}, v_{\rm KS})$ implicitly defined by

$$r_*(r) = \frac{v(v_{\rm KS}) - u(u_{\rm KS})}{2}\,. \tag{1.49}$$

Using the exact expression of the tortoise coordinate in eq. (1.33), the last relation can be rewritten as

$$u_{\rm KS}\, v_{\rm KS} = (1 - r/2m)\, e^{r/2m}\,, \tag{1.50}$$

showing that the coordinate range of the Kruskal-Szekeres coordinates is

$$-\infty < u_{\rm KS} < +\infty\,, \qquad -\infty < v_{\rm KS} < \infty\,, \qquad u_{\rm KS}\, v_{\rm KS} < 1\,. \tag{1.51}$$

Inserting eq. (1.50) in eq. (1.48) the Schwarzschild line element becomes

$$\mathrm{d}s^2 = -\frac{32m^3}{r} e^{-r/2m}\; \mathrm{d}u_{\rm KS}\, \mathrm{d}v_{\rm KS} + r^2\; \mathrm{d}\Omega^2\,. \tag{1.52}$$

To show that the metric in these coordinates is well defined it is then necessary to show that $r(u_{\rm KS}, v_{\rm KS})$ is a regular function. Luckily, this function can be explicitly given in terms of the *Lambert W function*, which is defined as the solution of the equation

$$x = W(x)\, e^{W(x)}\,. \tag{1.53}$$

This function is regular for $x > 1/e$ and it cannot be expressed in terms of elementary functions. Rewriting eq. (1.50) as

$$-\frac{u_{\mathrm{KS}}\, v_{\mathrm{KS}}}{e} = (r/2m - 1)\, e^{r/2m-1}\,, \tag{1.54}$$

it is clear that

$$r(u_{\mathrm{KS}}, v_{\mathrm{KS}}) = 2m\Big[W\big(-u_{\mathrm{KS}}\, v_{\mathrm{KS}}/e\big) + 1\Big]\,. \tag{1.55}$$

For u_{KS} and v_{KS} satisfying eq. (1.51) $-u_{\mathrm{KS}}\, v_{\mathrm{KS}}/e > -1/e$ and so $r(u_{\mathrm{KS}}, v_{\mathrm{KS}})$, and with it the metric tensor in eq. (1.52), is everywhere regular.

The Kruskal-Szekeres coordinates provide the needed global double-null coordinate chart for the maximal extension of Schwarzschild spacetime. It is then possible to use the standard change of coordinates

$$U = \tan^{-1}(u_{\mathrm{KS}})\,, \qquad V = \tan^{-1}(v_{\mathrm{KS}}) \tag{1.56}$$

$$T = U + V, \qquad R = V - U\,, \tag{1.57}$$

resulting in the coordinate intervals

$$-\pi/2 < U < \pi/2\,, \qquad -\pi/2 < V < \pi/2\,, \qquad -\pi/2 < T < \pi/2\,, \tag{1.58}$$

to define the coordinates of the Carter-Penrose diagram of Schwarzschild spacetime. The metric in these coordinates reads

$$\mathrm{d}s^2 = \frac{16m^3\, e^{-r/2m}/r}{\cos^2\big[(T-R)/2\big]\cos^2\big[(T+R)/2\big]}\Big[-\mathrm{d}T^2 + \mathrm{d}R^2\Big] + r^2\, \mathrm{d}\Omega^2\,, \tag{1.59}$$

with

$$r(T,R) = 2m\Big[W\big(-\tan\big[(T-R)/2\big]\tan\big[(T+R)/2\big]/e\big) + 1\Big]\,. \tag{1.60}$$

The Carter-Penrose diagram of the maximal extension of Schwarzschild spacetime is shown in fig. 1.2. All the information learned by the analysis of radial

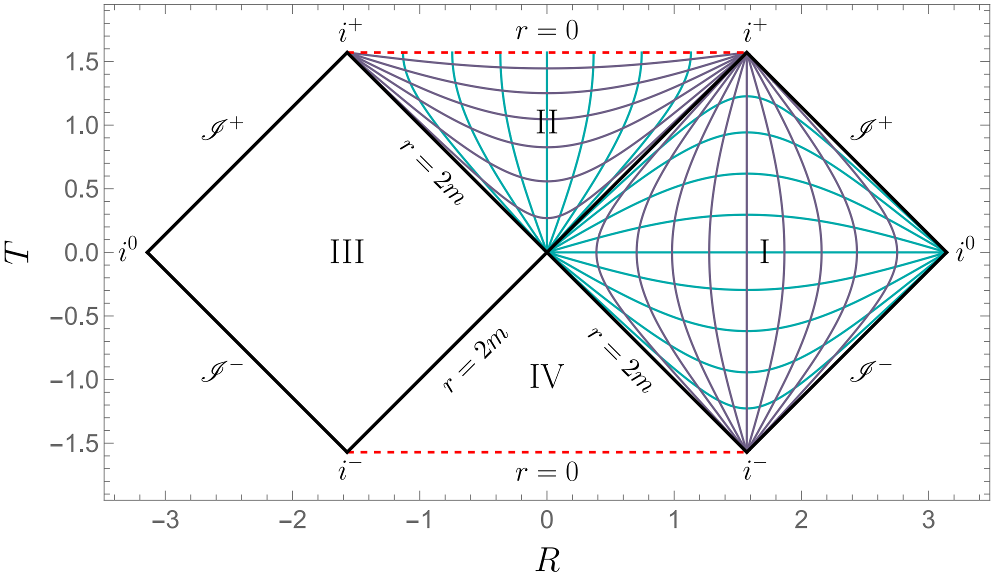

Figure 1.2: Carter-Penrose diagram of the maximal extension of Schwarzschild spacetime. In light blue curves of constant t, in violet curves of constant r and in a dashed red line the future and past curvature singularities at $r = 0$.

null geodesics in Eddington-Finkelstein coordinates is beautifully displayed by the diagram. Spacetime is divided into four blocks I, II, III, and IV. Each block can be separately covered by the Schwarzschild coordinates (t, r, θ, ϕ). Blocks I and III have $2m < r < +\infty$ while blocks II and IV have $0 < r < 2m$. Ingoing Eddington-Finkelstein coordinates are adapted to ingoing radial null geodesics, namely to straight lines tilted at −45° on the diagram, and are able to cover at the same time either blocks I and II or blocks III and IV. The ingoing geodesics described by eq. (1.40) start at past null infinity $\mathscr{I}^-$ in block I, move as straight lines tilted at −45°, cross the horizon connecting blocks I and II and finally hit the future curvature singularity at $r = 0$. The outgoing geodesics described by eqs. (1.42) and (1.43) suddenly start at the past horizon connecting blocks I and IV, move as straight lines tilted at 45°, and asymptote to future null infinity $\mathscr{I}^+$ of block I. Naturally, these geodesics really start at the past curvature singularity in block IV and then move towards region I. But ingoing Eddington-Finkelstein coordinates cannot describe blocks IV and I at the same time. Analogously, outgoing Eddington-Finkelstein coordinates are able to cover at the same time either blocks I and IV, or blocks II and III.

Thanks to the visual representation of spacetime provided in fig. 1.2, it is straightforward to qualitatively determine that the spacetime contains a black hole. Consider in fact the spacetime region in block II. Since an observer is always forced to move inside their light cone, and the latter, together with the horizons bounding region II, is formed by straight lines tilted at ±45°, any wordline entering region II is bound to remain inside it. Actually, it is bound to hit the future curvature singularity in $r = 0$, which is a spacelike curve, in a finite proper time. This suggests that the spacetime region in block II is a black hole. It can indeed be rigorously proved that this region is trapped, and the two horizons bounding it are apparent horizons. Furthermore, it is also clear that the region in block II is not contained in the causal past of future null infinity $\mathscr{I}^+$, thus making the horizons at $r = 2m$ bounding the black hole also event horizons. In Schwarzschild spacetime, the black hole horizons are thus killing horizons, apparent horizons, and event horizons at the same time. This is due to the high symmetry and non-dynamical nature of the Schwarzschild geometry. This special property is not preserved by more complicated black hole models.

Black holes are often heuristically said to be regions of spacetime where the gravitational field is so strong that nothing can escape them, not even light. While technically correct, this statement brings to mind a Newtonian picture of light moving outwards, turning around, and then moving back inward due to the strong gravitational pull. This is not what is happening in region II. Notice in fact that moving forward in time in region II of fig. 1.2 corresponds to moving towards smaller and smaller radius r until you hit the curvature singularity at $r = 0$. So moving forward in time inside a black hole means moving towards its ‘center’. A better heuristic definition of a black hole, as suggested by Hamilton [24], is that a black hole is a region of spacetime where space is falling faster than light. As a consequence, light moving outwards inside a black hole is nonetheless carried inward by the faster-than-light inflow of space, like a fish trying but failing to swim up a waterfall.

The spacetime region in block IV is the time-reverse of the black hole region and it is called *white hole* region. Contrary to what happens in region II, where any wordline is bound to remain inside of it, every wordline inside the white hole region is forced to exit either in block I or in block III. There is a curvature singularity in the past of this region. The exact definition of a white hole and of white hole horizons will be given in section 1.2.3.

Both the regions in block I and block III are asymptotically flat regions of spacetime in the exterior of the black hole and of the white hole. Consider for example an observer moving at constant r, θ, and ϕ (violet curves in fig. 1.2) in one of these regions. This observer is in the exterior of the white hole as much as in the exterior of the black hole. Furthermore, since the spacetime regions in block I and block III are static, there is no change in the local physics along the trajectory of the observer. Interestingly, these two exterior regions are causally disconnected: No wordline starting in block III can reach block I either moving in the past or in the future and vice versa.

The maximal extension of Schwarzschild spacetime, while very suggestive, is however clearly unphysical. In this spacetime both the black hole and the white hole are not formed as the result of a physical phenomenon, they simply exist. They are eternal. For this reason, as intriguing as fig. 1.2 may be, the maximal extension of Schwarzschild spacetime is not physically reasonable. Naturally, physical black holes do exist and they are formed by the gravitational collapse of a massive object.

1.2.2 Oppenheimer-Snyder model

The simplest model of black hole formation by gravitational collapse is the Oppenheimer-Snyder model [25]. The massive object undergoing collapse is modeled as a spherical ball of uncharged dust (i.e. a pressureless perfect fluid) of uniform density (i.e. the ball of dust is homogeneous and isotropic).

Since homogeneity and isotropy are the same symmetries satisfied by the universe under the *cosmological principle*, the spacetime metric describing the interior of the collapsing star is the same spacetime metric used in cosmology: the *Friedmann-Lemaître-Robertson-Walker* (FLRW) *metric*. This metric can be written as

$$\mathrm{d}s^2 = -\,\mathrm{d}t^2 + a^2(t)\left(\frac{\mathrm{d}\tilde{r}^2}{1-k\,\tilde{r}^2} + \tilde{r}^2\,\mathrm{d}\Omega^2\right), \tag{1.61}$$

in a coordinate system $(t, \tilde{r}, \theta, \phi)$, where $a(t)$, known as *scale factor*, is the only degree of freedom of the metric and k is a parameter controlling the geometry and the topology of the spatial slices of spacetime at constant time t. The time coordinate t is the proper time along curves of constant $\tilde{r}$, θ, and ϕ, which turn out to be geodesics of the spacetime. The coordinate $\tilde{r}$ is thus the spatial coordinate adapted to these geodesics, and its relation with the usual radial coordinate r whose square multiplied by 4π gives the area of the surface at constant t and r is $r = a(t)\,\tilde{r}$. The scale factor thus controls the size of the spatial geometry. The coordinate interval of the time coordinate t depends on the regularity of the scale factor. The coordinate interval of $\tilde{r}$ is given by $0 < \tilde{r} \leq \tilde{r}_{\mathrm{b}}(t)$, where $\tilde{r}_{\mathrm{b}}(t)$ is the wordline of the boundary of the star seen from the interior. The coordinates θ and ϕ are the usual angular coordinates adapted to the spherical symmetry. This coordinate system is usually referred to as the *comoving* coordinate system, as it is adapted to, or comoving with, the geodesics moving at constant $\tilde{r}$, θ, and ϕ.

It can be shown that pressureless dust necessarily moves along geodesics of spacetime. This means that also the boundary of the star must move along a geodesic. Let then the wordline of the boundary of the star be $\tilde{r}_{\mathrm{b}}(t) = \tilde{r}_{\mathrm{b}}$, where $\tilde{r}_{\mathrm{b}}$ is a constant and t is then the proper time along the geodesic.

The Einstein field equations for the FLRW metric in eq. (1.61) reduce to the *Friedmann equation* for the scale factor

$$\dot{a}^2 + k = \frac{8\pi}{3}\rho\, a^3\,, \tag{1.62}$$

where $\rho(t)$ is the uniform density of the star and the overdot means differentiation with respect to t. Parametrizing this density in terms of the total mass M of the star as

$$\rho = \frac{M}{\frac{4\pi}{3} r_{\mathrm{b}}^3} = \frac{3M}{4\pi\tilde{r}_{\mathrm{b}}^3}\frac{1}{a^3}, \tag{1.63}$$

the Friedmann equation can be rewritten as

$$\dot{a}^2 + k = \frac{2M}{\tilde{r}_\mathrm{b}^3}\frac{1}{a}\,. \tag{1.64}$$

The physical radius $r_\mathrm{b}(t) = a(t)\,\tilde{r_\mathrm{b}}$ of the boundary of the star then satisfies

$$\dot{r}_\mathrm{b}^2 + k\tilde{r}_\mathrm{b}^2 = \frac{2M}{r_\mathrm{b}}\,. \tag{1.65}$$

Assuming the boundary of the star to start collapsing from rest at $r \to +\infty$, the value of k needs to be fixed to $k = 0$. Equation (1.65) can then be solved to get

$$r_\mathrm{b}(t) = \left[9M(t_0 - t)^2/2\right]^{1/3}. \tag{1.66}$$

So the star starts to collapse from rest at $r \to +\infty$ for $t \to -\infty$ and then keeps collapsing until it reaches a singular point of vanishing physical radius r_b at $t = t_0$. The coordinate interval of the time coordinate is then $-\infty < t < t_0$.

The spacetime region in the exterior of the star is described by Schwarzschild geometry. In fact, while the maximal extension of Schwarzschild geometry in vacuum gives the spacetime represented in fig. 1.2 and containing a black hole and a white hole, the same geometry also describes the exterior region of any spherically symmetric massive object. In the usual Schwarzschild coordinates $(t_\mathrm{S}, r_\mathrm{S}, \theta, \phi)$, where t_S and r_S are used instead of t and r to avoid confusion with the time and radial coordinates of the FLRW metric, the exterior metric is thus given by

$$\mathrm{d}s^2 = -\left(1 - \frac{2m}{r_\mathrm{S}}\right)\mathrm{d}t_\mathrm{S}^2 + \left(1 - \frac{2m}{r_\mathrm{S}}\right)^{-1}\mathrm{d}r_\mathrm{S}^2 + r_\mathrm{S}^2\,\mathrm{d}\Omega^2\,. \tag{1.67}$$

The coordinate interval of the radial coordinate r_S is however restricted to $r_\mathrm{S}^\mathrm{b}(t_\mathrm{S}) < r_\mathrm{S} < +\infty$, where $\big(t_\mathrm{S}^\mathrm{b}(\tau), r_\mathrm{S}^\mathrm{b}(\tau)\big)$ is the wordline of the boundary of the star seen from the exterior as a function of its proper time $\tau = t$.

In situations like this one, where a hypersurface partitions spacetime into two regions that are separately described in two a priori different coordinate systems, it can be shown that the union of the two regions gives a well-defined solution of Einstein field equations only if the induced metric and the extrinsic curvature of the hypersurface match on the two sides. These conditions are known as the *Israel-Barrabès junction conditions* [26]. Requiring these conditions to be satisfied for the Oppenheimer-Snyder model, as explicitly carried out in Poisson [26], fixes the exterior wordline of the boundary of the star $\big(t_{\rm S}^{\rm b}(\tau), r_{\rm S}^{\rm b}(\tau)\big)$ to be a specific geodesic of the exterior Schwarzschild geometry and it sets $m = M$.

Given the simplicity of the model, it is however possible to do more than this. It is not complicated to find a unique global coordinate system to cover both the interior and exterior of the star. The interior of the star is currently described using the coordinate system $(t, \tilde{r}, \theta, \phi)$, while the exterior is described using Schwarzschild coordinates $(t_{\rm S}, r_{\rm S}, \theta, \phi)$. In both charts, the angular coordinates are the ones adapted to the spherical symmetry of the problem and can then be identified on the boundary of the star without any problem.

If spacetime has to be described with a unique coordinate system and the boundary of the star is a geodesic with respect to the interior metric, then it must be a geodesic also with respect to the exterior metric. The interior boundary of the star in eq. (1.66) describes a radial geodesic starting at rest at infinity in FLRW spacetime. It is therefore reasonable to assume that the exterior boundary of the star $\big(t_{\rm S}^{\rm b}(\tau), r_{\rm S}^{\rm b}(\tau)\big)$ is described by a radial geodesic starting at rest at infinity in Schwarzschild spacetime. It is indeed easy to show that these geodesics satisfy

$$\left(\dot{r}_{\rm S}^{\rm b}\right)^2 = \frac{2m}{r_{\rm S}^{\rm b}} \qquad\qquad \dot{t}_{\rm S}^{\rm b} = 1/f\,, \tag{1.68}$$

where the overdot indicates differentiation with respect to proper time τ. The first of these equations is exactly eq. (1.66) for $k = 0$, and it can be solved to obtain

$$r_{\rm S}^{\rm b}(\tau) = \left[9m(\tau_0 - \tau)^2/2\right]^{1/3}. \tag{1.69}$$

Clearly, it would be straightforward to match eqs. (1.66) and (1.69) working in the radial coordinate r. Also, being r and $r_{\rm S}$ the radial coordinates adapted to spherical symmetry (i.e. those coordinates whose square multiplied by 4π gives the area of the surface defined by the angular coordinates) in the interior and the exterior regions, they can be identified on the boundary and be given the same name r.

So, changing coordinates in the interior of the star from $(t, \tilde{r}, \theta, \phi)$ to (t, r, θ, ϕ), where $r = a(t)\,\tilde{r}$ and remembering that k has been set to zero, the FLRW metric becomes

$$\begin{aligned} \mathrm{d}s^2 &= -\,\mathrm{d}t^2 + \left(\mathrm{d}r - r\frac{\dot{a}}{a}\,\mathrm{d}t\right)^2 + r^2\,\mathrm{d}\Omega^2 \\ &= -\,\mathrm{d}t^2 + \left(\mathrm{d}r + \frac{2r}{3\,(t_0 - t)}\,\mathrm{d}t\right)^2 + r^2\,\mathrm{d}\Omega^2\,. \end{aligned} \tag{1.70}$$

Three out of the four coordinates have been identified. The remaining one is the temporal one. The interior time coordinate t has a pretty straightforward interpretation at the boundary: it is the proper time of the boundary's trajectory. Evidently, if the exterior metric is rewritten in terms of a temporal coordinate giving the proper time along radially infalling geodesics, the two time coordinates will match at the boundary. This coordinate, found independently by Painlevé [27] and Gullstrand [28], can be written as a function of the Schwarzschild coordinates t_{S} and r_{S} as

$$t_{\mathrm{PG}}(t_{\mathrm{S}}, r_{\mathrm{S}}) = t_{\mathrm{S}} + 2\sqrt{2mr_{\mathrm{S}}} + 2m\ln\left|\frac{\sqrt{r_{\mathrm{S}}/2m} - 1}{\sqrt{r_{\mathrm{S}}/2m} + 1}\right|. \tag{1.71}$$

Changing coordinates in the exterior of the star from $(t_{\mathrm{S}}, r_{\mathrm{S}}, \theta, \phi)$ to $(t_{\mathrm{PG}}, r, \theta, \phi)$, where r_{S} has just been identified with the radial coordinate r, the Schwarzschild metric becomes

$$\mathrm{d}s^2 = -\,\mathrm{d}t_{\mathrm{PG}}^2 + \left(\mathrm{d}r + \sqrt{2m/r}\,\mathrm{d}t_{\mathrm{PG}}\right)^2 + r^2\,\mathrm{d}\Omega^2\,. \tag{1.72}$$

The coordinates t and t_{PG} can then be identified on the star's boundary and be given the same name t_{PG}.

The entire spacetime can be written in terms of a unique global coordinate system $(t_{\mathrm{PG}}, r, \theta, \phi)$. For this construction to give a well-defined solution of Einstein field equations, it is necessary that the trajectory, the induced metric, and the extrinsic curvature of the star's boundary match on the two sides. Requiring $r_{\mathrm{b,\,in}}(t_{\mathrm{PG}})$ in eq. (1.66) to match $r_{\mathrm{b,\,ext}}(t_{\mathrm{PG}})$ in eq. (1.69) sets $m = M$. Namely, the central mass m experienced in the vacuum region in the exterior of the star is simply given by the total mass of the star. The interior and exterior induced metrics on the star's boundary satisfy

$$\begin{aligned}
\mathrm{d}s^2_{\mathrm{b,\,in}} \equiv & \left[-\,\mathrm{d}t^2_{\mathrm{PG}} + \left(\mathrm{d}r + \frac{2r}{3\,(t_0 - t)}\,\mathrm{d}t_{\mathrm{PG}} \right)^2 + r^2\,\mathrm{d}\Omega^2 \right]\Bigg|_{r=r_{\mathrm{b,\,in}}} \\
= & -\,\mathrm{d}t^2_{\mathrm{PG}} + r^2_{\mathrm{b,\,in}}\,\mathrm{d}\Omega^2 \\
= & -\,\mathrm{d}t^2_{\mathrm{PG}} + r^2_{\mathrm{b,\,ext}}\,\mathrm{d}\Omega^2 \\
= & \left[-\,\mathrm{d}t^2_{\mathrm{PG}} + \left(\mathrm{d}r + \sqrt{2m/r}\,\mathrm{d}t_{\mathrm{PG}} \right)^2 + r^2\,\mathrm{d}\Omega^2 \right]\Bigg|_{r=r_{\mathrm{b},\,ext}} = \mathrm{d}s^2_{\mathrm{b,\,ext}}\,,
\end{aligned} \tag{1.73}$$

showing the exact match of the induced metrics on the boundary of the star. The exact match of the extrinsic curvature on the star's boundary can be shown analogously. The full spacetime metric of the Oppenheimer-Snyder model can then be written as

$$\mathrm{d}s^2 = -\,\mathrm{d}t^2_{\mathrm{PG}} + \left(\mathrm{d}r + \sqrt{\frac{2\,m(t_{\mathrm{PG}}, r)}{r}}\,\mathrm{d}t_{\mathrm{PG}} \right)^2 + r^2\,\mathrm{d}\Omega^2\,, \tag{1.74}$$

where

$$m(t_{\mathrm{PG}}, r) = \begin{cases} 2r^3/9(t_{0,\mathrm{PG}} - t_{\mathrm{PG}})^2 & r \le r_{\mathrm{b}}(t_{\mathrm{PG}}), \\ m & r > r_{\mathrm{b}}(t_{\mathrm{PG}}). \end{cases} \tag{1.75}$$

Equivalently, it is sometimes useful to write the metric in terms of the *shift* $N^r(t_{\mathrm{PG}}, r) = \sqrt{2\,m(t_{\mathrm{PG}}, r)/r}$ as

$$\mathrm{d}s^2 = -\,\mathrm{d}t^2_{\mathrm{PG}} + \left(\mathrm{d}r + N^r(t_{\mathrm{PG}}, r)\,\mathrm{d}t_{\mathrm{PG}} \right)^2 + r^2\,\mathrm{d}\Omega^2\,, \tag{1.76}$$

with

$$N^r(t_{\mathrm{PG}}, r) = \begin{cases} 2r/3(t_{0,\mathrm{PG}} - t_{\mathrm{PG}}) & r \le r_{\mathrm{b}}(t_{\mathrm{PG}}), \\ \sqrt{2m/r} & r > r_{\mathrm{b}}(t_{\mathrm{PG}}). \end{cases} \tag{1.77}$$

So the metric of the Oppenheimer-Snyder model takes a particularly simple and clear form in Painlevé-Gullstrand coordinates.

The best way to get a prompt and rough idea of the causal structure of this spacetime is to construct its Carter-Penrose diagram. Unfortunately, this is not so straightforward. A coordinate chart satisfying all the requirements for a Carter-Penrose diagram (see section 1.1) and covering almost the entire spacetime can be found in the following way. Write separately both the interior and exterior of the star in global double-null coordinates, e.g. Kruskal-Szekeres coordinates in the exterior. A direct compactification of these coordinates would produce two separate Carter-Penrose diagrams for the interior and the exterior. It would however be much better to get a unique diagram giving a uniform description of the spacetime like in the Painlevé-Gullstrand coordinates. To accomplish this, new double-null coordinates in the interior that perfectly match the Kruskal-Szekeres coordinates in the exterior can be defined by matching the proper time of the interior and the exterior trajectories of the boundary of the star. This procedure achieves the desired result at the expense of covering the entire spacetime. A finite region of the interior of the star close to the singular point of zero physical radius is not covered by this coordinate chart. It is however more than enough to draw a *qualitative* Carter-Penrose diagram of the spacetime.

This qualitative Carter-Penrose diagram, which is actually a genuine Carter-Penrose diagram everywhere except for a small region near the the singular point of zero physical radius in the interior of the star, is given in fig. 1.3. It is quite informative to compare this diagram with the Carter-Penrose diagram of the maximal extensions of vacuum Schwarzschild spacetime in fig. 1.2. The exterior of the star, which is given by a portion of Schwarzschild spacetime, is represented in white and the interior of the star is represented in gray. In this diagram the black hole is not simply there, eternal, as it happens in the maximal extension of Schwarzschild spacetime, but it is formed by the gravitational collapse of a massive object. No white hole or second asymptotically flat exterior region (block III in fig. 1.2) ever forms in the creation of a black hole by gravitational collapse.

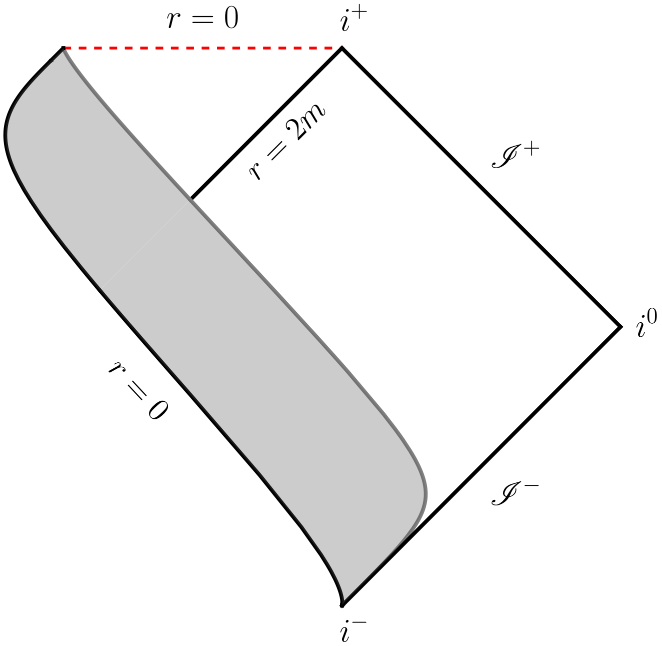

Figure 1.3: Qualitative Carter-Penrose diagram of the spacetime of the Oppenheimer-Snyder model. The interior of the star is represented in gray.

A black hole formed by gravitational collapse is usually called an astrophysical black hole due to its astrophysical origin. Another (hypothetical) type of black hole is a *primordial black hole*, formed in the early universe as a consequence of initial density perturbations. While these objects have been used in several theoretical scenarios and have been proposed to explain different experimental observations, their existence has yet to be proven.

1.2.3 White holes

In section 1.2.1 the concept of a white hole naturally emerged from the analysis of the maximal extension of Schwarzschild spacetime. The qualitative statement that a white hole is the "time-reverse" of a black hole is rigorously formalized as follows starting from the different definitions of a black hole. In terms of the global causal structure of spacetime, a white hole in an asymptotically flat spacetime can be defined as a region $\mathscr{V}$ in spacetime that is not contained in the causal future of past null infinity $\mathscr{I}^-$. The boundary $\partial\mathscr{V}$ of the region $\mathscr{V}$ is called the event horizon of the white hole. This definition raises the same difficulties already discussed in the black hole case.

The definition of white hole used in this thesis is given in terms of the same quasi-local geometric properties used for the black hole definition. Let then an *anti-trapped surface* be an orientable two-dimensional spacelike surface in spacetime such that the expansion Θ of both ingoing and outgoing congruences of null geodesics is positive on the whole surface. A white hole is defined as an *anti-trapped region*, that is a region in which every point belongs to an anti-trapped surface. The boundary of this anti-trapped region, which is a marginally anti-trapped surface, is called the (past) apparent horizon.

The same construction carried out in the last section for the Oppenheimer-Snyder model, but "time-reversed", can be carried out to construct the spacetime of a star emerging from the past singularity of the white while and then indefinitely expanding in the future. The interior and exterior metrics of the spacetime will still be given respectively by the FLRW metric and the Schwarzschild metric. But the trajectory of the boundary of the star would now be an expanding radial timelike geodesic emerging from the past singularity instead of an infalling radial timelike geodesic plunging into the black hole. This exact construction leads to a spacetime whose qualitative Carter-Penrose conformal diagram is given in fig. 1.4.

The exterior of the star, which is given by a portion of Schwarzschild spacetime, is represented in white and the interior of the star is represented in gray. It is however clear that this spacetime is still not physically reasonable. The white hole in this model is not formed due to astrophysical phenomena, but it is still simply there as was the case for the maximal extension of Schwarzschild spacetime. Furthermore, also the process of formation of matter from the past singularity is quite unclear. The physical relevance of white holes remains thus questionable.

Assuming however these objects exist, the gravitational field experienced by an observer in the exterior of both white hole and star would be the same gravitational field experienced by an observer in the exterior of both black hole

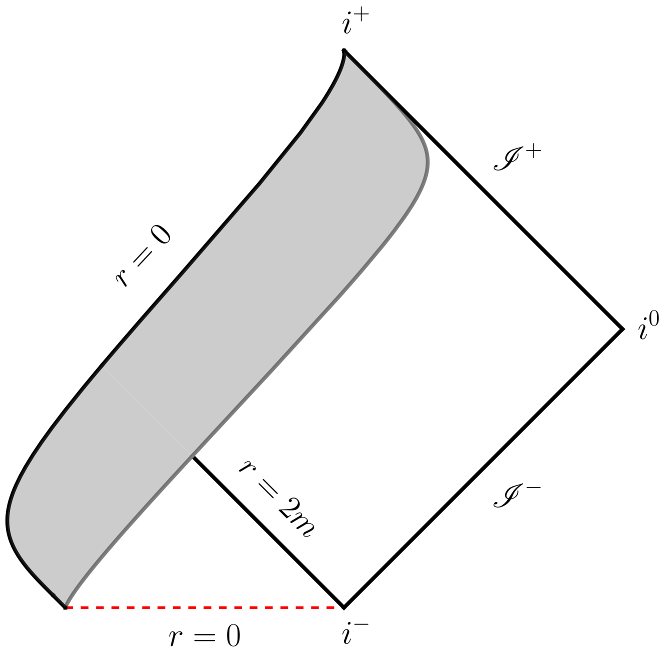

Figure 1.4: Qualitative Carter-Penrose diagram of the spacetime of a white hole.

and star in the Oppenheimer-Snyder model. An observer locally experiencing this gravitational field cannot tell the difference between the two scenarios. The distinction lies in the global structure of the spacetime. In the Oppenheimer-Snyder model, there is a collapsing star in the past and the observer can interact with it. This is not the case in the white hole spacetime. Conversely, in the white hole spacetime, there is an explosion of matter in the future that is absent in the black hole spacetime.

The first real interest in white holes began when Novikov [29] suggested the existence of primordial white holes (called "delayed-cores" or "lagging-cores") to explain quasars. These primordial white holes would have formed in the early universe as the result of a delayed expansion of some local regions in an expanding Friedmann universe. The conformal diagram of the spacetime describing these exploding white holes, after their formation, is exactly the one in fig. 1.4. It was however shown shortly after that exploding white holes are unstable under classical [30–32] and quantum [33] perturbations.

As a consequence of both the absence of any known astrophysical phenomena able to produce a white hole and the instability of the spacetime whose Carter-Penrose diagram is represented in fig. 1.4, white holes were deemed non-physical and the interest in these objects quickly faded. The black-to-white hole transition brings white holes back from oblivion by providing a tentative scenario for their astrophysical production.

1.2.4 Hawking evaporation

In the classical theory, a black hole interacting with its surroundings can only get bigger over time. Namely, its mass m and the surface area A of its apparent horizon can only grow with time. However, surprisingly enough, Hawking [34, 35] showed that, as soon as quantum field theory in curved spacetime is considered, this is no longer true. He indeed proved that a Schwarzschild black hole of mass m emits thermal radiation, the so-called *Hawking radiation*, like a black body at temperature (Planck units $\hbar = c = G = k_B = 1$)

$$T = \frac{1}{8\pi m} \ . \tag{1.78}$$

The first surprising consequence of this result is that considering only the contribution from massless fields for simplicity, an observer moving along $\mathscr{I}^+$ directly measures a non-vanishing flux F of energy

$$F(u) \propto \frac{1}{m^2} \tag{1.79}$$

coming from the black hole. Black holes are thus not completely black after all.

An even more striking consequence is that, by conservation of energy, a negative energy flux that is equal in magnitude to the flux in eq. (1.79) must flow into the black hole and decrease its total mass. This means that considering black holes to be isolated objects (namely neglecting the black hole accretion due to matter falling in), they are actually constantly “shrinking”. Specifically, the surface area A of their horizon is constantly decreasing due to the emission of Hawking radiation. This phenomenon is known as the *evaporation* of the black hole.

It is however important to stress that although the black hole evaporation causes its surface area A to shrink, the same is not necessarily true for its interior volume. In fact, the concept of "volume of the black hole" is not well defined. Any definition of such a concept will depend on a choice of foliation of its interior region. Nonetheless, it can be shown that for a physically reasonable choice of foliation, the interior volume of a black hole grows monotonically during the evaporation process [36, 37]. The final result of the evaporation process is then an object with a small external surface but a large interior volume.

To derive an accurate estimate of the black hole mass loss due to the evaporation process it is necessary to take into account the back-reaction of the quantum radiation over the Schwarzschild spacetime. This is accomplished by solving the *semiclassical Einstein field equations* [38], which are basically the classical Einstein field equations where the stress-energy tensor in the right-hand side includes the contribution coming from the expectation value of the stress-energy tensor operator of the quantum radiation field. This is unfortunately a nearly impossible task even in the simplest cases.

However, since the back-reaction effects near the black hole horizon should be small for a black hole whose mass m is much bigger than the *Planck mass* $m_{\mathrm{P}} := \sqrt{\hbar c/G}$, the black hole spacetime can be approximated by a locally Schwarzschild spacetime in which the mass m slowly decrease with time. The mass loss rate measured at $\mathscr{I}^+$ is then simply given by the negative energy flux entering the black hole horizon:

$$\frac{\mathrm{d}m(u)}{\mathrm{d}u} = -F(u) \propto -\frac{1}{m^2}\,. \tag{1.80}$$

The resulting mass profile is

$$m(u) = m_0\left(1 - \frac{u}{u_{\mathrm{P}}}\right)^{1/3}, \tag{1.81}$$

where u_{P} is approximately the retarded time at which the black hole reaches Planckian size (eq. (1.80) is no longer a good approximation when the black hole has Planckian size) and it is assumed that the black hole was formed at $u = 0$ with a mass m_0. It is then clear that an evaporating black hole reaches Planckian size in a finite retarded time roughly proportional to m_0^3.

This is a huge time for astrophysical black holes. The evaporation process of the smallest observed astrophysical black holes is estimated to last approximately 10^{58} times the current age of the universe [39], still assuming these black holes to be isolated objects, which are not. For primordial black holes, the situation is however different and there could be primordial black holes out there already in the final stage of their evaporation process.

The most controversial consequence of the evaporation process is surely the existence of a last stage of the black hole life. The nature of this final stage and the ultimate fate of the information that has fallen inside the black hole is the core of the renowned *information paradox* [40–42]. When the mass of the black hole reaches the Planck scale the curvature scalars near the horizon become Planckian and the quantum nature of the gravitational field can no longer be ignored. This means that Hawking's semiclassical approximation is no longer valid when the Planck mass is reached (but it could break down even before [43]) and that the proper description of the final stage of the black hole life belongs to the quantum gravity realm. Since however a fully developed and tested quantum theory of the gravitational field is still missing, the problem has been mainly addressed by making assumptions on the final stage of the black hole life and then studying their consequences. It is nonetheless crucial to stress that, being the final stage of the black hole life a quantum gravity phenomenon, any assumption about it is really an assumption about quantum gravity.

Several scenarios for the end of the life of a black hole have been proposed over the years. The first to suggest that something "unusual" had to happen at the end of the evaporation process was Hawking [44] himself. He assumed the complete evaporation as the final stage of the black hole life and studied the consequences of this choice. A guess of what the Carter-Penrose diagram of this spacetime might look like is given in fig. 1.5. It is important to stress that this is not a concrete Carter-Penrose diagram of the spacetime, not even qualitatively. In fact, there is not really a spacetime: There is no concrete spacetime metric

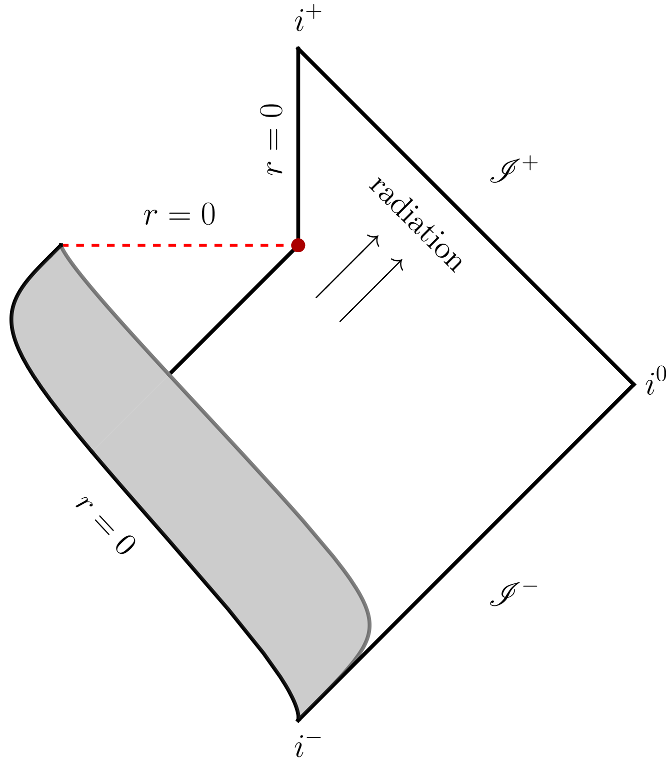

Figure 1.5: Guess of a Carter-Penrose diagram for the spacetime describing a complete evaporation of a black hole.

describing this scenario. So no genuine Carter-Penrose diagram of it can be constructed. While the diagram is tremendously useful to get the physical intuition behind the idea of complete evaporation, it should not be taken too seriously.

The white region of the diagram in the exterior of the collapsing star is supposed to represent a metric that is locally isomorphic to Schwarzschild. The 45° black line separating the interior and exterior of the black hole represents the event horizon of the black hole, which in this dynamical spacetime is different from the apparent horizon. The latter would instead be represented by a timelike curve. The red dot where the event horizon, curvature singularity, and future $r = 0$ line meet is the spacetime event/region where the complete evaporation takes place. It can be shown that any attempt to rigorously construct a spacetime metric producing a diagram of this sort would lead to this point being excised from spacetime and to the formation of a naked singularity [45]. In the future of the point of complete evaporation, spacetime continues as a portion of Minkowski spacetime (see fig. 1.1). Namely, as a portion of Schwarzschild spacetime with $m = 0$.

The original information loss paradox argument goes as follows. Prior to the black hole formation, the state of the quantum fields on spacetime can be represented by a pure density matrix. When the black hole has formed and the evaporation has begun, it can be shown [38] that the quantum state of the Hawking radiation reaching infinity is strongly correlated with the quantum state of the radiation fallen inside the black hole. Both states are singularly described by a mixed density matrix, but the total correlated state is still described by a pure density matrix. If after the last stage of his life, the black hole just ceases to exist, then all the radiation fallen inside it ceases to exist as well and the total state of the quantum fields is just given by the state describing the radiation at infinity. This quantum state is however described by a mixed density matrix. This means that the unitarity of the quantum evolution, which is at the core of standard quantum theory, and the information about the correlation between the two states are irretrievably lost.

Although the non-unitarity of the quantum evolution and the complete loss of information should not be considered lightly (it has however been argued that this might not be as unphysical as it may seems [46]), the true unphysical aspect of this scenario is the initial assumption of complete evaporation. As already stressed, the final stage of the black hole life belongs to the quantum gravity realm. So, to assume that the evaporation process continues after the Planck scale is equivalent to assume that the quantum nature of the gravitational field does not alter the picture of quantum field theory in curved spacetime. This is highly unrealistic. A more plausible interpretation of this scenario is the one in which the "complete evaporation" of the black hole at the end of the evaporation process is realized as a quantum transition of the Schwarzschild geometry near the horizon in the Minkowski geometry. However, none of the current tentative quantum theories of the gravitational field suggest or support this scenario. In fact, as it will be seen in detail in chapter 3, this scenario is not consistent with the physical picture independently emerging from the quantum description of the interior region of the black hole.

Excluding proposals that introduce new physics unrelated to the quantum nature of the gravitational field before the black hole reaches Planckian size, the alternatives to Hawking's proposal are principally two. In the first scenario, called *remnant scenario*, the black hole does not evaporate completely and the final stage of its life is a Planck mass object called *remnant*. In the second scenario the correlation information between the early Hawking radiation at infinity and the radiation inside the black hole is somehow transferred to Hawking radiation emitted at later times and no information is lost. Although originally proposed in the context of a complete evaporation of the black hole, many current formulations of this scenario remain agnostic about the last stage of life of the black hole.

Proponents of the second scenario often argue that the evaporating black hole no longer has enough internal states to be correctly correlated with the Hawking radiation at infinity long before the Planck scale is reached, at the so-called *Page time* [47]. Consequently, the information paradox would arise long before the quantum gravity realm is relevant and the second scenario would be the only viable option. These considerations are however made under the wrong assumption that the total number of internal states of a black hole can be calculated using its *Bekenstein-Hawking entropy*. The latter is in fact defined by the thermodynamical interaction of the black hole with its surroundings and it is thus only related to the degrees of freedom of the black hole that can actually interact with the exterior region. Since an observer in the exterior region can only probe the degrees of freedom of the horizon [48], it is not surprising that the Bekenstein-Hawking entropy is proportional to the area of the horizon. While the surface area A of the black hole horizon, and with it its Bekenstein-Hawking entropy, decreases monotonically during the evaporation process, the interior volume of the black hole, and with it the number of available internal states [49], grows monotonically [36, 37].

In the remnant scenario, the entire information of the radiation fallen inside the black hole is stored in some internal states of the remnant, which are thus strongly correlated with the Hawking radiation at infinity. Therefore, since the initial mass of the black hole, and with it the amount of radiation emitted, could be arbitrarily big, the total number of internal states of the remnant would have to be accordingly large in order to be correctly correlated with the Hawking radiation at infinity. There are two main arguments that are commonly made against the remnant scenario. First, it is argued that a remnant with a Planckian surface area cannot contain such an amount of internal states. Second, assuming such an object to exist, it is argued that the probability of their production in physical processes like scattering experiments at colliders should be very high. In fact, although their Planckian mass considerably suppresses their production rate, the "infinite" degeneracy of their internal structure would nonetheless make their production quite probable [50].

Both arguments once again make the wrong assumption that a remnant of Planckian surface area is an object of small internal volume. Given that the interior volume of a black hole, and with it the number of available internal states [49], grows monotonically during evaporation [36, 37], a hypothetical remnant formed in the last stage of the evaporation process would be an object with small external surface but large interior volume. This large interior volume is perfectly able to accommodate enough internal states to be correctly correlated with the Hawking radiation at infinity. Likewise, the computation of the remnants' production rate in scattering or other physical processes assumes that these processes can, in an appropriate limit, be described by an effective field theory where the remnants act as pointlike objects. But this is just not possible if the remnants are objects with a large interior volume. See Kazemian et al. [51] for a recent discussion of black hole remnants production in scattering processes.

I will argue that a natural and conservative scenario for the end of the life of a black hole is the one in which the black hole geometry undergoes a quantum transition in a white hole geometry. In this scenario, there is a unique asymptotically flat region in the exterior of the black-to-white hole and the black hole interior is a regular and well-defined region in which the trapped region undergoes a smooth transition in the interior anti-trapped region of the white hole. The resulting astrophysically produced white hole can be taken as a remnant. The internal states of the evaporating black hole and of the white hole remnant are given by the states of the quantum fields in the regular interior of the hole. Any particle that falls inside the black hole will simply follow its trajectory inside the regular interior of the black hole, passing through a region where the (semi)classical theory is no longer reliable, and quantum gravity effects must be taken into account. This means that the information contained in the radiation fallen inside the black hole and correlated with the Hawking radiation at infinity is not lost and it will just come out from the other end of the hole. In this scenario, no information paradox ever occurs.

1.2.5 The three quantum regions of a black hole spacetime

The description of a black hole presented in this section breaks down into three separate regions of spacetime:

- The spacelike curvature singularity in the vacuum region in the interior of the black hole;
- The singular point of vanishing physical radius in the interior of the star at the end of its collapse;
- The black hole horizon at the end of the evaporation process.

The spacelike singularity in the interior of the black hole is a spacetime region where the curvature invariants of spacetime suddenly diverge and where any wordline abruptly stops. Spacetime just terminates there and the predictive power of Einstein field equations is lost. The theory completely breaks down there. In fact, “infinity” is a mathematical concept that has no counterpart in the physical world and it should not be predicted for any physical quantity. In the interior region of the star, Einstein field equations predict the collapse of the entire star into a point of zero physical radius with “infinite” density (see eqs. (1.63) and (1.66)). Once again, this signals a breakdown of the theory. Finally, the equations describing the physics of the black hole horizon under evaporation are no longer valid when the horizon becomes Planckian, pointing out the breakdown of the semiclassical theory in that region.

These three regions have however something in common. In all three of them, the curvature scalars become Planckian, and consequently quantum gravitational effects become relevant. As a consequence, the results of the classical theory cannot be trusted in these regions and a complete quantum theory of the gravitational field is necessary to properly represent their physics. As it will be indeed explicitly shown in chapter 3, quantum gravity effects resolve the singularities present in the classical theory and spacetime continues beyond them.

The three separate regions in a black hole spacetime where the quantum nature of the gravitational field cannot be neglected are thus:

> **Region** $\mathscr{A}$: The subregion of the vacuum region in the interior of the black hole where the curvature becomes Planckian;
>
> **Region** $\mathscr{B}$: The spacetime region surrounding the black hole horizon when it reaches Planckian size at the end of the evaporation process;
>
> **Region** $\mathscr{C}$: The subregion of the interior of the star where both star density and curvature become Planckian.

They are qualitatively shown in dark grey in the spacetime diagram sketched in fig. 1.6. The onset of quantum gravitational effects in these regions is triggered by different physical phenomena in causally disconnected regions of spacetime. The quantum physics of these regions should then be studied separately and the results of the analyses should be appropriately matched afterwards.

1.3 Loop quantum gravity in a nutshell

Loop quantum gravity is simply the quantization of general relativity with a specific choice of elementary variables. As any quantum theory, it can be equally

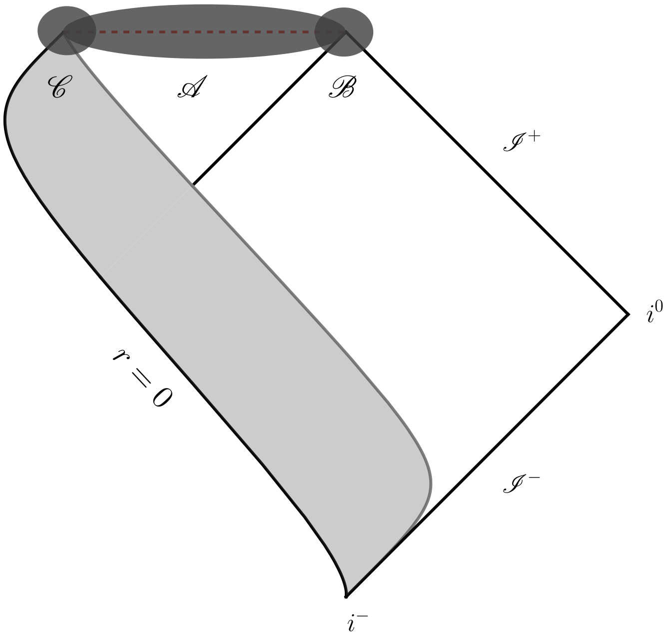

Figure 1.6: The three quantum regions of a black hole spacetime.

formulated canonically, by promoting the classical Poisson algebra to a set of commutation relations between operators living on a Hilbert space, or covariantly, via path integral techniques.

1.3.1 Canonical formulation

One of the fundamental aspects of the definition of the theory is the choice of elementary variables. The starting point of the canonical quantization of any classical theory is the Hamiltonian formulation of the theory. The Hamiltonian formulation of general relativity in the usual metric variables was pioneered by Dirac [52] and Arnowitt, Deser, and Misner [53]. Its canonical quantization, leading to the renowned Wheeler-DeWitt equation for the wavefunctional of the metric, was later carried out by DeWitt [54–56]. Although the Wheeler-DeWitt equation has been a fundamental tool in the development of a quantum theory of the gravitational field and it has great historical value [57], this theory is dramatically ill-defined and no mathematically rigorous quantum theory has been found using this formalism.

A big step forward in the direction of a quantum theory of the gravitational field was eventually made by Ashtekar [58, 59], who was able to reformulate the Hamiltonian theory of general relativity as a diffeomorphism invariant gauge theory for a gauge connection A. This reformulation of the theory allows us to express general relativity in the same language used for the other fundamental fields of nature. However, due to the non-trivial transformations of the connection and its conjugate momentum under the gauge symmetry on top of the diffeomorphism symmetry, the canonical quantization of the theory in these elementary variables would lead to a very complicated theory with no concrete predictive power.

These difficulties in rigorously defining a quantum theory of the gravitational field in terms of field elementary variables are not an accident, and there is a deep physical reason behind it. The connection field $A(x)$ stores the information about the parallel transport of an arbitrary vector along any infinitesimal direction starting from any spacetime point. The parallel transport of an arbitrary vector along any given curve in spacetime is instead controlled by the parallel propagator, also known as the *holonomy* in the quantum gravity literature, which is given by the path ordered exponential of the integral of the connection along the curve. The information contained in the connection field and in the set of all possible holonomies is equivalent: Given the connection, the holonomy along an arbitrary curve in spacetime can be defined as a sequence of several parallel transports between infinitesimally close points belonging to the curve; given the set of all the possible holonomies, the connection information can be defined through a limiting procedure of arbitrary short curves.

At the classical level, it is far easier to work with the connection. At the quantum level, however, the situation may change dramatically. In a quantum theory of the gravitational field, it is natural to consider the possibility of a quantized gravitational field. This however would mean that spacetime itself is quantized. In a discrete setting, while the finite information contained in the holonomies remains well-defined, the infinitesimal information contained in the connection loses any meaning and is not well-defined anymore. This strongly suggests abandoning the connection and searching for a quantum theory of the gravitational field using holonomies as fundamental variables.

This is indeed what loop quantum gravity does. Canonical loop quantum gravity is the canonical quantization of general relativity using holonomies of a generalization of the Ashtekar connection due to Barbero [60], known as Ashtekar-Barbero connection, as elementary variables.[2] This process results in the definition of a (kinematical) Hilbert space $\mathcal{H}$, an algebra of operators $\mathcal{A}$ living on it, and a Hamiltonian (constraint) operator $\widehat{H}$ which implements the dynamics in the quantum theory. All the details of this construction can be found in Rovelli [61] and in Thiemann [62].

Let a graph Γ be a collection of L oriented curves $\alpha_\ell \in \Sigma$, with $\ell = 1, \ldots, L$ and Σ being the three-dimensional manifold singled out by the choice of a coordinate time variable in the Hamiltonian formulation of the classical theory. Curves in this graph are called links and their source and target are called nodes. A generic node n of the graph is the target and the source of several different links. Let $\mathcal{H}_\Gamma$ be the Hilbert space of square-integrable functions $\psi(h_\ell)$ of the holonomies $h_\ell \in \mathrm{SU}(2)$ of the Ashtekar-Barbero connection along the links $\alpha_\ell \in \Gamma$ that are invariant under SU(2) gauge transformations. This space is often written as

$$\mathcal{H}_\Gamma = L^2\Big[\mathrm{SU}(2)^L / \, \mathrm{SU}(2)^N\Big]_\Gamma, \tag{1.82}$$

where N is the total number of nodes in the graph Γ. Using the Peter-Weyl theorem and the transformation properties of the holonomies under SU(2) gauge transformations it can be shown that a basis of this space can be labeled in the following way:

- A unitary irreducible representation of SU(2) labeled by the semi-integer j_ℓ and acting on the $(2j_\ell + 1)$-dimensional Hilbert space $\mathcal{H}_{j_\ell}$ is assigned to each link $\ell \in \Gamma$.

---

[2] The name *loop* quantum gravity comes from the original formulation of the theory where the elementary variables used for quantization were holonomies along closed curves, also known as loops.

- A basis element $i_{\rm n}$ of the Hilbert space

$$\mathcal{H}_{\rm n} := \mathrm{Inv}_{\mathrm{SU}(2)}\left[\bigotimes_{\ell\ni{\rm n}} \mathcal{H}_{j_\ell}\right], \tag{1.83}$$

  where $\bigotimes_{\ell\ni{\rm n}}$ is the direct product over all links ℓ having the node n either as source or target, is assigned to each node n. The Hilbert space $\mathcal{H}_{\rm n}$ is known as *intertwiner* space and its elements $i_{\rm n}$ are known as intertwiners.

This basis of $\mathcal{H}_\Gamma$ is known as *spin-network* basis [63]. The (kinematical) Hilbert space $\mathcal{H}$ of loop quantum gravity is the space of linear combinations of spin-network states, for all possible graphs Γ, that are invariant under the transformations generated by three-dimensional diffeomorphisms on Σ. While the proper mathematical construction of this Hilbert space is considerably complicated, its physical significance is pretty straightforward. A basis of this space is given by spin-network states defined on equivalence classes of graphs under three-dimensional diffeomorphisms. Namely, a basis of $\mathcal{H}$ is given by spin-network states whose graph Γ, which was defined as an object embedded in Σ, has lost all information except for its topology. Since equivalence classes of graphs under diffeomorphisms are called *knots*, the spin-network states in $\mathcal{H}$ are often called s-knots or knotted spin-networks.

A spin-network $|S\rangle \in \mathcal{H}$ is thus a triplet $S = \big(\Gamma, j_\ell, i_{\rm n}\big)$ composed of a graph Γ, which is a topological object made out of nodes n connected by links ℓ (see fig. 1.7), a quantum number j_ℓ assigned to each link $\ell \in \Gamma$ and a quantum number $i_{\rm n}$ assigned to each node ${\rm n} \in \Gamma$.

Classically, the gravitational field is the physical entity that endows the theory with a concept of geometry. It is thus natural to search for geometrical characteristics of the gravitational field in the quantum theory as well. The overall physical picture emerging from the canonical quantization process can be then studied using the area and the volume operators defined on $\mathcal{H}$ [64–66]. It turns out that spin-network states have a particularly simple geometric interpretation. By studying the *discrete* spectra of the area and the volume operators on the spin-network basis it is possible to assign the following geo-

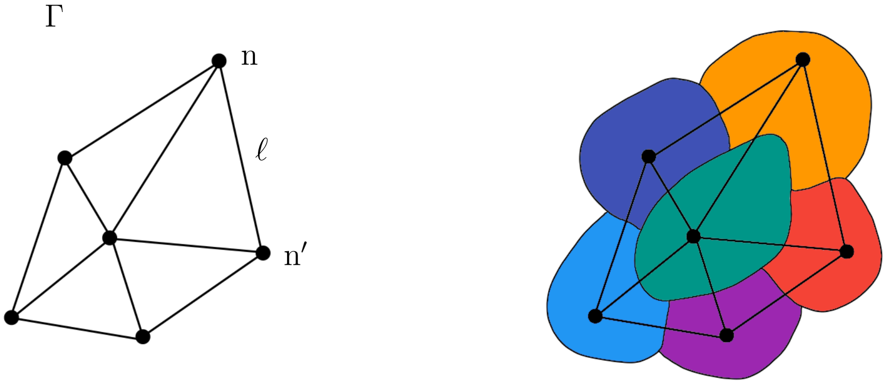

Figure 1.7: Visual representation of a spin-network state.

metrical interpretation to these states:

- Each node n represents an elementary quantum of space whose volume is determined by the quantum number i_{n};
- Two quanta of space (nodes) are adjacent if and only if they are connected by a link;
- Two adjacent quanta of space share an elementary quantum of surface whose value is determined by the quantum number j_ℓ.

A visual representation of this geometrical interpretation is shown in fig. 1.7.

Notice that the concept of manifold, which is a mathematical object devoid of any physical meaning that is conveniently used to construct the classical theory, disappears at the quantum level. The graph Γ of a spin-network in $\mathcal{H}$ is not embedded in any space manifold and it can be continuously deformed in any way without changing the information it contains, as the relevant information is only in its topological structure. In the quantum theory is thus apparent that there is not a space in which the quantum excitations of the gravitational field live, the quantum excitations of the gravitational field are space itself. The only possible localization is given by the adjacency relations provided by the topological graph.

Furthermore, since the area and the volume operators have discrete spectra [64], the theory exhibits an intrinsic discreteness of the quantum geometry.

The gravitational field manifests itself in discrete quanta at the quantum level. This discreteness is entirely a result of the quantum theory in the same way in which the discreteness of the energy levels of the harmonic oscillator is entirely a result of the non-relativistic quantum theory. It was not postulated or imposed in any way from the outside. In particular, the specific choice of elementary variables used for the quantization has nothing to do with it. Holonomies are elementary variables for *continuum* general relativity exactly as the Ashtekar-Barbero connection field or the metric field. They simply provide elementary variables that are still well-defined in a discrete setting.

While this "kinematical" level of the theory is well understood, the dynamical level, which consists in the construction of a unique and well-defined Hamiltonian operator $\widehat{H}$ on $\mathcal{H}$ and in the computation of its action on the spin-network basis, is far less developed. This is due to the very complicated form of the classical Hamiltonian. One of the several lines of research to overcome the difficulties in the dynamical level of the canonical theory is the covariant approach.

1.3.2 Spin-network histories and spin foams

The procedure to heuristically construct the path integral formulation of loop quantum gravity starting from the canonical theory formally mimics the procedure that is used to do the same in non-relativistic quantum mechanics.

Consider a one-dimensional non-relativistic system with mass m and Hamiltonian

$$H(q,p) = \frac{p^2}{2m} + V(q)\,, \tag{1.84}$$

where q and p are the canonical conjugate variables of the system. In the quantum theory, q and p are promoted to operators $\hat{q}$ and $\hat{p}$ acting on a Hilbert space $\overline{\mathcal{H}}$. The dynamics of the canonical quantum theory is defined using the time evolution operator $\widehat{U}(t'-t) = e^{-i(t'-t)\,\widehat{H}}$, where $\widehat{H}$ is the operator corresponding to the classical Hamiltonian in eq. (1.84) and $\hbar = 1$. The so-called *propagator* $W(q', t', q, t)$, whose squared modulus gives the probability of finding the system in the position q at time t and in the position q' at time t', is defined as

$$W(q', t', q, t) := \langle q' | \, \widehat{U}(t' - t) \, | q \rangle = \langle q' | \, e^{-i(t'-t)\,\widehat{H}} \, | q \rangle \ , \tag{1.85}$$

where $|q\rangle$ and $|q'\rangle$ are eigenstates of the $\widehat{q}$ observable on $\overline{\mathcal{H}}$. Partitioning the time interval $t' - t$ into I time intervals of equal duration $\epsilon := (t' - t)/I$, the propagator can be rewritten as

$$\begin{aligned} W(q', t', q, t) &= \langle q' | \, e^{-i(t'-t)\,\widehat{H}} \, | q \rangle = \langle q' | \left(e^{-i\epsilon\,\widehat{H}} \right)^{I} | q \rangle \\ &= \int \mathrm{d}q_1 \, \cdots \, \mathrm{d}q_{I-1} \, \langle q' | \, e^{-i\epsilon\,\widehat{H}} \, | q_{I-1} \rangle \cdots \langle q_1 | \, e^{-i\epsilon\,\widehat{H}} \, | q \rangle \ , \end{aligned} \tag{1.86}$$

where in the second line $I - 1$ resolutions of the identity $\mathbb{1} = \int \mathrm{d}\widetilde{q} \, |\widetilde{q}\rangle \langle \widetilde{q}|$ in $\overline{\mathcal{H}}$ were used. Explicitly computing the transition amplitudes of the form $\langle q_k | \, e^{-i\epsilon\,\widehat{H}} \, | q_{k-1} \rangle$, the propagator reads

$$W(q', t', q, t) \approx \left(\frac{m}{2\pi i \epsilon} \right)^{I/2} \int \mathrm{d}q_1 \cdots \mathrm{d}q_{I-1} \, \exp\left(i \sum_k \left[\frac{m v_k^2}{2} - V(q_k) \right] \epsilon \right) , \tag{1.87}$$

where $v_k := (q_k - q_{k-1})/\epsilon$ is the mean classical velocity in the k-th time interval and terms that vanish in the $\epsilon \to 0$ limit have been neglected.

The argument of the exponential function in eq. (1.87) can be seen as a Riemann sum converging to the integral in time of the classical Lagrangian in the limit of $\epsilon \to 0$. Namely,

$$\sum_k \left(\frac{m v_k^2}{2} - V(q_k) \right) \epsilon \quad \xrightarrow{\epsilon \to 0} \quad \int \mathrm{d}\tau \left[\frac{1}{2} m \dot{q}^2(\tau) - V\big(q(\tau)\big) \right] \equiv S[q(\tau)] \, , \tag{1.88}$$

where $S[q(\tau)]$ is the classical action of the system. Furthermore, in the limit $\epsilon \to 0$, which is equivalent to the $I \to +\infty$ limit, the set of points $\{q \, , \, q_1 \, , \, \cdots \, , \, q_{I-1} \, , \, q'\}$ represents a trajectory $q(\tau)$ starting in q at time $\tau = t$ and ending in q' at time $\tau = t'$. The weighted integral in eq. (1.87) can thus be seen as an integral, known as *path integral*, over all the possible trajectories $q(\tau)$ starting in q at time t and ending in q' at time t':

$$\left(\frac{m}{2\pi i\epsilon}\right)^{I/2}\int \mathrm{d}q_1\cdots\mathrm{d}q_{I-1}\quad\xrightarrow{\epsilon\to 0}\quad\int \mathrm{d}\big[q(\tau)\big]\,. \tag{1.89}$$

The propagator in eq. (1.85) can finally be rewritten in the $\epsilon\to 0$ limit as

$$W(q',t',q,t)=\int \mathrm{d}\big[q(\tau)\big]\,e^{iS[q(\tau)]}\,. \tag{1.90}$$

This is the expression of the propagator in the path integral formulation of non-relativistic quantum mechanics. Feynman [67] showed that, in the cases in which eq. (1.90) holds (the convergence of the path integral for a generic classical potential V is a non-trivial topic), an equivalent formulation of quantum mechanics in terms of path integrals, as opposed to the usual canonical theory, can be given. In the path integral formulation of quantum mechanics eq. (1.90) is taken as an axiom, from which the standard axioms of the canonical formulation, such as the canonical commutation relations, can be derived.

The same procedure can be formally carried out in canonical loop quantum gravity as well. The transition amplitude of interest corresponding to the non-relativistic propagator in eq. (1.85) is $\langle S'|\,\widehat{P}\,|S\rangle$, where $|S\rangle$ and $|S'\rangle$ are spin-network states in $\mathcal{H}$ and $\widehat{P}$ is

$$\widehat{P}:=\int \mathrm{d}\big[N(\vec{x})\big]\,e^{i\widehat{H}(N)}\,, \tag{1.91}$$

$$\widehat{H}(N):=\int_\Sigma \mathrm{d}^3x\,\widehat{H}(\vec{x})N(\vec{x})\,, \tag{1.92}$$

where Σ is a three-dimensional manifold singled out by the choice of a coordinate time variable in the Hamiltonian formulation of the classical theory, $H(\vec{x})$ is the Hamiltonian (constraint) density of the gravitational field on Σ, $N(\vec{x})$ is an appropriately defined test function and the integration over $N(\vec{x})$ is a functional integration just like the one in eq. (1.90). In the classical theory $H(N)$ is the generator of a diffeomorphism of parameter $N(\vec{x})$ along the normal to Σ. The differences between $\widehat{P}$ and the non-relativistic time evolution operator are due both to the difference in degrees of freedom between a field and a one-dimensional system and to the background independence of general relativity.

The transition amplitude of interest is then

$$\langle S'|\,\widehat{P}\,|S\,\rangle = \int \mathrm{d}\big[N(\vec{x})\big]\ \langle S'|\ e^{i\int_\Sigma \mathrm{d}^3x\,\widehat{H}(\vec{x})N(\vec{x})}\ |S\,\rangle\ . \tag{1.93}$$

Partitioning the parameter $N(\vec{x})$ into I smaller parameters $\epsilon(\vec{x}) := N(\vec{x})/I$ and using the resolution of the identity $\mathbb{1} = \sum_{\tilde{S}} |\tilde{S}\rangle\,\langle\tilde{S}|$ in $\mathcal{H}$, the expression in eq. (1.93) can be written in the following way:

$$\begin{aligned}\langle S'|\,\widehat{P}\,|S\,\rangle &= \int \mathrm{d}\big[N(\vec{x})\big]\ \langle S'|\ \left(e^{i\int_\Sigma \mathrm{d}^3x\,\widehat{H}(\vec{x})\,\epsilon(\vec{x})}\right)^I\ |S\,\rangle\\ &= \int \mathrm{d}\big[N(\vec{x})\big]\ \sum_{S_1}\cdots\sum_{S_{I-1}}\langle S'|\ e^{i\int_\Sigma \mathrm{d}^3x\,\widehat{H}(\vec{x})\,\epsilon(\vec{x})}\ |S_{I-1}\rangle\\ &\quad\times\langle S_{I-1}|\ e^{i\int_\Sigma \mathrm{d}^3x\,\widehat{H}(\vec{x})\,\epsilon(\vec{x})}\ |S_{I-2}\rangle\cdots\langle S_1|\ e^{i\int_\Sigma \mathrm{d}^3x\,\widehat{H}(\vec{x})\,\epsilon(\vec{x})}\,|S\,\rangle\ .\end{aligned} \tag{1.94}$$

Unfortunately, due to the difficulties in dealing with the action of the Hamiltonian (constraint) operator, it is not possible to rewrite this expression in a closed form as it was done in eq. (1.87) for the simpler case of the one-dimensional non-relativistic system. It is nonetheless possible to read the heuristic physical picture emerging from this construction.

The spin-network $|S\,\rangle$ can be pictured as living in the chosen spatial foliation Σ, while $|S'\rangle$ can be pictured as living in Σ', which is defined as the result of the classical action of $H(N)$ on Σ. In the limit in which $I \to +\infty$ the sequence of spin-networks $\{S\,,\,S_1\,,\,\cdots\,,\,S_{I-1}\,,\,S'\}$, also known as a *spin-network history*, represents a continuous two-dimensional foam-like structure connecting $|S\,\rangle$ on Σ to $|S'\rangle$ on Σ', in the same way in which the set of points $\{q\,,\,q_1\,,\,\cdots\,,\,q_{I-1}\,,\,q'\}$ represents a classical trajectory $q(\tau)$ connecting q to q' in the non-relativistic case. An example of this construction is reported in fig. 1.8. A spin-network history can be seen as the coordinate time evolution in the manifold of the spin-network $|S\,\rangle$ into the spin-network $|S'\rangle$. As the spin-network $|S\,\rangle$ moves through its history, its links and nodes form respectively *faces* and *edges* in the foam-like structure. Furthermore, these faces and edges inherit the quantum

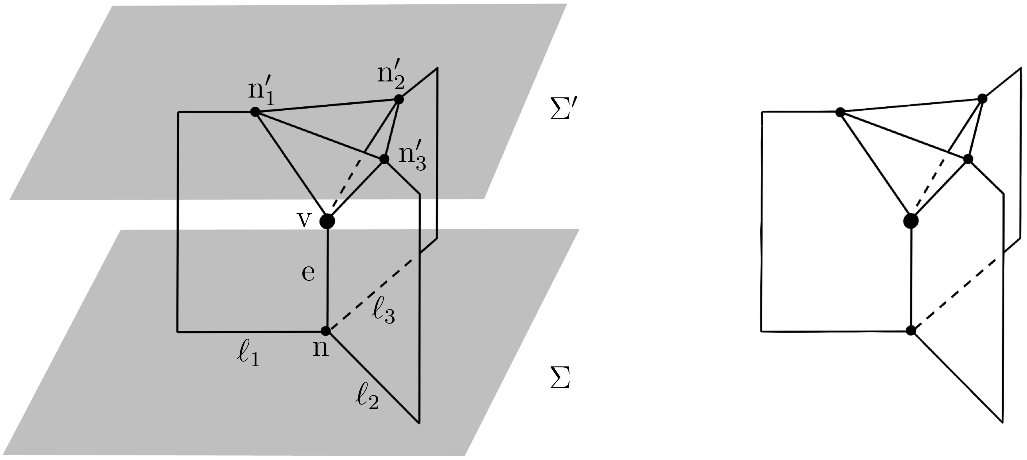

Figure 1.8: Example of a spin foam seen both as an embedded object in spacetime (left) and as a topological object (right).

numbers of the links and nodes creating them. A *colored* spin-network history, i.e. a spin-network history together with the assignment of quantum numbers on its faces and edges, is called a *spin foam.*

The amplitude associated with each spin foam depends on the matrix elements of the form

$$\langle S_n|\; e^{i\int_\Sigma \mathrm{d}^3x\, \widehat{H}(\vec{x})\,\epsilon(\vec{x})}\; |S_{n-1}\rangle \ . \tag{1.95}$$

Although a closed formula for these matrix elements is not available, a few properties of the action of the Hamiltonian operator on spin-network states are actually known. It is known for example that the Hamiltonian operator only acts on the nodes of the spin-network, possibly changing its graph in the vicinity of the node. The points in which the scalar constraint acts on a node and changes the topological structure of the spin-network are called *vertices* of the spin foam.

A spin foam is thus a triplet $\big(\mathcal{C}, j_{\mathrm{f}}, i_{\mathrm{e}}\big)$, where $\mathcal{C}$ is the topological object (known as *two-complex*) composed of vertices v, edges e and faces f defined by the dynamical evolution of the graph Γ of the spin-network $|S\rangle$, the labels j_{f} are quantum numbers assigned to the faces of $\mathcal{C}$ inherited from the quantum numbers j_ℓ assigned to the links of Γ and the labels i_{e} are quantum numbers assigned to the edges of $\mathcal{C}$ inherited from the quantum numbers i_{n} assigned to the nodes of Γ. The transition amplitude in eq. (1.93) can then be represented heuristically as a sum over all the possible spin foams connecting the two spin-networks $|S\rangle$ and $|S'\rangle$ of amplitudes determined by matrix elements similar to the one in eq. (1.95). The topological nature of the spin-network states and the functional integration over $N(\vec{x})$ in eq. (1.94) ensure that the result is invariant under four-dimensional diffeomorphisms. The spin foams considered in the sum should thus be seen as topological objects without any information about their location in the manifold (see fig. 1.8).

Since the amplitude associated with each spin foam is determined by the action of the Hamiltonian (constraint) operator, there is clearly no hope of properly defining a path integral version of the theory starting from the canonical one, at least not until the dynamical part of the canonical version of the theory is better understood. However, starting from the compelling physical picture that emerged from the canonical theory, another way to proceed is to study and properly define spin foam models as independent theories [68, 69]. Each model differs from the others by the choice of the actual spin foams to be considered in the sum and by the choice of the amplitude associated with each spin foam. Once a suitable definition and understanding of such theories is accomplished, the spin foam model describing quantum gravity must be singled out. This way of proceeding is both a way to directly define the dynamics of the theory bypassing the difficulties in dealing with the scalar constraint and an alternative way to study the scalar constraint itself [70, 71].

Interestingly, loop quantum gravity is not the only quantum gravity framework in which the concept of spin foam emerges. It is in fact not even the first. The notion that transition amplitudes in quantum gravity should be realized as a sum over surfaces was first advocated in Baez [72]. It seems that several different theories in one way or the other converge to the same physical idea. More on this can be found in Oriti [73].

1.3.3 Covariant formulation

Covariant loop quantum gravity is a tentative path integral formulation of quantum gravity that is meant to be a proper formalization of the heuristic picture emerging from the path integral reformulation of canonical loop quantum gravity. The mathematically rigorous definition of the theory is accomplished through a lattice discretization [74] very similar to Regge calculus [75] that naturally leads to the concept of spin foam. The continuum limit of the quantum theory is still under investigation and, as it happens in quantum chromodynamics, explicit calculations are performed in the discrete theory.

Given an arbitrary compact spacetime region $\mathcal{B}$ with boundary Σ, the lattice regularization procedure assigns to Σ a topological graph Γ and to $\mathcal{B}$ a topological two-complex $\mathcal{C}$ (that is a spin foam with no quantum numbers). A concrete implementation of this procedure will be carried out in chapter 4 in the context of the black-to-white hole transition. Let f, e and v $\in \mathcal{C}$ denote respectively a face, an edge, and a vertex of the two-complex $\mathcal{C}$. The discretization of the field variables of the continuum theory gives the following variables for the discrete theory[3] (see fig. 1.9):

1. To each *internal edge* e linking two vertices v and v′ are assigned two $\mathrm{SL}(2,\mathbb{C})$ elements $g_{\mathrm{ve}} = g_{\mathrm{ev}}^{-1}$ and $g_{\mathrm{ev'}} = g_{\mathrm{v'e}}^{-1}$.

2. To each *boundary edge* E linking an internal vertex v and a node n is assigned one $\mathrm{SL}(2,\mathbb{C})$ element $g_{\mathrm{vn}} = g_{\mathrm{nv}}^{-1}$.

3. To each link $\ell \in \Gamma$ is assigned one $\mathrm{SU}(2)$ element h_ℓ.

Then, the quantization procedure assigns to Σ a boundary Hilbert space $\mathcal{H}_\Gamma$ [76], which is exactly the subspace of the canonical Hilbert space $\mathcal{H}$ whose basis is given by the spin-network states having the fixed graph Γ as their topological

---

[3] The gauge symmetry of general relativity expressed in terms of a connection variable is really the Lorentz group, or its double cover $\mathrm{SL}(2,\mathbb{C})$. The gauge symmetry of the Hamiltonian formulation of the theory in Ashtekar-Barbero variables, and thus of the canonical quantum theory, is $\mathrm{SU}(2)$ because part of the symmetry has been gauge-fixed to better adapt it to the 3+1 splitting of the Hamiltonian formalism.

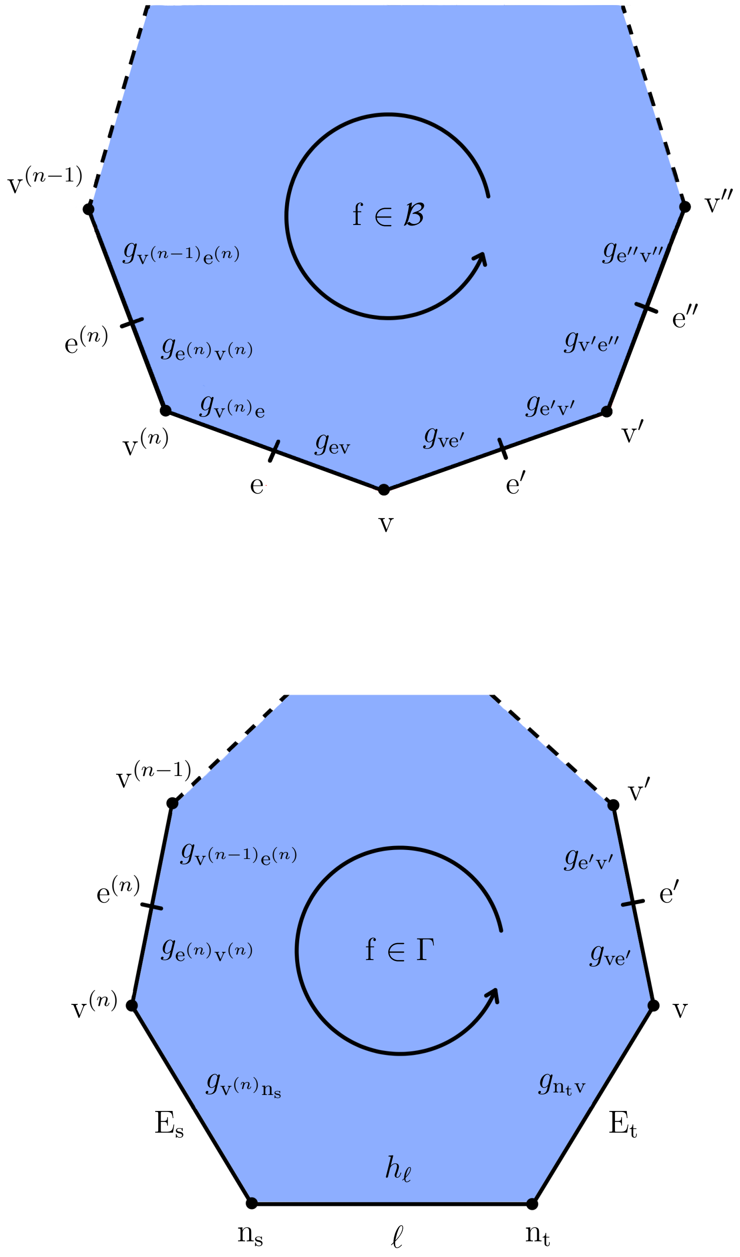

Figure 1.9: Internal (top) and boundary face (bottom) of the two-complex with the discrete group variables living on them.

graph. A state $|\psi\rangle \in \mathcal{H}_\Gamma$ can be represented as a square-integrable function $\psi(h_\ell)$, where $h_\ell \in \mathrm{SU}(2)$ can be seen as the holonomy of the Ashtekar-Barbero connection along the link $\ell \in \Gamma$, that is invariant under SU(2) gauge transformations.

Given an arbitrary boundary state $|\psi\rangle \in H_\Gamma$, the theory assigns to it a transition amplitude $W_{\mathcal{C}}\big[\psi\big] = \langle W_{\mathcal{C}}|\psi\rangle$ that is related to the probability of observing the gravitational field in the state $|\psi\rangle$ on Σ. The current state-of-the-art spin foam model for quantum gravity is the EPRL-KKL model [77–80]. The transition amplitude $W_{\mathcal{C}}\big[\psi\big]$ for this model can be conveniently written in terms of elementary face amplitudes in the following way:

$$\langle W_{\mathcal{C}}|\psi\rangle = \int_{\mathrm{SU}(2)} \left(\prod_{\ell\in\Gamma} \mathrm{d}h_\ell\right) W_{\mathcal{C}}\big(h_\ell\big)\, \psi\big(h_\ell\big)\,, \tag{1.96}$$

where the two-complex amplitude $W_{\mathcal{C}}\big(h_\ell\big)$ and the elementary face amplitudes $A_{\mathrm{f}}\big(g_{\mathrm{ve}}\big)$ and $A_{\mathrm{F}}\big(g_{\mathrm{ve}}, h_{\ell_{\mathrm{F}}}\big)$ are defined as

$$W_{\mathcal{C}}\big(h_\ell\big) = \int_{\mathrm{SL}(2,\mathbb{C})} \left[\prod_{\mathrm{v}\in\mathcal{C}} \widetilde{\prod_{\mathrm{e}\ni\mathrm{v}}} \mathrm{d}g_{\mathrm{ve}}\right] \left[\prod_{\mathrm{f}\in\mathcal{B}} A_{\mathrm{f}}\big(g_{\mathrm{ve}}\big)\right] \left[\prod_{\mathrm{F}\in\Gamma} A_{\mathrm{F}}\big(g_{\mathrm{ve}}, h_{\ell_{\mathrm{F}}}\big)\right], \tag{1.97}$$

$$\begin{aligned} A_{\mathrm{f}}\big(g_{\mathrm{ve}}\big) := \sum_{j_{\mathrm{f}}} d_{j_{\mathrm{f}}}\, \mathrm{Tr}\Big[&D^{(\gamma j_{\mathrm{f}}, j_{\mathrm{f}})}\big(g_{\mathrm{ev}} g_{\mathrm{ve'}}\big)\, D^{(\gamma j_{\mathrm{f}}, j_{\mathrm{f}})}\big(g_{\mathrm{e'v'}} g_{\mathrm{v'e''}}\big)\, \cdots \\ &\times\, \cdots\, D^{(\gamma j_{\mathrm{f}}, j_{\mathrm{f}})}\big(g_{\mathrm{e}^{(n)}\mathrm{v}^{(n)}} g_{\mathrm{v}^{(n)}\mathrm{e}}\big)\Big]\,, \end{aligned} \tag{1.98}$$

$$\begin{aligned} A_{\mathrm{F}}\big(g_{\mathrm{ve}}, h_{\ell_{\mathrm{F}}}\big) := \sum_{j_{\mathrm{F}}} d_{j_{\mathrm{F}}}\, \mathrm{Tr}\Big[&D^{(\gamma j_{\mathrm{F}}, j_{\mathrm{F}})}\big(g_{\mathrm{n}_t\mathrm{v}} g_{\mathrm{ve'}}\big) D^{(\gamma j_{\mathrm{F}}, j_{\mathrm{F}})}\big(g_{\mathrm{e'v'}} g_{\mathrm{v'e''}}\big)\, \cdots \\ &\times\, \cdots\, D^{(\gamma j_{\mathrm{F}}, j_{\mathrm{F}})}\big(g_{\mathrm{e}^{(n)}\mathrm{v}^{(n)}} g_{\mathrm{v}^{(n)}\mathrm{n}_s}\big) D^{(j_{\mathrm{F}})}\big(h_{\ell_{\mathrm{F}}}\big)\Big]\,. \end{aligned} \tag{1.99}$$

The symbol $\widetilde{\prod}_{\mathrm{e}\ni\mathrm{v}}$ stands for the product over all the edges e having the vertex v as either source or target, except for one, which can be chosen arbitrarily. It can indeed be shown [81, 82] that one integration per vertex in eq. (1.97) is redundant.

The two-complex amplitude $W_{\mathcal{C}}\big(h_\ell\big)$ is the integral over (almost) all the bulk $\mathrm{SL}(2,\mathbb{C})$ elements defined in items 1 and 2 of the product of one face amplitude for each face in the two-complex $\mathcal{C}$. An internal face of the two-complex is denoted as $\mathrm{f} \in \mathcal{B}$ and a boundary face, a face that contains a link, is denoted as $\mathrm{F} \in \Gamma$. A face amplitude is given by the sum over all its possible colorings j_{f} of the trace of the group elements living on its edges contracted following the pattern shown in fig. 1.9. The matrix $D^{(j)}$ is the Wigner matrix of the d_j-dimensional ($d_j = 2j + 1$) representation of SU(2). The matrix $D^{(p,k)}$ is the matrix of the (p, k) unitary irreducible representation of the principal series of $\mathrm{SL}(2, \mathbb{C})$. Notice that only the particular representations of the form $(p, k) = (\gamma j, j)$, γ being the *Barbero-Immirzi parameter*,[4] enter in the transition amplitude.

The transition amplitude of any spin foam model can be written in terms of elementary face amplitudes, or often also in terms of elementary vertex or wedge amplitudes. Different spin foam models have different elementary amplitudes. The specific amplitudes in eqs. (1.97) to (1.99) are the ones meant to properly formalize the quantities in eqs. (1.94) and (1.95) and provide a tentative spin foam model for quantum gravity. Although open issues remain [88], the EPRL-KKL model has shown many interesting properties in various physical applications. See Rovelli and Vidotto [89] for a pedagogical introduction to the model and for a somewhat outdated review of its physical applications.

In the heuristic path integral reformulation of the canonical theory, the transition amplitude was expressed as a sum over all the spin foams that are consistent with the boundary state, that is as a sum over all the two-complexes that are consistent with the boundary state and all their quantum numbers. The

---

[4] The classical action giving the Einstein field equations under variation is usually taken to be the Einstein-Hilbert action. It turns out however that the latter is not the most general one. There exists a term (actually more than one [83]), known as Holst term [84], that can be added to the Einstein-Hilbert action without affecting the classical equations of motion. The Barbero-Immirzi parameter is the coupling constant between the Einstein-Hilbert action and the Holst term. Since this new term does not change the classical equations of motion, the Holst and the Einstein-Hilbert actions (in vacuum) are classically equivalent and the Barbero-Immirzi parameter does not lead to any physically observable effect. This is no longer true in the quantum theory and the Barbero-Immirzi parameter explicitly enters in the construction of the theory. The physical interpretation of this parameter, which discriminates between unitarily inequivalent quantum theories [85], is still unclear [86, 87].

mathematically well-defined covariant loop quantum gravity transition amplitude in eqs. (1.96) to (1.99) can be shown to be a sum over all the consistent quantum numbers of the fixed two-complex $\mathcal{C}$. This is a natural consequence of the discretization process and the sum over spin foams must be recovered in the continuum limit of the theory. While physical predictions should be made using the continuum theory, it is actually fairly reasonable to assume that the transition amplitude of the continuum theory would be too complicated to be used in physical situations and that an approximation would be needed anyway. This is exactly how computations are performed in quantum chromodynamics. Even if the continuum limit of the discrete Wilson lattice theory is well defined, due to the challenging nature of the calculations involved in this limit the computations of physical quantities are more than often performed in the discrete theory. The results are accurate as long as the considered lattice is able to capture the relevant degrees of freedom of the continuum theory. Analogously, physical predictions obtained using the covariant loop quantum gravity transition amplitude in eqs. (1.96) to (1.99) are accurate as long as the two-complex $\mathcal{C}$ is sufficiently refined to capture the relevant degrees of freedom of the phenomenon studied.

Chapter 2

Global Kruskal-Szekeres coordinates for Reissner-Nordström spacetime

A version of this chapter has been published in Physical Review D as

F. Soltani. “Global Kruskal-Szekeres coordinates for Reissner–Nordström spacetime”. *Phys. Rev. D* **108** (2023), 124002. DOI: `10.1103/PhysRevD.108.124002`.

2.1 Introduction

The Reissner-Nordström geometry [16, 17] describes the gravitational field of an electrically charged spherically-symmetric static black hole. Although it only adds the presence of an electric charge to the Schwarzschild solution discussed in section 1.2.1, the global causal structure of this spacetime is considerably different from the causal structure of Schwarzschild spacetime, and it is strongly dependent on the relative strength of its gravitational mass m and its electric charge q.

A Reissner-Nordström spacetime with $m^2 > q^2$ is called *non-extremal* and, instead of a spacelike curvature singularity hidden behind a single horizon, it features a timelike curvature singularity concealed behind two separate horizons.

A Reissner-Nordström spacetime with $m^2 = q^2$ is called *extremal* and it features a timelike curvature singularity concealed behind a single horizon. In both cases, given the timelike nature of the singularity, a massive observer falling inside the black hole is not bound to end their wordline at the singularity, as it happens in the Schwarzschild solution, and so spacetime must continue in the future of the singularity. In fact, the conformal diagram of the maximal extension of both the extremal and the non-extremal Reissner-Nordström geometries consists of an infinitely periodic tower of asymptotically flat exterior regions connected to each other by black hole interiors. A Reissner-Nordström spacetime with $m^2 < q^2$ features a timelike curvature singularity which is not concealed by any horizon. It is thus a *naked singularity.* Since however the mass m of the black hole is a measure of the total energy of the system, including its electrostatic energy, the condition $m^2 < q^2$ implies that the total energy of the black hole is somehow smaller than its electrostatic energy alone. This case is therefore considered unphysical and I will not discuss it in the following.

The Reissner-Nordström spacetime is a strongly spherically symmetric spacetime. So all the results obtained in section 1.1.2 for arbitrary spherically symmetric spacetimes can be used for the description of this spacetime. Specifically, Eddington-Finkelstein coordinates and Kruskal-Szekeres coordinates can be used to cover part of the maximal extension of spacetime. Differently from the Kruskal-Szekeres coordinates in the maximal extension of Schwarzschild spacetime, where they provide a global coordinate chart, the standard Kruskal-Szekeres coordinate charts in Reissner-Nordström spacetime are adapted to a specific horizon and fail to cover any region beyond the other horizons.

The first global coordinate chart for the Carter-Penrose diagram of the maximal extension of Reissner-Nordström spacetime was found by Carter [7, 90]. These coordinates however provide only a continuous chart. A smooth generalization of this chart, though only available for the non-extremal case, was recently found by Schindler and Aguirre [13]. A different global coordinate chart for the Carter-Penrose diagram of non-extremal Reissner-Nordström spacetime is the one provided in Hawking and Ellis [91] and in Chandrasekhar [92]. This chart is analytic everywhere except at the inner horizon, where it is C^2, but the metric is degenerate at the inner horizon. These coordinates are then perfectly fine to visualize spacetime and study its causal and global aspects. Non-degeneracy is however needed to analyze more than just that.

In this chapter, I derive a smooth Kruskal-Szekeres coordinate chart that covers the entire maximal extension of both extremal and non-extremal Reissner-Nordström spacetime. This coordinate chart can be considered a smooth generalization of the C^1 global Kruskal-Szekeres coordinate chart derived in Hamilton [24]. Due to the particular causal and global structure of Reissner-Nordström spacetime, this generalized Kruskal-Szekeres chart already brings "infinity" at a finite coordinate position and no further compactification is needed to provide a coordinate chart for the Carter-Penrose diagram.

The only other smooth (analytic in fact) and global coordinate chart for the maximal extension of both extremal and non-extremal Reissner-Nordström geometry is the (Israel-)Klösch-Strobl coordinate chart[1] [93, 95]. While very interesting coordinates, they are however not relevant for the construction of Carter-Penrose diagrams, as they neither bring "infinity" at a finite coordinate position nor express the metric in double-null form.

Finally, the global Kruskal-Szekeres coordinate chart derived here is not specific to the Reissner-Nordström spacetime but it can be straightforwardly generalized to any strongly spherically symmetric spacetime as long as the tortoise coordinate $r_*(r)$ can be explicitly computed. They will indeed be used in the next chapter to draw the Carter-Penrose diagrams of the black-to-white hole spacetime.

The chapter is structured in the following way. In section 2.2 I briefly review the non-extremal Reissner-Nordström geometry and its causal and global structure. Standard inner and outer Kruskal-Szekeres coordinate charts are derived in section 2.3. The smooth and global Kruskal-Szekeres coordinate chart for the

---

[1] The Israel [93] coordinate chart provides a not widely known analytic and global covering of the maximal extension of the Schwarzschild geometry. The same coordinate chart was later rediscovered by Pajerski and Newman [94] and by Klösch and Strobl [95]. Israel [93] also provides a generalization of this chart to the non-extremal Reissner-Nordström geometry. However, as explained in Klösch and Strobl [95], this coordinate chart does not provide a global covering of the maximal extension of non-extremal Reissner-Nordström geometry.

non-extremal Reissner-Nordström spacetime is derived in section 2.4. Finally, I generalize this construction to the extremal case in section 2.5.

2.2 Non-extremal Reissner-Nordström spacetime

In Planck natural units $c = G = \hbar = 1$ and spherical coordinates (t, r, θ, ϕ) the metric of Reissner-Nordström spacetime reads

$$\mathrm{d}s^2 = -h(r)\,\mathrm{d}t^2 + h^{-1}(r)\,\mathrm{d}r^2 + r^2\,\mathrm{d}\Omega^2\,, \tag{2.1}$$

$$h(r) = 1 - \frac{2m}{r} + \frac{q^2}{r^2}\,, \tag{2.2}$$

where m and q are the mass and the electric charge of the black hole. It is a strongly spherically symmetric spacetime (see section 1.1.2) with defining function $f(r) = h(r)$.

Considering the non-extremal case of $m^2 > q^2$, the extremal case will be discussed in section 2.5, the function $h(r)$ has two zeroes $r_\pm = m \pm \sqrt{m^2 - q^2}$, which result in two different Killing horizons of the black hole: an *outer horizon* at $r = r_+$ and an *inner horizon* at $r = r_-$. The coordinate chart (t, r, θ, ϕ) can be used to separately cover all spacetime regions such that $0 < r < r_-$, $r_- < r < r_+$, or $r_+ < r < +\infty$. In the spacetime regions where $0 < r < r_-$ or $r_+ < r < +\infty$ the coordinates t and r are respectively timelike and spacelike and the metric is static, since the Killing vector field ∂_t is timelike. On the contrary, in the spacetime regions where $r_- < r < r_+$ t is spacelike and r is timelike. Furthermore, since ∂_t becomes spacelike, these spacetime regions are homogeneous but neither static nor stationary. The metric in eqs. (2.1) and (2.2) has coordinate singularities in $r = r_\pm$ and a curvature singularity in $r = 0$.

Instead of using the Eddington-Finkelstein and Kruskal-Szekeres coordinate charts to discover the causal structure of this spacetime and then represent it in a Carter-Penrose diagram, let me do the opposite: I will describe the properties of the various coordinate charts starting from the qualitative Carter-Penrose diagram of Reissner-Nordström spacetime in fig. 2.1. While this diagram has been only qualitatively drawn for the sake of simplicity, any of the coordinate charts mentioned above [7, 8, 90–92] can be used to draw a proper Carter-Penrose diagram.

The block division of the Carter-Penrose diagram of strongly spherically symmetric spacetimes discussed in section 1.1.2 is clearly shown in fig. 2.1. For later convenience, blocks where $r_+ < r < +\infty$ are labeled A_i, blocks where $r_- < r < r_+$ are labeled B_i, and blocks where $0 < r < r_-$ are labeled C_i. The index i takes values in $\mathbb{Z}$. From the diagram, it is clear that differently from Schwarzschild spacetime, an observer that falls inside the outer horizon is not bound to hit the curvature singularity but can instead exit the black hole interior into a second asymptotically flat exterior region in the future of the first one. In fact, there is an infinite tower of asymptotically flat exterior regions connected to each other by black hole interiors. B regions sharing future (past) horizons with C regions are trapped (anti-trapped). Interestingly, the curvature singularity in $r = 0$ is timelike instead of spacelike.

The coordinate system (t, r, θ, ϕ) can separately cover each one of the infinitely many regions A_i, B_i, and C_i, with the time coordinate t going to infinity on every horizon. The tortoise coordinate r_* satisfying $\mathrm{d}r_* = \mathrm{d}r/h(r)$ is given by

$$r_* = r + \frac{1}{2\kappa_+} \log\left|\frac{r}{r_+} - 1\right| + \frac{1}{2\kappa_-} \log\left|\frac{r}{r_-} - 1\right| + C\,, \tag{2.3}$$

where C is a constant of integration and

$$\kappa_\pm = \pm\frac{r_+ - r_-}{2r_\pm^2} \tag{2.4}$$

is the *surface gravity*[2] associated to the horizon $r_\pm$. Retarded and advanced

---

[2] The surface gravity κ of the horizon $r = 2m$ in Schwarzschild spacetime is given by $\kappa = 1/4m$.

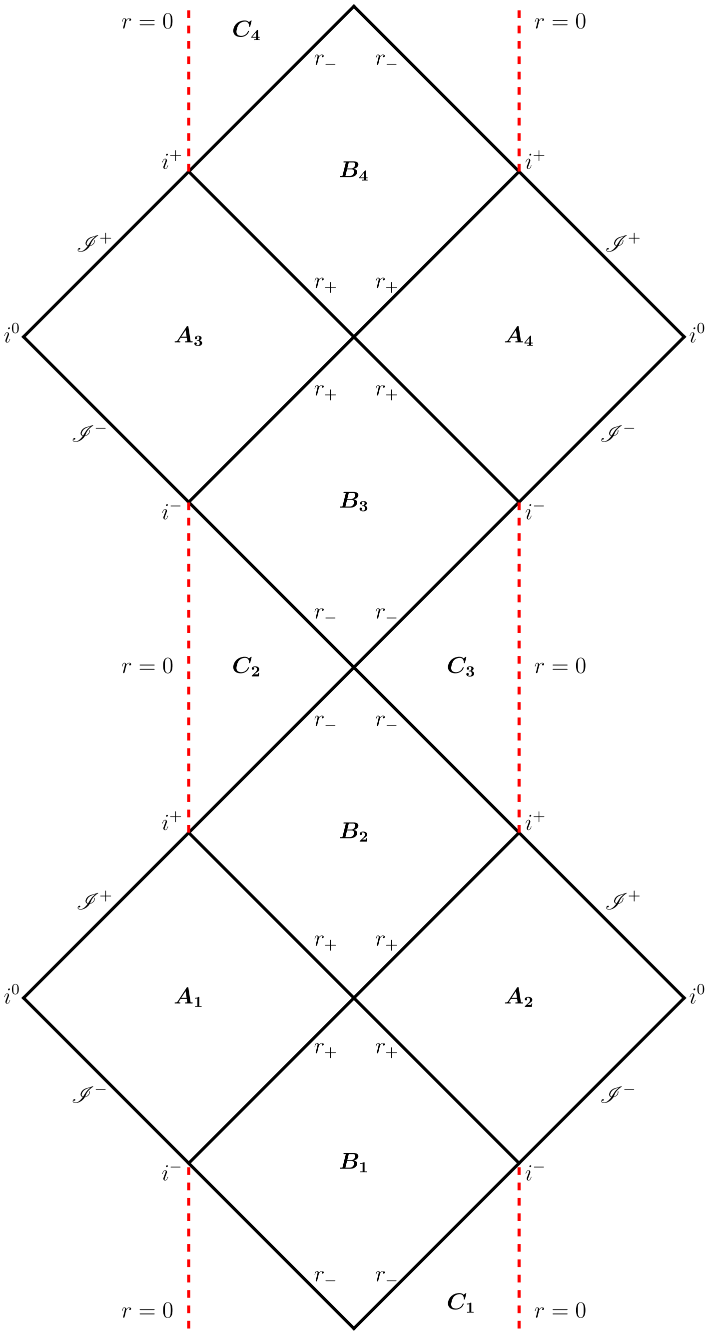

Figure 2.1: Qualitative Carter-Penrose diagram of the maximal extension of non-extremal Reissner-Nordström spacetime.

time null coordinates u and v then read

$$\begin{aligned} u =& t - r_*, \\ v =& t + r_*. \end{aligned} \tag{2.5}$$

The Reissner-Nordström metric in ingoing Eddington-Finkelstein coordinates (v, r, θ, ϕ) becomes

$$\mathrm{d}s^2 = -h(r)\,\mathrm{d}v^2 + 2\,\mathrm{d}v\,\mathrm{d}r + r^2\,\mathrm{d}\Omega^2\,. \tag{2.6}$$

The advanced time coordinate v is well behaved on all the horizons that are represented as 45° lines in the Carter-Penrose diagram, but it goes to infinity on the others. The ingoing Eddington-Finkelstein coordinate system is then able to separately cover all the spacetime regions between two consecutive −45° lines in fig. 2.1. Namely, it can be used to simultaneously cover regions A_1, B_1, and C_1, or regions A_2, B_2, and C_2, and so on.

Analogously, the retarded time coordinate u is well-behaved on all −45° line horizons and it goes to infinity on the others. Thus, the outgoing Eddington-Finkelstein coordinates (u, r, θ, ϕ) separately covers all the spacetime regions between two consecutive 45° lines in fig. 2.1. For example, it can be used to simultaneously cover regions A_1, B_2, and C_3, or regions A_4, B_3, and C_2, and so on.

As it always happens in strongly spherically symmetric spacetimes, although the coordinates u and v are separately well defined on several horizons, one or the other is not defined on every given horizon, and thus the double-null coordinate system (u, v, θ, ϕ) does not improve the spacetime coverage of the coordinate system (t, r, θ, ϕ). The Reissner-Nordström metric in the double-null coordinate system (u, v, θ, ϕ) reads

$$\mathrm{d}s^2 = -h(r)\,\mathrm{d}u\,\mathrm{d}v + r^2\,\mathrm{d}\Omega^2\,, \tag{2.7}$$

where $r = r(u, v)$ is implicitly defined by

$$r_*(r) = \frac{v-u}{2}\,. \tag{2.8}$$

2.3 Inner and outer Kruskal-Szekeres coordinates

The Kruskal-Szekeres coordinates provide a global double-null coordinate chart for Schwarzschild spacetime. Unfortunately, this is no longer true in strongly spherically symmetric spacetimes with a defining function $f(r)$ with more than one zero, as I will show in this section using the Reissner-Nordström spacetime as a working example. Standard Kruskal-Szekeres coordinates can be derived by studying the behavior of radial null geodesics in Eddington-Finkelstein coordinates as it was done for the Schwarzschild spacetime in section 1.2.1.

Consider for definiteness the spacetime regions A_2, B_2, and C_2 in fig. 2.1 covered in ingoing Eddington-Finkelstein coordinates. Given the metric in eq. (2.6), radial null geodesics must satisfy the equations

$$h(r)\dot{v}^2 - 2\dot{v}\dot{r} = 0 \tag{2.9}$$

(normalization of 4-velocity) and

$$h(r)\dot{v} - \dot{r} = E \tag{2.10}$$

(due to v-translation invariance), where the overdot means differentiation with respect to an affine parameter λ and E is the constant of motion associated with the v-translation invariance. A first set of solutions is given by geodesics satisfying

$$\dot{v} = 0\,, \qquad \dot{r} = -E\,, \tag{2.11}$$

that is

$$v(\lambda) = v_0\,, \qquad r(\lambda) = r_0 - E\lambda\,. \tag{2.12}$$

with v_0 and r_0 constants of integration. For $E > 0$ these solutions, valid for $\lambda \in (-\infty, r_0/E)$, describe future-oriented ingoing radial null geodesics starting out at past null infinity in A_2, diagonally crossing regions A_2, B_2, C_2 and then finally hitting the $r = 0$ curvature singularity at $\lambda = r_0/E$.

A different set of solutions, which by exclusion will describe outgoing radial null geodesics, satisfy

$$\dot{v} = \frac{2E}{h(r)}\,, \qquad\qquad \dot{r} = E\,. \tag{2.13}$$

For future-oriented geodesics, E must be taken negative in B_2 and positive in A_2 and C_2. Focusing on region B_2, and taking $E = -1$ and $r_0 = 0$ for simplicity, outgoing radial null geodesics are given by

$$r(\lambda) = -\lambda\,, \qquad \lambda \in (-r_+, -r_-)\,, \tag{2.14}$$

$$v(\lambda) = -2\lambda + \frac{1}{\kappa_+}\log\left|\frac{\lambda}{r_+} + 1\right| + \frac{1}{\kappa_-}\log\left|\frac{\lambda}{r_-} + 1\right| + K\,, \tag{2.15}$$

where K is a constant identifying different geodesics. These curves start at the past outer horizon between regions B_2 and A_1, that is $r \to r_+$ and $v \to -\infty$ for $\lambda \to (-r_+)^+$, cross diagonally region B_2 and end at the future inner horizon between regions B_2 and C_3, that is $r \to r_-$ and $v \to +\infty$ (notice that $\kappa_- < 0$) for $\lambda \to (-r_-)^-$. Naturally, these geodesics do not end at the two horizons, but the null coordinate v is not able to follow them past the horizons.

Once again, this analysis perfectly displays the physics of ingoing Eddington-Finkelstein coordinates. They are able to cover the full range of the affine parameter of ingoing radial null geodesics, as they are adapted to them, but they cover only a finite interval $\lambda \in (-r_+, -r_-)$ of the affine parameter of outgoing radial null geodesics in the full coordinate interval $v \in (-\infty, +\infty)$. The analysis itself however suggests the solution to the issue: the affine parameter λ is the natural coordinate to extend v beyond the horizons.

The same analysis performed in outgoing Eddington-Finkelstein coordinates covering regions A_1, B_2, and C_3 shows that future-oriented outgoing radial null geodesics are given by

$$u(\sigma) = u_0 \,, \qquad r(\sigma) = r_0 + E\sigma \,, \tag{2.16}$$

for an affine parameter $\sigma \in (-\infty, -r_0/E)$ and $E < 0$, while future-oriented ingoing radial null geodesics ($E = 1$ and $r_0 = 0$) in region B_2 are given by

$$r(\sigma) = -\sigma \,, \qquad \sigma \in (-r_+, -r_-) \,, \tag{2.17}$$

$$u(\sigma) = 2\sigma - \frac{1}{\kappa_+} \log\left|\frac{\sigma}{r_+} + 1\right| - \frac{1}{\kappa_-} \log\left|\frac{\sigma}{r_-} + 1\right| + K' \,, \tag{2.18}$$

where K' is a constant identifying different geodesics. Thus, only a finite interval $\sigma \in (-r_+, -r_-)$ of the affine parameter of ingoing radial null geodesics in region B_2 is covered in the full coordinate interval $u \in (-\infty, +\infty)$ and the affine parameter σ is the natural coordinate to extend u beyond the horizons.

So, starting from region B_2 in the null coordinate system (u, v, θ, ϕ), in order to obtain coordinates that are well defined on both the past outer horizons the discussion above suggests making the following change of coordinates (keeping only the leading term near the outer horizon in eqs. (2.15) and (2.18)):

$$u(U_+) = -\frac{1}{\kappa_+} \log|U_+| \,, \tag{2.19}$$

$$v(V_+) = \frac{1}{\kappa_+} \log|V_+| \,, \tag{2.20}$$

where U_+ and V_+ are adimensional null coordinates such that $U_+ > 0$ and $V_+ > 0$ in B_2 and the position of the outer horizons has been set to $U_+ = 0$ and $V_+ = 0$. The non-extremal Reissner-Nordström metric in (U_+, V_+, θ, ϕ) coordinates, also known as *outer Kruskal-Szekeres* double-null coordinates, reads

$$\mathrm{d}s^2 = \frac{1}{\kappa_+^2} \frac{h(r)}{U_+ V_+} \,\mathrm{d}U_+ \,\mathrm{d}V_+ + r^2 \,\mathrm{d}\Omega^2 \,, \tag{2.21}$$

where $r = r(U_+, V_+)$ is implicitly defined by eqs. (2.8), (2.19) and (2.20). It is straightforward to check that the metric tensor is indeed well-defined on both past outer horizons and that the outer Kruskal-Szekeres coordinates simultaneously cover regions A_1, B_1, A_2, and B_2, going to infinity on all inner horizons. These coordinates can in fact be used to separately cover all the "*quad-block*" regions of spacetime formed by four blocks of spacetime separated by outer horizons. E.g. A_1, B_1, A_2, and B_2, or A_3, B_3, A_4, and B_4, etc.

The transformation in eqs. (2.19) and (2.20) separately gives a well-defined diffeomorphism between (U_+, V_+, θ, ϕ) and (u, v, θ, ϕ) in each of the four blocks in the quad-block region covered by the outer Kruskal-Szekeres coordinates. Being the double-null coordinate system (u, v, θ, ϕ) singular on the horizons, also the transformation in eqs. (2.19) and (2.20) is ill defined there. The same is true also in eq. (1.47) for Schwarzschild spacetime.

Analogously, in order to obtain coordinates that are well defined on both the future inner horizons of the region B_2, *inner Kruskal-Szekeres* double-null coordinates (U_-, V_-) should be defined as

$$u(U_-) = -\frac{1}{\kappa_-} \log |U_- - 1| \,, \tag{2.22}$$

$$v(V_-) = \frac{1}{\kappa_-} \log |V_- - 1| \,, \tag{2.23}$$

where $U_- < 1$ and $V_- < 1$ in B_2 and the position of the inner horizons has been set to $U_- = 1$ and $V_- = 1$. The non-extremal Reissner-Nordström metric in inner Kruskal-Szekeres coordinates (U_-, V_-, θ, ϕ) reads

$$\mathrm{d}s^2 = \frac{1}{\kappa_-^2} \frac{h(r)}{(U_- - 1)(V_- - 1)} \, \mathrm{d}U_- \, \mathrm{d}V_- + r^2 \, \mathrm{d}\Omega^2 \,, \tag{2.24}$$

where $r = r(U_-, V_-)$ is implicitly defined by eqs. (2.8), (2.22) and (2.23). This metric tensor is well-defined on both future inner horizons and the inner Kruskal-Szekeres coordinates simultaneously cover regions B_2, C_2, B_3, and C_3 (or any quad-block region of spacetime formed by four blocks of spacetime separated by inner horizons), going to infinity on all outer horizons.

The transformation in eqs. (2.22) and (2.23) separately gives a well-defined diffeomorphism between (U_-, V_-, θ, ϕ) and (u, v, θ, ϕ) in each of the four blocks in the quad-block region covered by the inner Kruskal-Szekeres coordinates. Being the double-null coordinate system (u, v, θ, ϕ) singular on the horizons, also the transformation in eqs. (2.22) and (2.23) is ill defined there.

While these Kruskal-Szekeres coordinate charts for the non-extremal Reissner-Nordström spacetime are interesting coordinate systems, they are not as convenient as the Kruskal-Szekeres coordinate chart for Schwarzschild spacetime, which provides a global covering of the maximal extension of spacetime. This is however not a consequence of the intricate causal structure of Reissner-Nordström spacetime but rather an intrinsic limitation of the standard Kruskal-Szekeres coordinates. The Kruskal-Szekeres coordinate charts are intrinsically adapted to cover a single quad-block region of spacetime. They provide a global coordinate chart for the maximal extension of Schwarzschild spacetime simply because the latter is formed by a single quad-block region. In the next section, I generalize this standard construction in order to define a Kruskal-Szekeres coordinate chart covering the entire maximal extension of the non-extremal Reissner-Nordström geometry.

2.4 Global Kruskal-Szekeres coordinate chart

Let me start with finding a Kruskal-Szekeres coordinate chart covering region B_2 that is well behaved on both its inner and outer horizons at the same time. From the discussion in the previous section, the natural choice for such coordinates would be

$$u(\bar{U}) = -\frac{1}{\kappa_+}\log|\bar{U}| - \frac{1}{\kappa_-}\log|\bar{U}-1|\,, \tag{2.25}$$

$$v(\bar{V}) = \frac{1}{\kappa_+}\log|\bar{V}| + \frac{1}{\kappa_-}\log|\bar{V}-1|, \tag{2.26}$$

where $\bar{U}$ and $\bar{V}$ are adimensional null coordinates such that the outer horizons have been set to $\bar{U}=0$, $\bar{V}=0$ and the inner horizons have been set to $\bar{U}=1$, $\bar{V}=1$. It is however straightforward to see that this is not a well-defined change of coordinate, as the function $v(\bar{V})$ $(u(\bar{U}))$ is not separately monotonic in each of the regions

$$\begin{aligned} \bar{V} &< 0 \qquad (\bar{U} < 0)\,, \\ 0 < \bar{V} &< 1 \qquad (0 < \bar{U} < 1)\,, \\ \bar{V} &> 1 \qquad (\bar{U} > 1)\,. \end{aligned}$$

Focusing on the behavior of $v(\bar{V})$ shown in the top panel of fig. 2.2 for a specific choice of m and q, the problem is that the logarithm associated to the outer horizon at $\bar{V} = 0$ dominates the asymptotic behavior of $v(\bar{V})$ in both $\bar{V} < 0$ and $\bar{V} > 1$, while it should only dominate in $\bar{V} < 0$, with the other logarithm dominating the asymptotic behavior in $\bar{V} > 1$. This issue can be taken care of with a smooth transition function that interpolates between 0 and 1 in such a way that, when multiplied by the logarithms, it ensures that their contribution is only restricted to the desired regions.

Consider in fact the function

$$g_{\uparrow}(X) = \frac{F(X)}{F(X) + F(1-X)}\,, \tag{2.27}$$

with

$$F(X) = \begin{cases} 0 & X \leq 0\,, \\ e^{-1/X} & X > 0\,. \end{cases} \tag{2.28}$$

The function $g_{\uparrow}(X)$ is smooth, it satisfies $g_{\uparrow}(X) = 0$ for $X \leq 0$ and $g_{\uparrow}(X) = 1$ for $X \geq 1$, and its derivatives of all orders in $X = 0$ and $X = 1$ are vanishing. It is thus a function that smoothly interpolates between 0 and 1 in the interval $X \in [0, 1]$. A function that smoothly interpolates between 1 and 0 in the interval $X \in [0, 1]$ is given by

$$g_{\downarrow}(X) = 1 - g_{\uparrow}(X)\,. \tag{2.29}$$

These functions, whose behavior is plotted in fig. 2.3, can be used to modify the change of coordinate in eqs. (2.25) and (2.26) in the following way:

$$u(\widetilde{U}) = -\frac{1}{\kappa_+} g_{\downarrow}(\widetilde{U}) \log|\widetilde{U}| - \frac{1}{\kappa_-} g_{\uparrow}(\widetilde{U}) \log|\widetilde{U} - 1|\,, \tag{2.30}$$

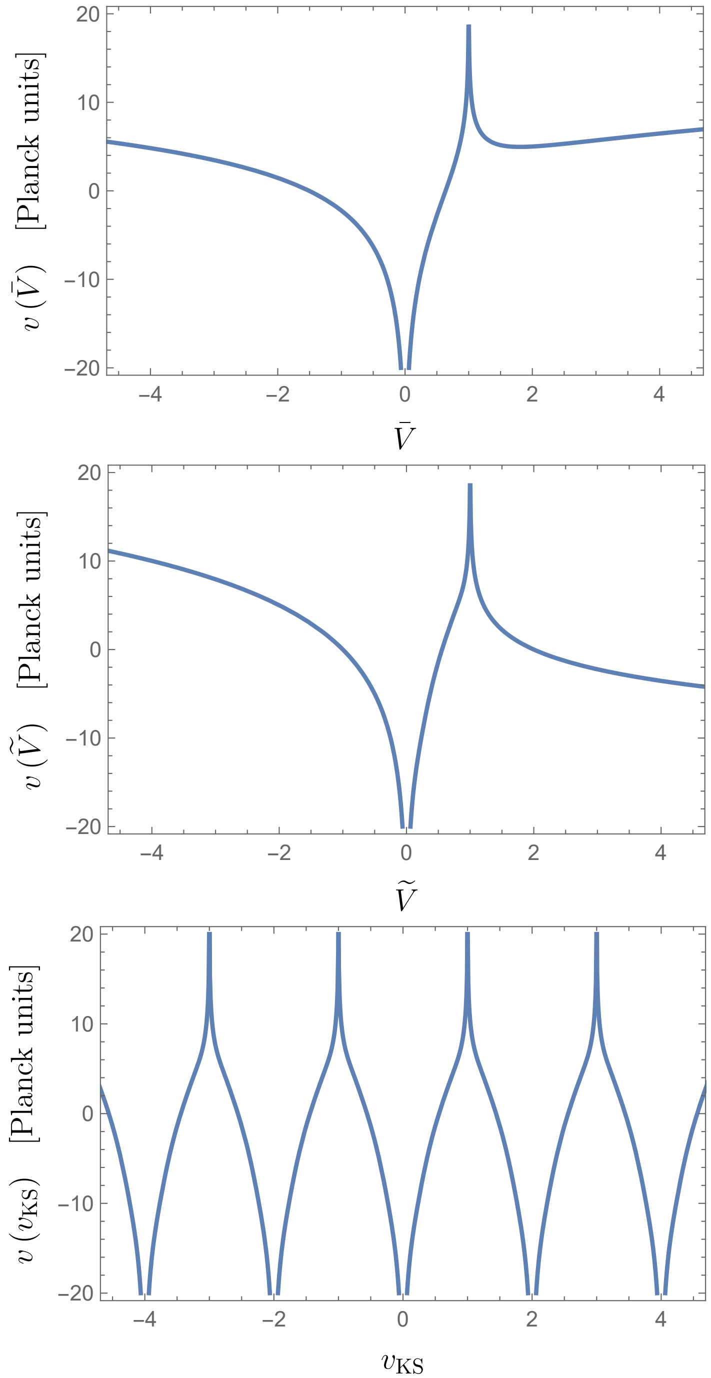

Figure 2.2: Plot of $v(\bar{V})$ in eq. (2.26) (top), $v(\widetilde{V})$ in eq. (2.31) (center), and $v(v_{\mathrm{KS}})$ in eq. (2.35) (bottom) with $m = 1$ and $q = 0.98$ (Planck units).

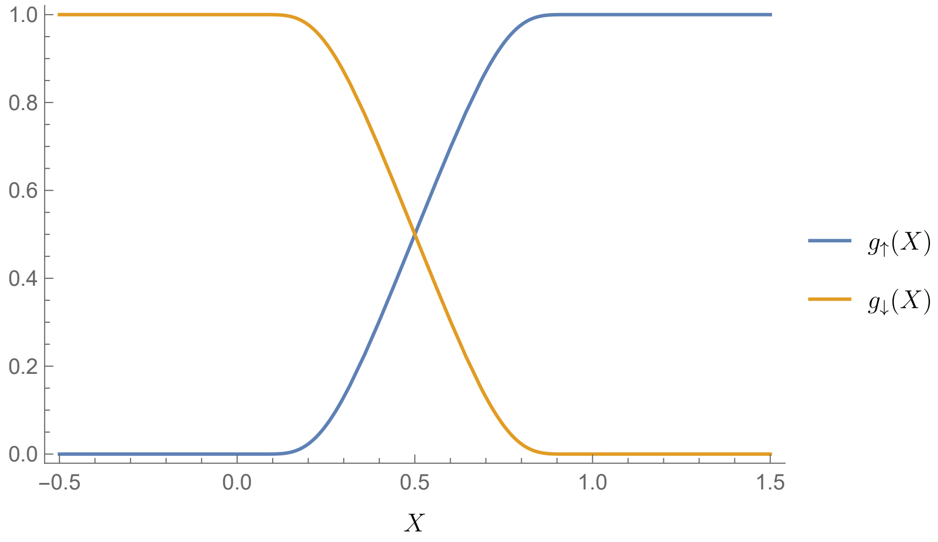

Figure 2.3: Plot of the smooth transition functions $g_\uparrow(X)$ and $g_\downarrow(X)$ defined in eqs. (2.27) and (2.29).

$$v(\widetilde{V}) = \frac{1}{\kappa_+} g_\downarrow(\widetilde{V}) \log|\widetilde{V}| + \frac{1}{\kappa_-} g_\uparrow(\widetilde{V}) \log|\widetilde{V} - 1|. \tag{2.31}$$

The function $v(\widetilde{V})$ $(u(\widetilde{U}))$ is now separately monotonic in each of the regions

$$\begin{aligned} \widetilde{V} &< 0 \qquad (\widetilde{U} < 0)\,, \\ 0 < \widetilde{V} &< 1 \qquad (0 < \widetilde{U} < 1)\,, \\ \widetilde{V} &> 1 \qquad (\widetilde{U} > 1)\,, \end{aligned}$$

as it can be checked from the plot of $v(\widetilde{V})$ in the center panel of fig. 2.2. The non-extremal Reissner-Nordström metric in these double-horizon-penetrating Kruskal-Szekeres coordinates $(\widetilde{U}, \widetilde{V}, \theta, \phi)$ reads

$$\mathrm{d}s^2 = h(r)\widetilde{f}(\widetilde{U})\widetilde{f}(\widetilde{V})\,\mathrm{d}\widetilde{U}\,\mathrm{d}\widetilde{V} + r^2\,\mathrm{d}\Omega^2\,, \tag{2.32}$$

where $r = r(\widetilde{U}, \widetilde{V})$ is implicitly defined by eqs. (2.8), (2.30) and (2.31) and

$$\begin{aligned}\widetilde{f}(X) =& \frac{1}{\kappa_+} g'_\downarrow(X) \log|X| + \frac{1}{\kappa_+}\frac{g_\downarrow(X)}{X} \\ &+ \frac{1}{\kappa_-} g'_\uparrow(X) \log|X-1| + \frac{1}{\kappa_-}\frac{g_\uparrow(X)}{X-1}\,.\end{aligned} \tag{2.33}$$

The metric tensor in eq. (2.32) is indeed well defined on all outer and inner horizons bounding region B_2. The coordinate chart $(\widetilde{U}, \widetilde{V}, \theta, \phi)$ simultaneously cover regions A_1, B_1, A_2, B_2, C_2, B_3, and C_3 of fig. 2.1, going to infinity on the past inner horizons bounding B_1 and the future outer horizons bounding B_3. They can in fact be used to separately cover all the multi-block regions of spacetime such as the one just described.

The transformation in eqs. (2.30) and (2.31) separately gives a well-defined diffeomorphism between $(\widetilde{U}, \widetilde{V}, \theta, \phi)$ and (u, v, θ, ϕ) in each block of spacetime covered by $(\widetilde{U}, \widetilde{V}, \theta, \phi)$, even if an analytical expression for the inverse transformation cannot be given. In fact, restricting the attention to block B_2 ($0 < \widetilde{U} < 1$, $0 < \widetilde{V} < 1$), the strict monotonicity of $u(\widetilde{U})$ and $v(\widetilde{V})$ in this region ensures the invertibility of the transformation and the inverse function theorem ensures the differentiability of its inverse.[3] Being the double-null coordinate system (u, v, θ, ϕ) singular on the horizons, also the transformation in eqs. (2.30) and (2.31) is ill defined there.

The construction of a Kruskal-Szekeres coordinate chart able to simultaneously cover two successive outer and inner horizons was thus successful. A Kruskal-Szekeres coordinate chart able to simultaneously cover two successive inner and outer horizons can be constructed analogously. However, not much would be gained by this. Let me thus go directly to the construction of a global Kruskal-Szekeres coordinate chart covering the entire maximal extension of non-extremal Reissner-Nordström spacetime with its infinite tower of asymptotic regions and black hole interiors.

The way to accomplish this is to use the same method used to cover two

---

[3] In the general case the statement of the inverse function theorem holds true only locally. However, for real functions of one real variable, the statement holds true globally.

successive horizons, but multiple times, in such a way as to cover the infinite tower of horizons. Consider in fact the following change of coordinates:

$$u(u_{\mathrm{KS}}) = \begin{cases} \qquad\vdots & \\ \begin{aligned} &-\frac{1}{\kappa_+} g_{\uparrow}(u_{\mathrm{KS}}, 2n-1, 2n) \log|u_{\mathrm{KS}} - 2n| + \\ &\quad -\frac{1}{\kappa_-} g_{\downarrow}(u_{\mathrm{KS}}, 2n-1, 2n) \log|u_{\mathrm{KS}} - (2n-1)| \end{aligned} & 2n-1 < u_{\mathrm{KS}} < 2n\,, \\ \begin{aligned} &-\frac{1}{\kappa_+} g_{\downarrow}(u_{\mathrm{KS}}, 2n, 2n+1) \log|u_{\mathrm{KS}} - 2n| + \\ &\quad -\frac{1}{\kappa_-} g_{\uparrow}(u_{\mathrm{KS}}, 2n, 2n+1) \log|u_{\mathrm{KS}} - (2n+1)| \end{aligned} & 2n < u_{\mathrm{KS}} < 2n+1\,, \\ \qquad\vdots & \end{cases} \tag{2.34}$$

$$v(v_{\mathrm{KS}}) = \begin{cases} \qquad\vdots & \\ \begin{aligned} &\frac{1}{\kappa_+} g_{\uparrow}(v_{\mathrm{KS}}, 2n-1, 2n) \log|v_{\mathrm{KS}} - 2n| + \\ &\quad +\frac{1}{\kappa_-} g_{\downarrow}(v_{\mathrm{KS}}, 2n-1, 2n) \log|v_{\mathrm{KS}} - (2n-1)| \end{aligned} & 2n-1 < v_{\mathrm{KS}} < 2n\,, \\ \begin{aligned} &\frac{1}{\kappa_+} g_{\downarrow}(v_{\mathrm{KS}}, 2n, 2n+1) \log|v_{\mathrm{KS}} - 2n| + \\ &\quad +\frac{1}{\kappa_-} g_{\uparrow}(v_{\mathrm{KS}}, 2n, 2n+1) \log|v_{\mathrm{KS}} - (2n+1)| \end{aligned} & 2n < v_{\mathrm{KS}} < 2n+1\,, \\ \qquad\vdots & \end{cases} \tag{2.35}$$

with $n \in \mathbb{Z}$ and $g_{\uparrow\downarrow}(X, a, b) = g_{\uparrow\downarrow}\big(\frac{X-a}{b-a}\big)$ being smoothly transition functions in $X \in [a, b]$. The function $v(v_{\mathrm{KS}})$ is plotted in the bottom panel of fig. 2.2. The position of the horizons in the $(u_{\mathrm{KS}}, v_{\mathrm{KS}})$ coordinates is arbitrary. I made the choice $u_{\mathrm{KS}} = n$ and $v_{\mathrm{KS}} = n$ for $n \in \mathbb{Z}$.

Defining the function $f(X)$ in such a way that $v'(v_{\mathrm{KS}}) = f(v_{\mathrm{KS}})$ and $u'(u_{\mathrm{KS}}) = -f(u_{\mathrm{KS}})$, the non-extremal Reissner-Nordström metric in the Kruskal-Szekeres coordinates $(u_{\mathrm{KS}}, v_{\mathrm{KS}}, \theta, \phi)$ reads

$$\mathrm{d}s^2 = h(r) f(u_{\mathrm{KS}}) f(v_{\mathrm{KS}})\, \mathrm{d}u_{\mathrm{KS}}\, \mathrm{d}v_{\mathrm{KS}} + r^2\, \mathrm{d}\Omega^2\,, \tag{2.36}$$

where $r = r(u_{\mathrm{KS}}, v_{\mathrm{KS}})$ is implicitly defined by eqs. (2.8), (2.34) and (2.35). These equations can then be used to study the regularity of both the function $r(u_{\mathrm{KS}}, v_{\mathrm{KS}})$ itself and of the metric tensor near the horizons. The analysis is carried out exactly as it is carried out for the standard inner and outer Kruskal-Szekeres coordinates, and it shows that the metric tensor is well behaved on all spacetime horizons and that these generalized Kruskal-Szekeres double-null coordinates $(u_{\mathrm{KS}}, v_{\mathrm{KS}}, \theta, \phi)$ provide a smooth and global chart for the maximal extension of the non-extremal Reissner-Nordström geometry.

The transformation in eqs. (2.34) and (2.35) separately gives a well-defined diffeomorphism between $(u_{\mathrm{KS}}, v_{\mathrm{KS}}, \theta, \phi)$ and (u, v, θ, ϕ) in each block of spacetime covered by $(u_{\mathrm{KS}}, v_{\mathrm{KS}}, \theta, \phi)$, even if an analytical expression for the inverse transformation cannot be given. Once again, this is ensured by the strict monotonicity of $u(u_{\mathrm{KS}})$ and $v(v_{\mathrm{KS}})$ (see fig. 2.2) in each spacetime block and by the inverse function theorem. Being the double-null coordinates (u, v, θ, ϕ) singular on the horizons, also the transformation in eqs. (2.34) and (2.35) is ill defined there.

Kruskal-Szekeres spatial x_{KS} and temporal t_{KS} coordinates can be defined as

$$t_{KS} = v_{\mathrm{KS}} + u_{\mathrm{KS}}\,, \qquad x_{KS} = v_{\mathrm{KS}} - u_{\mathrm{KS}}\,. \tag{2.37}$$

The Kruskal-Szekeres spacetime diagram of the maximal extension of non-extremal Reissner-Nordström spacetime is reported in fig. 2.4. This diagram is very similar to the qualitative Carter-Penrose diagram shown in fig. 2.1. In fact, since the radial light cones are tilted at ±45° and spacetime "infinity" is at a finite coordinate position, the spacetime diagram in fig. 2.4 is actually a genuine Carter-Penrose diagram. The reason why no explicit compactification was needed is that future and past null infinity of the asymptotically flat exterior regions are located at the same Eddington-Finkelstein coordinate value, either $v \to \pm\infty$ or $u \to \pm\infty$, of the inner horizons. So, since the inner horizons are at a finite coordinate value in the global Kruskal-Szekeres coordinates, so are future and past null infinity of the exterior asymptotically flat regions.

The peculiar shape of the curves of constant t and r, and with them the

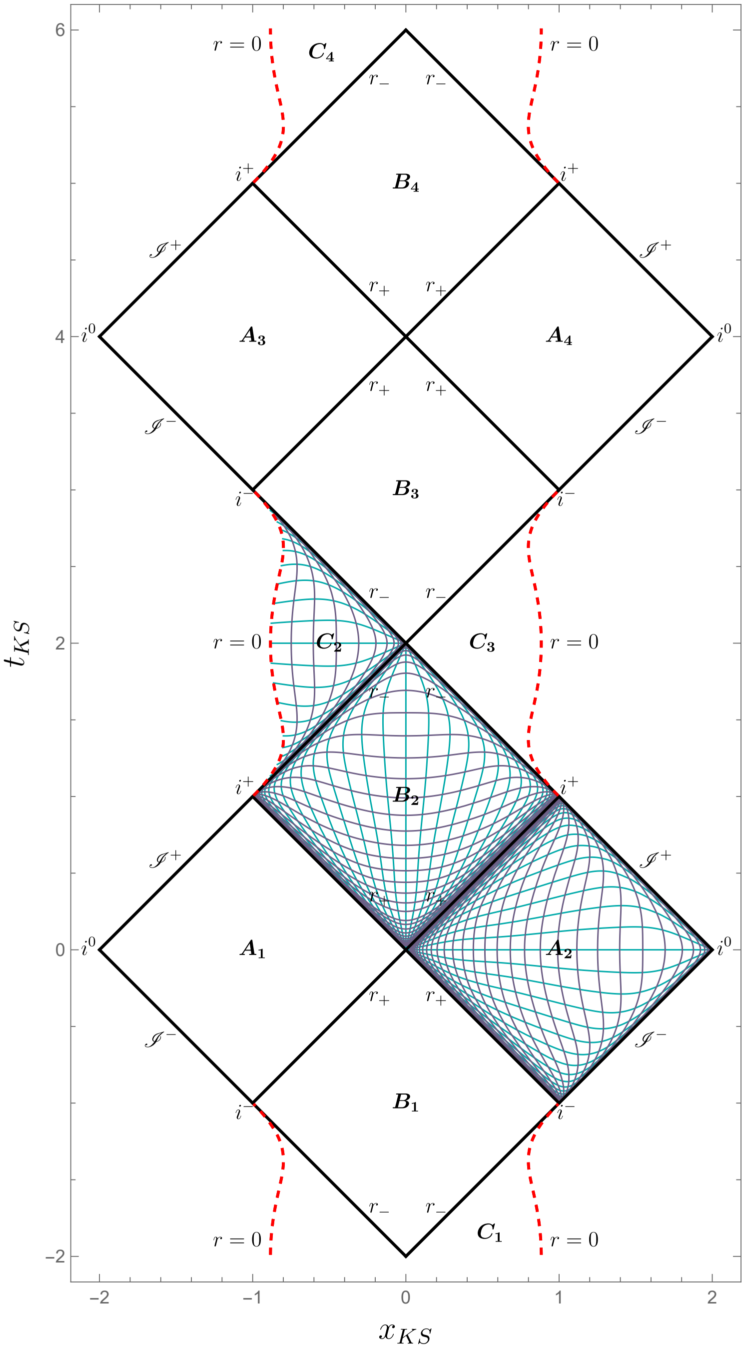

Figure 2.4: Kruskal-Szekeres spacetime diagram of the maximal extension of non-extremal Reissner-Nordström spacetime with $m = 1$ and $q = 0.98$ (Planck units). In light blue curves of constant t and in violet curves of constant r.

shape of the curvature singularity at $r = 0$, is apparently an inherent property of a coordinate chart that interpolates between the behavior of the inner and outer Kruskal-Szekeres coordinates and it does not (significantly) depend on the choice of smooth transition functions $g_{\uparrow\downarrow}(X)$. The same behavior is indeed found also in the C^1 global Kruskal-Szekeres coordinate chart derived in Hamilton [24], where no transition functions are used. This behavior is particularly pronounced for values of m and q far from the extremal case, with curves of constant t and r being squeezed towards the boundary of their block. This phenomenon however seems to also be a general problem of any smooth and global Carter-Penrose coordinate charts for strongly spherically symmetric spacetimes. Schindler and Aguirre [13] in fact recently defined an algorithm to construct global Carter-Penrose coordinate charts of any given regularity for strongly spherically symmetric spacetimes (with simple zeroes). Since smooth charts displayed the same phenomenon discussed above, they gave up the smoothness requirement in their construction of Carter-Penrose diagrams in favor of a better appearance of the diagram.

As a side note, a coordinate chart equivalent to the one defined in eqs. (2.34) and (2.35) can also be obtained with the more compact change of coordinates

$$\begin{aligned} u(u_{\mathrm{KS}}) = -\sum_{n\in\mathbb{Z}}\Big[&B(u_{\mathrm{KS}}, 2n)\frac{\log|u_{\mathrm{KS}} - 2n|}{\kappa_+} \\ &+ B(u_{\mathrm{KS}}, 2n+1)\frac{\log|u_{\mathrm{KS}} - (2n+1)|}{\kappa_-}\Big]\,, \end{aligned} \tag{2.38}$$

$$\begin{aligned} v(v_{\mathrm{KS}}) = \sum_{n\in\mathbb{Z}}\Big[&B(v_{\mathrm{KS}}, 2n)\frac{\log|v_{\mathrm{KS}} - 2n|}{\kappa_+} \\ &+ B(v_{\mathrm{KS}}, 2n+1)\frac{\log|v_{\mathrm{KS}} - (2n+1)|}{\kappa_-}\Big]\,, \end{aligned} \tag{2.39}$$

where $B(X, a)$ is the bump function

$$B(X,a) = \begin{cases} \exp\left(-\frac{1}{1-(X-a)^2}\right) & a-1 < X < a+1\,, \\ 0 & \text{otherwise}\,. \end{cases}$$

2.5 Extremal case

The exact same construction can be carried out also in the extremal case $m^2 = q^2$, resulting in a global Kruskal-Szekeres coordinate chart covering the entire maximal extension of the extremal Reissner-Nordström spacetime.

The extremal Reissner-Nordström metric in the coordinate system (t, r, θ, ϕ) still reads

$$\mathrm{d}s^2 = -h(r)\,\mathrm{d}t^2 + h^{-1}(r)\,\mathrm{d}r^2 + r^2\,\mathrm{d}\Omega^2\,, \tag{2.40}$$

but now

$$h(r) = \left(1 - \frac{m}{r}\right)^2 . \tag{2.41}$$

This function has only a unique (double) zero which results in a Killing horizon at $r = m$. The coordinate chart (t, r, θ, ϕ) can be used to separately cover all spacetime regions such that $0 < r < m$ or $m < r < +\infty$. In the spacetime regions where $m < r < +\infty$ the coordinates t and r are respectively timelike and spacelike and the metric is static, since the Killing vector field ∂_t is timelike. In the spacetime regions where $0 < r < m$ t is spacelike and r is timelike. Furthermore, since ∂_t becomes spacelike, these spacetime regions are homogeneous but neither static nor stationary. The metric has a coordinate singularity in $r = m$ and a curvature singularity in $r = 0$.

The maximal extension of this spacetime is shown in fig. 2.5 using the global Kruskal-Szekeres coordinate chart that will be defined shortly. From the diagram, it can be seen that even if the spacetime possesses only one horizon at $r = m$, similarly to what happens in Schwarzschild spacetime, the curvature singularity at $r = 0$ is still timelike and an observer that falls inside the horizon can exit the black hole interior into a second asymptotically flat exterior region in the future of the first one. In fact, there is once again an infinite tower of asymptotically flat exterior regions connected to each other by black hole interiors.

The tortoise coordinate r_* satisfying $\mathrm{d}r_* = \mathrm{d}r/h(r)$ is now given by

$$r_* = r + 2m \log\left|\frac{r}{m} - 1\right| - \frac{m}{r/m - 1} + C'\,, \tag{2.42}$$

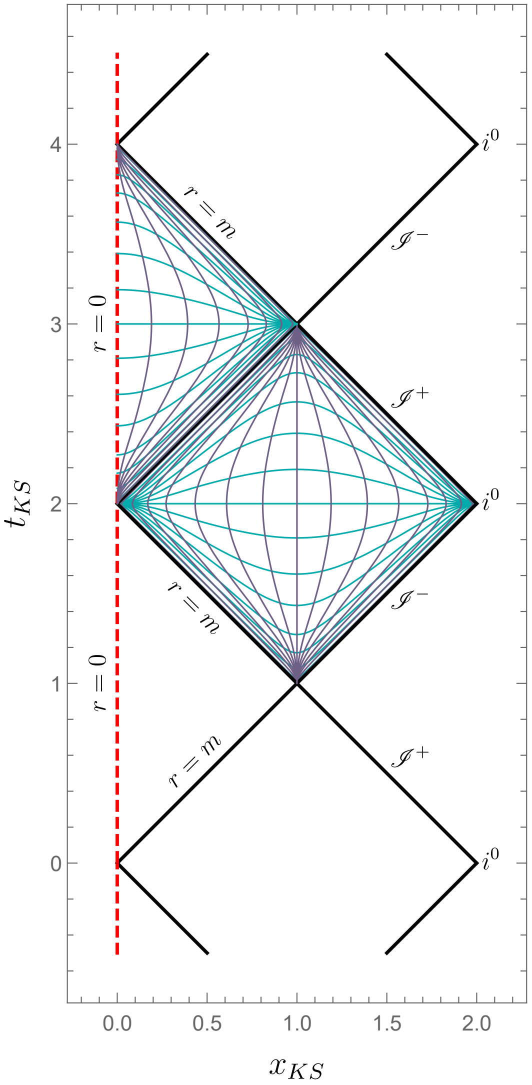

Figure 2.5: Kruskal-Szekeres spacetime diagram of the maximal extension of extremal Reissner-Nordström spacetime with $m = 1$ (Planck units). In light blue curves of constant t and in violet curves of constant r.

where C' is a constant of integration. Retarded and advanced time null coordinates u and v are defined as in eq. (2.5). Ingoing (v, r, θ, ϕ) and outgoing (u, r, θ, ϕ) Eddington-Finkelstein coordinates and double-null coordinates (u, v, θ, ϕ) can then be used to cover different regions of spacetime as usual.

The analysis of the behavior of null geodesics in Eddington-Finkelstein coordinates for the extremal geometry closely follows the analysis of the non-extremal case discussed in section 2.3. Outgoing radial null geodesics in ingoing Eddington-Finkelstein coordinates satisfy

$$\dot{v} = \frac{2E}{h(r)}\,, \qquad \dot{r} = E\,, \tag{2.43}$$

where $h(r)$ is now given by eq. (2.41). Focusing on one of the asymptotically flat exterior regions, and taking $r_0 = 0$ and $E = 1$ (future-oriented geodesics have $E > 0$) for simplicity, outgoing radial null geodesics are given by

$$r(\lambda) = \lambda\,, \qquad \lambda \in (m, \infty)\,, \tag{2.44}$$

$$v(\lambda) = 2\lambda + 4m \log\left|\frac{\lambda}{m} - 1\right| - \frac{2m}{\frac{\lambda}{m} - 1} + K\,, \tag{2.45}$$

where K is a constant identifying different geodesics. These curves start at the past horizon of the exterior region, that is $r \to m$ and $v \to -\infty$ for $\lambda \to m^+$, cross diagonally this exterior region and end at future null infinity $\mathscr{I}^+$.

Similarly, future-oriented ingoing radial null geodesics ($E = 1$ and $r_0 = 0$) in outgoing Eddington-Finkelstein coordinates are given by

$$r(\sigma) = -\sigma\,, \qquad \sigma \in (-\infty, -m)\,, \tag{2.46}$$

$$u(\sigma) = 2\sigma - 4m \log\left|\frac{\sigma}{m} + 1\right| - \frac{2m}{\frac{\sigma}{m} + 1} + K'\,, \tag{2.47}$$

where K' is a constant identifying different geodesics. These curves start at past null infinity $\mathscr{I}^-$, diagonally cross the exterior region, and end at the future horizon, that is $r \to m$ and $u \to +\infty$ for $\sigma \to (-m)^-$.

Naturally, these outgoing and ingoing null geodesics do not abruptly start or end at the past or future horizon, but the null coordinates u and v are not able to follow them past the horizons. However, the leading behavior of eqs. (2.45) and (2.47) near the horizons once again suggests a natural change of coordinates to extend u and v beyond the horizons.

Starting from the leading behavior of eqs. (2.45) and (2.47) near the horizons, and skipping all the intermediate steps detailed in section 2.4 for the non-extremal case, a global Kruskal-Szekeres coordinate chart for the maximal extension of the extremal Reissner-Nordström spacetime can be defined by the following transformation:

$$\frac{u(u_{\mathrm{KS}})}{2m} = \begin{cases} \vdots & \\ -\dfrac{g_{\downarrow}(u_{\mathrm{KS}}, n-1, n)}{u_{\mathrm{KS}} - (n-1)} - \dfrac{g_{\uparrow}(u_{\mathrm{KS}}, n-1, n)}{u_{\mathrm{KS}} - n} & n-1 < u_{\mathrm{KS}} < n\,, \\ -\dfrac{g_{\downarrow}(u_{\mathrm{KS}}, n, n+1)}{u_{\mathrm{KS}} - n} - \dfrac{g_{\uparrow}(u_{\mathrm{KS}}, n, n+1)}{u_{\mathrm{KS}} - (n+1)} & n < u_{\mathrm{KS}} < n+1\,, \\ \vdots & \end{cases} \tag{2.48}$$

$$\frac{v(v_{\mathrm{KS}})}{2m} = \begin{cases} \vdots & \\ -\dfrac{g_{\downarrow}(v_{\mathrm{KS}}, n-1, n)}{v_{\mathrm{KS}} - (n-1)} - \dfrac{g_{\uparrow}(v_{\mathrm{KS}}, n-1, n)}{v_{\mathrm{KS}} - n} & n-1 < v_{\mathrm{KS}} < n\,, \\ -\dfrac{g_{\downarrow}(v_{\mathrm{KS}}, n, n+1)}{v_{\mathrm{KS}} - n} - \dfrac{g_{\uparrow}(v_{\mathrm{KS}}, n, n+1)}{v_{\mathrm{KS}} - (n+1)} & n < v_{\mathrm{KS}} < n+1\,, \\ \vdots & \end{cases} \tag{2.49}$$

with $n \in \mathbb{Z}$. The position of the horizons in the $(u_{\mathrm{KS}}, v_{\mathrm{KS}})$ coordinates is arbitrary. I made the choice $u_{\mathrm{KS}} = n$ and $v_{\mathrm{KS}} = n$ for $n \in \mathbb{Z}$.

Defining the function $f(X)$ in such a way that $u'(u_{\mathrm{KS}}) = f(u_{\mathrm{KS}})$ and $v'(v_{\mathrm{KS}}) = f(v_{\mathrm{KS}})$, the extremal Reissner-Nordström metric in these global Kruskal-Szekeres coordinates $(u_{\mathrm{KS}}, v_{\mathrm{KS}}, \theta, \phi)$ reads

$$\mathrm{d}s^2 = -h(r) f(u_{\mathrm{KS}}) f(v_{\mathrm{KS}})\, \mathrm{d}u_{\mathrm{KS}}\, \mathrm{d}v_{\mathrm{KS}} + r^2\, \mathrm{d}\Omega^2\,, \tag{2.50}$$

where $r = r(u_{\text{KS}}, v_{\text{KS}})$ is implicitly defined by eqs. (2.8), (2.42), (2.48) and (2.49). These equations can then be used to study the regularity of both the function $r(u_{\text{KS}}, v_{\text{KS}})$ itself and of the metric tensor near the horizons. The analysis is carried out exactly as it is carried out for the non-extremal case, and it shows that the metric tensor in eq. (2.50) is well behaved on all spacetime horizons and that the Kruskal-Szekeres double-null coordinates $(u_{\text{KS}}, v_{\text{KS}}, \theta, \phi)$ provide a smooth and global coordinate chart for the maximal extension of extremal Reissner-Nordström spacetime.

The transformation in eqs. (2.48) and (2.49) separately gives a well-defined diffeomorphism between $(u_{\text{KS}}, v_{\text{KS}}, \theta, \phi)$ and (u, v, θ, ϕ) in each spacetime block, even if an analytical expression for the inverse transformation cannot be given. Once again, this is ensured by the strict monotonicity of $u(u_{\text{KS}})$ and $v(v_{\text{KS}})$ in each spacetime block and by the inverse function theorem. Being the double-null coordinates (u, v, θ, ϕ) singular on the horizons, also the transformation in eqs. (2.48) and (2.49) is ill defined there.

Global Kruskal-Szekeres spatial x_{KS} and temporal t_{KS} coordinates can be defined as in eq. (2.37). The Kruskal-Szekeres spacetime diagram of the maximal extension of extremal Reissner-Nordström spacetime is shown in fig. 2.5. This diagram is actually a genuine Carter-Penrose diagram for the spacetime, as it was the case also for the non-extremal case.

Chapter 3

The black-to-white hole spacetime

A version of this chapter has been published in Physical Review D as

M. Han, C. Rovelli and F. Soltani. “Geometry of the black-to-white hole transition within a single asymptotic region”. *Phys. Rev. D* **107** (2023), 064011. DOI: `10.1103/PhysRevD.107.064011.` Copyright © 2023 by American Physical Society. All rights reserved.

F. Fazzini, C. Rovelli and F. Soltani. “Painlevé-Gullstrand coordinates discontinuity in the quantum Oppenheimer-Snyder model”. *Phys. Rev. D* **108** (2023), 044009. DOI: `10.1103/PhysRevD.108.044009.` Copyright © 2023 by American Physical Society. All rights reserved.

3.1 Introduction

The starting point of this chapter is the physical picture of a black hole spacetime discussed in section 1.2.5. The classical theory is able to describe the local exterior geometry of a black hole extremely well. However, this description breaks down completely into three physically separate regions (as qualitatively shown in fig. 3.1):

Region $\mathscr{A}$: The subregion of the vacuum region in the interior of the black hole where the curvature becomes Planckian;

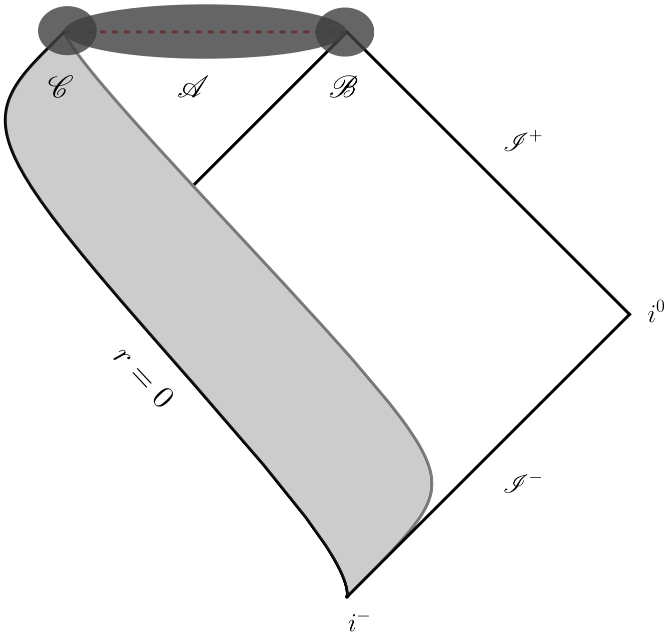

Figure 3.1: The three quantum regions of a black hole spacetime.

Region $\mathscr{B}$: The spacetime region surrounding the black hole horizon when it reaches Planckian size at the end of the evaporation process;

Region $\mathscr{C}$: The subregion of the interior of the star where both star density and curvature become Planckian.

In these regions, quantum gravitational effects cannot be neglected and the results of the classical theory cannot be trusted.

Loop quantum gravity inspired investigations [96–119] consistently and coherently point towards a scenario where the Einstein field equations are briefly violated in these three regions, either by correction terms depending on the value of the curvature or by quantum tunneling effects, and spacetime smoothly continues past them. A natural and concrete implementation of this scenario is the black-to-white hole transition [43, 120–124], where the internal geometry of the black hole undergoes a smooth transition from trapped to anti-trapped (possibly through an intermediate non-trapped region) and the horizon tunnels from marginally trapped to marginally anti-trapped as well. In this scenario, the black hole evolves into a white-hole "remnant" living in the future of the parent black hole, in its same asymptotic region and location. The aim of this chapter is to construct a concrete effective spacetime metric to describe this phenomenon.

The starting point of the construction is the Oppenheimer-Snyder model introduced in section 1.2.2. In order to obtain a concrete spacetime metric whose properties can be investigated, dissipative phenomena such as Hawking evaporation or Perez dissipation into Planckian degrees of freedom [125] are not taken into account. The assumption made is that dissipative phenomena can be disregarded in a first approximation, as it can be done for a basketball bouncing on the floor, and consequently that the "bounce" of the geometry can be described in a first approximation in terms of a few "large-scale" degrees of freedom. Rotational degrees of freedom are neglected as well. However, the causal structure of the spacetime constructed in this chapter will be quite similar to the causal structure of *Kerr spacetime*, suggesting that rotation might not significantly alter the picture.

Although the evaporation process of the black hole will be completely neglected in the construction of the metric, it will be an important factor in the physical interpretation of the model. It will in fact be argued that the inclusion of the evaporation process should not alter the qualitative picture given by the spacetime constructed in this chapter. A spacetime model taking into account Hawking radiation in the black-to-white hole transition scenario has been studied in Martin-Dussaud and Rovelli [39].

In regions $\mathscr{A}$ and $\mathscr{C}$ quantum effects are studied only as local violations of the Einstein field equations, and not with a full quantum analysis. This is possible thanks to the similarity of the interior geometry of the collapsing star in the Oppenheimer-Snyder model with the geometry of a cosmological scenario. In fact, since the loop quantization of this cosmological scenario leads to a quantum-corrected Friedmann equation [126, 127] for the scale factor, the same will be true also in the interior of the star. The quantum-corrected Friedmann equation predicts a "bounce" of the star at the end of its collapse, followed by an expansion analogous to the one happening in a star emerging from a white hole singularity. The geometry of the interior of the black hole outside the star can then be uniquely determined [128, 129] by requiring the junction conditions to be satisfied on the boundary of the star, as in the classical Oppenheimer-Snyder model. The resulting geometry turns out to be similar to the interior geometry of a Reissner–Nordström spacetime.

The quantum physics of region $\mathscr{B}$ is instead modeled as a non-perturbative quantum tunneling event that briefly and locally violates the Einstein field equations around the horizon and that allows the bounce of the interior geometry to happen in a unique asymptotically flat exterior region. The (surprising) compatibility of this scenario with the validity of the Einstein field equations outside the quantum region was first pointed out in Haggard and Rovelli [43]. Crucially, it will be shown that the horizon tunneling region (region $\mathscr{B}$) can be filled with an (effective) smooth Lorentzian metric. This geometry unravels the possible global horizon structure of the black-to-white hole scenario: There are neither event nor global Killing horizons; there are only apparent horizons, and these keep the trapped and anti-trapped regions disconnected. The metric in this region only provides proof of existence for a geometry with these features. As with any trajectory in a quantum tunneling phenomenon, its direct physical interpretation is not straightforward.

The chapter is structured as follows. Sections 3.2 and 3.3 deal with the physics of regions $\mathscr{C}$ and $\mathscr{A}$. The physics of region $\mathscr{B}$ is discussed in section 3.4. The physical meaning and the large-scale geometry of the black-to-white spacetime are analyzed in section 3.5. A global coordinate chart for the spacetime is then given in section 3.6. Section 3.7 deals with the construction of a Lorentzian effective metric for the $\mathscr{B}$ region and section 3.8 provides a qualitative analysis of the horizon structure of the spacetime.

3.2 Region $\mathscr{C}$: Interior of the star

As already seen in section 1.2.2, the Oppenheimer-Snyder model describes the collapsing star as a spherical ball of uncharged dust of uniform density. In

Planck units ($c = \hbar = G = 1$), and assuming the star's boundary to start at rest at past infinity, the metric describing this object in $(t, \tilde{r}, \theta, \phi)$ coordinates is given by

$$\mathrm{d}s^2 = -\,\mathrm{d}t^2 + a^2(t)\left(\,\mathrm{d}\tilde{r}^2 + \tilde{r}^2\,\mathrm{d}\Omega^2\,\right), \tag{3.1}$$

where t and $\tilde{r}$ are comoving coordinates with respect to the geodesics of constant $\tilde{r}$, θ, and ϕ. The coordinate interval of the time coordinate t depends on the regularity of the scale factor. The coordinate interval of $\tilde{r}$ is given by $0 < \tilde{r} \leq \tilde{r}_\mathrm{b}$, where $\tilde{r}_\mathrm{b} = \text{const.}$ is the wordline of the boundary of the star seen from the interior.

The Einstein field equations for this metric reduce to the Friedmann equation for the scale factor $a(t)$ in eq. (1.62). The solution to this equation describes a star of physical radius $r_\mathrm{b}(t) = a(t)\tilde{r}_\mathrm{b}$ that starts to collapse from rest at $r_\mathrm{b} \to +\infty$ for $t \to -\infty$ and then keep collapsing until it reaches a singular point of vanishing physical radius at $t = t_0$.

A thorough investigation of the (loop) quantum theory of such a geometry [126, 130] shows that a description of this scenario in terms of an effective spacetime metric taking into account first-order quantum corrections is possible. The line element in eq. (3.1) stays the same, but the Friedmann equation for $a(t)$ is modified to

$$\frac{\dot{a}^2}{a^2} = \frac{8\pi}{3}\rho\left(1 - \frac{\rho}{\rho_c}\right), \tag{3.2}$$

where the *critical density*[1] ρ_c is a constant parameter of Planckian value whose exact expression will not be relevant in the following and $\rho = 3m/4\pi r_\mathrm{b}^3$. The quantum-corrected Friedmann equation can be integrated to give

$$a(t) = \left(\frac{9m(t_0 - t)^2 + Am}{2r_\mathrm{b}^3}\right)^{1/3}, \tag{3.3}$$

where $A = 3/(2\pi\rho_c)$ is a parameter of Planckian value with the dimensions of a squared mass. Equation (3.3) gives the quantum-corrected version of the classical equation eq. (1.66). Their comparison is shown in the plot in fig. 3.2.

---

[1] $\rho_c = \sqrt{3}c^2/(32\pi^2\gamma^3\hbar G^2)$, γ being the Barbero-Immirzi parameter.

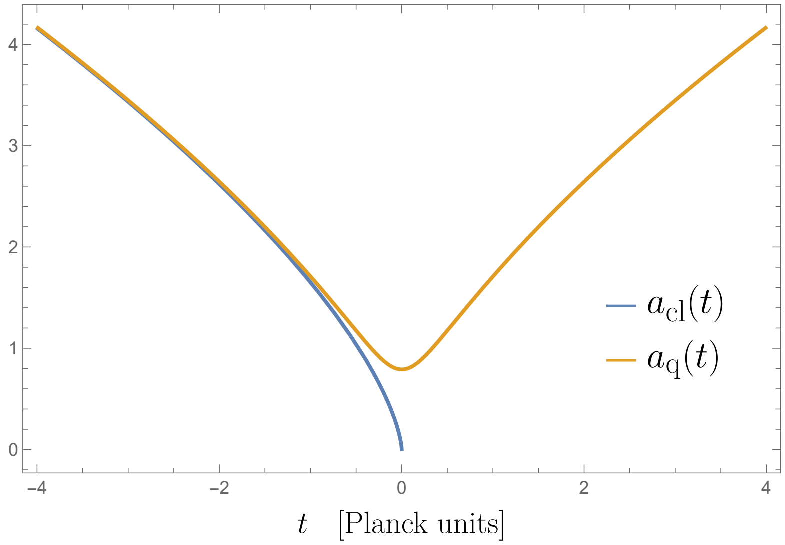

Figure 3.2: Plot of the classical scale factor $a_{\mathrm{cl}}(t)$ (blue) and the quantum-corrected scale factor $a_{\mathrm{q}}(t)$ (orange) with $m = 1$, $t_0 = 0$ and $A = .99$.

Importantly, the quantum-corrected scale factor never vanishes, meaning that the physical radius r_{b} of the star never collapses to zero, but it rather reaches its minimum size

$$r_M = a(0)\tilde{r}_{\mathrm{b}} = (Am/2)^{1/3} \tag{3.4}$$

at $t = t_0$, before "bouncing" and starting to increase. This is the characteristic bounce of *loop quantum cosmology* [126, 130]. The interior metric in eq. (3.1) is thus well defined in the whole interval $-\infty < t < +\infty$.

3.3 Region $\mathscr{A}$: Exterior of the star

Classically, the geometry in the exterior of the star is given by Schwarzschild geometry. In the context of the Oppenheimer-Snyder model, this geometry can be uniquely characterized as the geometry that: i) is spherically symmetric, ii) has a Killing vector field in addition to those related to the spherical symmetry, iii) satisfies the junction conditions on the boundary of the star. It can be shown [128, 129] that requiring the exterior geometry to satisfy the same three conditions, with the matching in iii) performed with the quantum-corrected interior geometry constructed in the last section, uniquely fixes the exterior metric to

$$\mathrm{d}s^2 = -F(r)\,\mathrm{d}t_S^2 + F^{-1}(r)\,\mathrm{d}r^2 + r^2\,\mathrm{d}\Omega^2\,, \tag{3.5}$$

where

$$F(r) = 1 - \frac{2m}{r} + \frac{Am^2}{r^4}\,. \tag{3.6}$$

This is the metric of a strongly spherically symmetric spacetime with defining function $f(r) = F(r)$ expressed in the standard spherical coordinate system (t_S, r, θ, ϕ). The time coordinate has been labeled t_S to avoid confusion with the time coordinate t of the interior of the star. Since however the distinction between the two should be clear from the context, in the following I will use t to denote both of them in order to avoid an unnecessary complex notation.

The spacetime defined by eqs. (3.5) and (3.6) provides a first-order quantum correction to Schwarzschild geometry in the context of the Oppenheimer-Snyder model. It depends on two parameters: the total mass m of the star and the constant $A \sim m_{Pl}^2$ characterizing the quantum correction to the Friedmann equation. If $m \gg m_{\mathrm{P}}$ and r is of order m or larger, where the classical theory is still expected to be reliable, the last term in eq. (3.6) gives a negligible contribution and the spacetime in eq. (3.5) is basically Schwarzschild spacetime.

Interestingly enough, the same exterior metric can be derived independently from the interior of the star by studying loop quantum gravity corrections in spherically symmetric spacetimes [131, 132]. This is a nice consistency check of the formalism.

3.3.1 Zeroes of $F(r)$

As the analysis of strongly spherically symmetric spacetimes in section 1.1.2 shows, finding the zeroes of the defining function $f(r)$ is a very important step in the description of these spacetimes. It is then necessary to find the zeroes of the function

$$F(r) = 1 - \frac{2m}{r} + \frac{Am^2}{r^4} \tag{3.7}$$

with A being a constant with dimensions of a squared mass and satisfying $A \ll m^2$. Finding the zeroes of $F(r)$ is equivalent to finding the roots of the fourth-degree equation

$$r^4 - 2mr^3 + Am^2 = 0\,. \tag{3.8}$$

Although the exact solutions to this problem are known, their expression is too complicated to be of any help in the investigation of the spacetime. Instead, the solutions to this equation will be studied perturbatively in the small parameter A. The absence of a closed formula for the zeroes of $F(r)$ will not affect in any way the analysis of spacetime.

To rigorously treat eq. (3.8) as a perturbation problem in a small dimensionless parameter, let $x = r/m$, such that the equation to solve becomes

$$x^4 - 2x^3 + \varepsilon = 0\,, \tag{3.9}$$

where $\varepsilon := A/m^2 \ll 1$. The unperturbed equation

$$x^4 - 2x^3 = 0 \tag{3.10}$$

has the four solutions

$$x_{1,2,3} = 0 \qquad x_4 = 2\,. \tag{3.11}$$

The idea is then to perturbatively search for solutions of eq. (3.9) of the form

$$x_i = \sum_{n=0}^{\infty} a_{i,n}\varepsilon^n\,, \tag{3.12}$$

where $i = 1,2,3,4$, $a_{4,0} = 2$, and $a_{j,0} = 0$ for $j = 1,2,3$. The coefficients $a_{i,n}$ can be determined by solving eq. (3.9) order by order.

Let us start with the ε order for x_4. Inserting

$$x_4 = 2 + a_{4,1}\varepsilon + O(\varepsilon^2) \tag{3.13}$$

in eq. (3.9) we find

$$\big(2 + a_{4,1}\varepsilon + O(\varepsilon^2)\big)^4 - 2\big(2 + a_{4,1}\varepsilon + O(\varepsilon^2)\big)^3 + \varepsilon = 0\,. \tag{3.14}$$

Solving to order ε we obtain $a_{4,1} = -1/8$. This means that

$$x_4 = 2 - \frac{\varepsilon}{8} + O(\varepsilon^2)\,. \tag{3.15}$$

If we try to do the same for

$$x_j = a_{j,1} + O(\varepsilon^2), \tag{3.16}$$

where $j = 1, 2, 3$, we get

$$\big(a_{j,1}\varepsilon + O(\varepsilon^2)\big)^4 - 2\big(a_{j,1}\varepsilon + O(\varepsilon^2)\big)^3 + \varepsilon = 0\,. \tag{3.17}$$

This equation is clearly not consistent, which means that the ansatz in eq. (3.12) is not consistent. It simply means that $x_j \sim \varepsilon$ ($j = 1, 2, 3$) for $\varepsilon \ll 1$ is not true. In order to find the right scaling we can study the *dominate balance* of eq. (3.9) when $\varepsilon \ll 1$ (see Bender and Orszag [133] for further details):

- If $x^4 \sim x^3$, and thus
$$\varepsilon \ll x^4, x^3\,, \tag{3.18}$$
we find one solution such that $x \sim 1$. Equation (3.18) gives $\varepsilon \ll 1$, which is consistent. This solution is the solution x_4 we already found.

- If $x^4 \sim \varepsilon$, and thus
$$x^3 \ll x^4, \varepsilon\,, \tag{3.19}$$
we find three solutions such that $x \sim \varepsilon^{1/4}$. Equation (3.19) gives $\varepsilon^{3/4} \ll \varepsilon$, which is not consistent.

- If $x^3 \sim \varepsilon$, and thus
$$x^4 \ll x^3, \varepsilon\,, \tag{3.20}$$
we find three solutions such that $x \sim \varepsilon^{1/3}$. Equation (3.20) gives $\varepsilon^{4/3} \ll \varepsilon$,

which is consistent. Hence, the remaining solutions x_j ($j = 1, 2, 3$) behave as $x_j \sim \varepsilon^{1/3}$ for $\varepsilon \to 0$.

The new ansatz for the solutions x_j ($j = 1, 2, 3$) is then

$$x_j = \sum_{n=1}^{\infty} b_{j,n} (\varepsilon^{1/3})^n \,. \tag{3.21}$$

Inserting

$$x_j = b_{j,1}\varepsilon^{1/3} + O(\varepsilon^{2/3}) \tag{3.22}$$

in eq. (3.9) we find

$$\big(b_{j,1}\varepsilon^{1/3} + O(\varepsilon^{2/3})\big)^4 - 2\big(b_{j,1}\varepsilon^{1/3} + O(\varepsilon^{2/3})\big)^3 + \varepsilon = 0. \tag{3.23}$$

Keeping only the order ε we get $b_{j,1}^3 = 1/2$. The three solutions are thus

$$b_{3,1} = \frac{1}{2^{1/3}} \quad \text{and} \quad b_{(1,2),1} = \frac{1}{2^{1/3}} e^{\pm 2\pi i/3} \,. \tag{3.24}$$

All the subsequent orders of the solutions can be found in this way.

The roots of eq. (3.9) to their second non-vanishing order in ε are

$$\begin{aligned} x_{1,2} &= \left(\frac{\varepsilon}{2}\right)^{1/3} e^{\pm 2\pi i/3} + \frac{1}{6}\left(\frac{\varepsilon}{2}\right)^{2/3} e^{\pm 4\pi i/3} + O(\varepsilon) \,, \\ x_3 &= \left(\frac{\varepsilon}{2}\right)^{1/3} + \frac{1}{6}\left(\frac{\varepsilon}{2}\right)^{2/3} + O(\varepsilon) \,, \\ x_4 &= 2 - \frac{\varepsilon}{8} + O(\varepsilon^2) \,. \end{aligned} \tag{3.25}$$

Going back to the original variable r, the solutions to eq. (3.8) to their second non-vanishing order in A are

$$\begin{aligned} r_{1,2} &= \left(\frac{Am}{2}\right)^{1/3} e^{\pm 2\pi i/3} + \frac{1}{6}\left(\frac{A}{2\sqrt{m}}\right)^{2/3} e^{\pm 4\pi i/3} + O(A/m)\,, \\ r_- = r_3 &= \left(\frac{Am}{2}\right)^{1/3} + \frac{1}{6}\left(\frac{A}{2\sqrt{m}}\right)^{2/3} + O(A/m)\,, \\ r_+ = r_4 &= \; 2m - \frac{A}{8m} + O(A^2/m^3)\,. \end{aligned} \tag{3.26}$$

3.3.2 The tortoise coordinate r_*

Another important step for the investigation of the causal structure of strongly spherically symmetric spacetimes is the definition of the tortoise function r_* satisfying $\mathrm{d}r_* = \mathrm{d}r/F(r)$. So, let me get it out of the way.

First of all, consider again the fourth-degree equation

$$r^4 - 2mr^3 + Am^2 = 0\,. \tag{3.27}$$

The analysis in the last subsection tells us that this equation has two real solutions $r_\pm$ and two complex conjugate solutions $r_{1,2}$. This means that the polynomial $r^4 - 2mr^3 + Am^2$ can be rewritten as

$$r^4 - 2mr^3 + Am^2 = (r - r_+)(r - r_-)(r^2 + ar + b)\,, \tag{3.28}$$

where $r^2+ar+b = (r-r_1)(r-r_2)$ is a positive-definite second-degree polynomial. The values of a and b can be easily computed by expanding the polynomial in the right-hand side of eq. (3.28) and then equating it order-by-order to the left-hand side. This gives

$$a = (r_+ + r_-) - 2m \tag{3.29}$$

and

$$b = \frac{Am^2}{r_+ r_-}\,. \tag{3.30}$$

The tortoise coordinate $r_*(r)$ is then given by

$$\begin{aligned}
r_*(r) &= \int \frac{\mathrm{d}r}{1 - 2m/r + Am^2/r^4} = \int \frac{r^4 \ \mathrm{d}r}{r^4 - 2mr^3 + Am^2} \\
&= \int \mathrm{d}r + \int \frac{2mr^3 - Am^2}{r^4 - 2mr^3 + Am^2} \,\mathrm{d}r \\
&= r + \int \frac{2mr^3 - Am^2}{(r - r_+)(r - r_-)(r^2 + ar + b)} \,\mathrm{d}r \,.
\end{aligned} \tag{3.31}$$

Using partial fraction decomposition we look for an expansion of the form

$$\frac{2mr^3 - Am^2}{(r - r_+)(r - r_-)(r^2 + ar + b)} = \frac{c_+}{r - r_+} + \frac{c_-}{r - r_-} + \frac{c_1 r + c_2}{r^2 + ar + b} \,, \tag{3.32}$$

where c_+, c_-, and $c_{1,2}$ are constants whose value need to be determined. By rewriting the right-hand side of this expression using a common denominator and then equating order-by-order the polynomials in the numerator of respectively left and right-hand side we find

$$c_+ = \frac{2mr_+^3 - Am^2}{(r_+ - r_-)\,(r_+^2 + ar_+ + b)} = \frac{r_+^4}{(r_+ - r_-)\,(r_+^2 + ar_+ + b)} = \frac{1}{F'(r_+)} \,, \tag{3.33}$$

$$c_- = \frac{2mr_-^3 - Am^2}{(r_- - r_+)\,(r_-^2 + ar_- + b)} = \frac{r_-^4}{(r_- - r_+)\,(r_-^2 + ar_- + b)} = \frac{1}{F'(r_-)} \,, \tag{3.34}$$

$$\begin{aligned}
c_1 = &- \frac{-2a^2 m r_- r_+ + aAm^2 - 2abmr_- - 2abmr_+ + Am^2 r_- + Am^2 r_+}{(r_+^2 + ar_+ + b)\,(r_-^2 + ar_- + b)} \\
&- \frac{2bmr_- r_+ - 2b^2 m}{(r_+^2 + ar_+ + b)\,(r_-^2 + ar_- + b)} \,,
\end{aligned} \tag{3.35}$$

$$\begin{aligned}
c_2 = &- \frac{a^2 Am^2 + aAm^2 r_- + aAm^2 r_+ - 2abmr_- r_+ - Abm^2 + Am^2 r_- r_+}{(r_+^2 + ar_+ + b)\,(r_-^2 + ar_- + b)} \\
&+ \frac{2b^2 mr_- + 2b^2 mr_+}{(r_+^2 + ar_+ + b)\,(r_-^2 + ar_- + b)} \,.
\end{aligned} \tag{3.36}$$

This leads to

$$\begin{aligned}
r_*(r) &= r + c_+ \int \frac{\mathrm{d}r}{r - r_+} + c_- \int \frac{\mathrm{d}r}{r - r_-} + c_1 \int \frac{r + c_1/c_2}{r^2 + ar + b}\,\mathrm{d}r \\
&= r + c_+ \log|r - r_+| + c_- \log|r - r_-| \\
&\quad + \frac{c_1}{2} \int \frac{(2r + a) + (2c_1/c_2 - a)}{r^2 + ar + b}\,\mathrm{d}r \\
&= r + c_+ \log|r - r_+| + c_- \log|r - r_-| \\
&\quad + \frac{c_1}{2} \log\bigl(r^2 + ar + b\bigr) + (2c_1/c_2 - a) \int \frac{\mathrm{d}r}{(r + a/2)^2 + (b - a^2/4)} \\
&= r + c_+ \log|r - r_+| + c_- \log|r - r_-| + \frac{c_1}{2} \log\bigl(r^2 + ar + b\bigr) \\
&\quad + \frac{(2c_1/c_2 - a)}{\sqrt{b - a^2/4}} \tan^{-1}\left(\frac{r + a/2}{\sqrt{b - a^2/4}}\right) + K\,.
\end{aligned} \tag{3.37}$$

3.3.3 Investigation of the causal structure of spacetime

It is finally time to investigate the causal structure of the exterior spacetime. The metric in spherical coordinates (t, r, θ, ϕ) reads

$$\mathrm{d}s^2 = -F(r)\,\mathrm{d}t^2 + F^{-1}(r)\,\mathrm{d}r^2 + r^2\,\mathrm{d}\Omega^2\,, \tag{3.38}$$

where

$$F(r) = 1 - \frac{2m}{r} + \frac{Am^2}{r^4}\,. \tag{3.39}$$

The analysis in section 3.3.1 shows that the defining function $F(r)$ has two real roots $r_\pm$. Spacetime has thus two different Killing horizons. For $m \gg m_\mathrm{P}$, that is $m^2 \gg A$,

$$r_+ = 2m + O(A/m) \tag{3.40}$$

is the outer horizon of the black hole and it is located in the classical region where quantum corrections are negligible, while

$$r_- = \sqrt[3]{Am/2} + O(A^{2/3}/m^{1/3}) \tag{3.41}$$

is an inner horizon and it is located inside the quantum region. A direct study of the metric in eqs. (3.38) and (3.39) shows that $r = r_{\pm}$ are also apparent horizons. The coordinate chart (t, r, θ, ϕ) can be used to separately cover all spacetime regions such that $0 < r < r_-$, $r_- < r < r_+$, or $r_+ < r < +\infty$. In the spacetime regions where $0 < r < r_-$ or $r_+ < r < +\infty$ the coordinates t and r are respectively timelike and spacelike and the metric is static, since the Killing vector field ∂_t is timelike. On the contrary, in the spacetime regions where $r_- < r < r_+$ t is spacelike and r is timelike. Furthermore, since ∂_t becomes spacelike, these spacetime regions are homogeneous but neither static nor stationary. The metric in eqs. (3.38) and (3.39) has coordinate singularities in $r = r_{\pm}$ and a timelike curvature singularity in $r = 0$.

The Carter-Penrose diagram of the maximal extension of the quantum-corrected Oppenheimer-Snyder model is shown in fig. 3.3. The diagram is drawn using the global Kruskal-Szekeres coordinate chart for strongly spherically symmetric spacetimes introduced in chapter 2. The spacetime blocks can be labeled in the following way:

- There are two asymptotically flat regions, a "lower" region L bounded by a lower outer horizon and an "upper" region U bounded by an upper outer horizon, where $r_+ < r < +\infty$.
- There are a trapped region T and an anti-trapped region A where $r_- < r < r_+$.
- There are two interior non-trapped regions; one inner region I where $r_b(\tau) < r < r_-$, $r_b(\tau)$ being the wordline of the star's boundary, and an interior region S bounded by the timelike curvature singularity at $r = 0$ where $0 < r < r_-$.

The bounce of the star takes place in the non-trapped interior region I. This is consistent with the analysis of matter collapse performed in Achour et al. [107], where it is shown that a bounce of the collapsing matter can take place only in a non-trapped region.

The coordinate chart (t, r, θ, ϕ) can separately cover each one of the spacetime regions L, T, I, S, A, and U, with the time coordinate t going to infinity

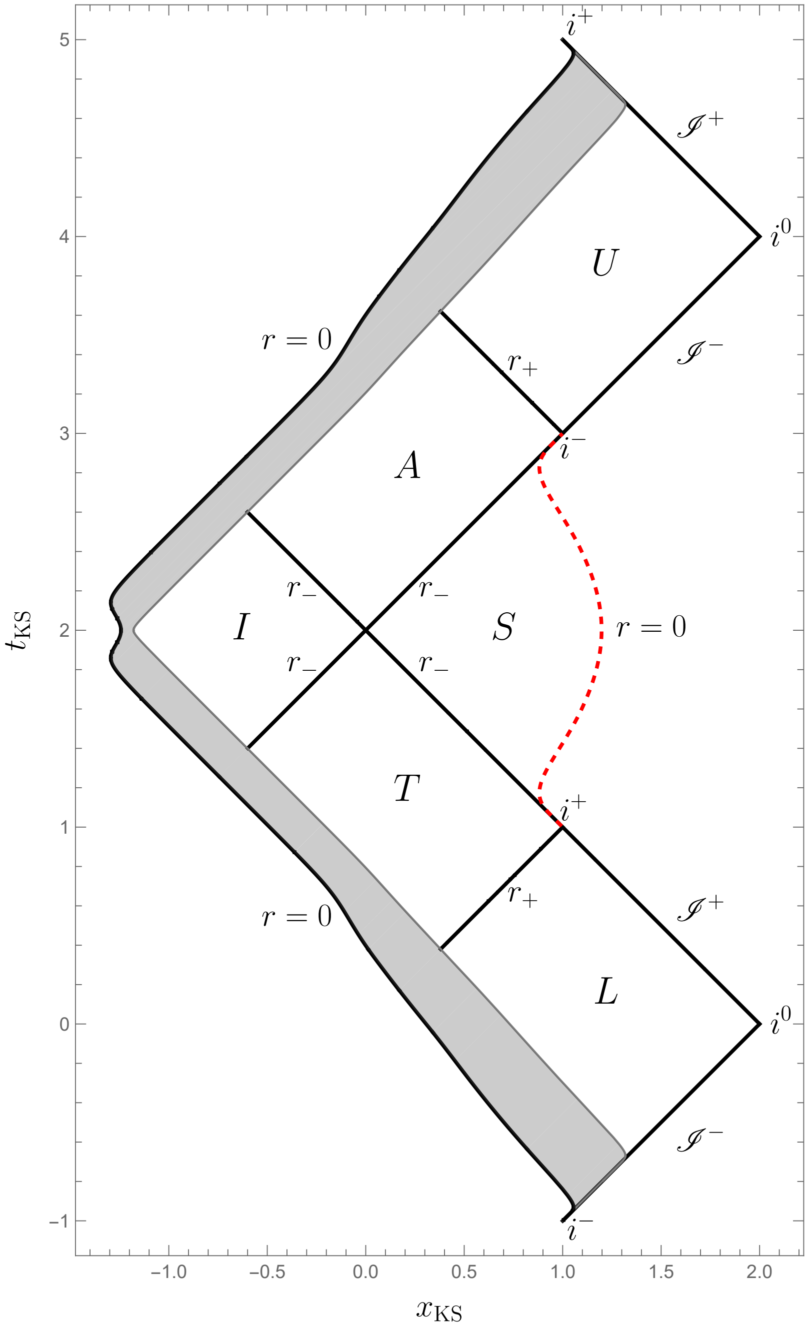

Figure 3.3: Carter-Penrose diagram of the quantum-corrected Oppenheimer-Snyder model with $m = 1$ and $A = 0.99$ (Planck units). The interior of the star is represented in gray.

on every horizon. Retarded and advanced time null coordinates u and v can be defined as

$$u = r_* - t, \tag{3.42}$$

$$v = r_* + t, \tag{3.43}$$

where the explicit expression of the tortoise coordinate $r_*(r)$ is given in eq. (3.37). Notice that the definition of the coordinate u in this chapter differs by a global sign with respect to the one used in the previous chapters. This convention greatly simplifies later formulas. The exterior metric in eq. (3.38) in ingoing Eddington-Finkelstein coordinates (v, r, θ, ϕ) reads

$$\mathrm{d}s^2 = -F(r)\,\mathrm{d}v^2 + 2\,\mathrm{d}v\,\mathrm{d}r + r^2\,\mathrm{d}\Omega^2. \tag{3.44}$$

The advanced time coordinate v is well behaved on all the horizons that are represented as 45° lines in the Carter-Penrose diagram, but it goes to infinity on the others. The ingoing Eddington-Finkelstein coordinate system is then able to simultaneously cover either regions L, T, I, or regions S, A, or region U. Analogously, the metric outgoing Eddington-Finkelstein coordinates (u, r, θ, ϕ) reads

$$\mathrm{d}s^2 = -F(r)\,\mathrm{d}u^2 + 2\,\mathrm{d}u\,\mathrm{d}r + r^2\,\mathrm{d}\Omega^2, \tag{3.45}$$

and the retarded time coordinate u is well behaved on all the horizons that are represented as −45° lines in the Carter-Penrose diagram, but it goes to infinity on the others. Outgoing Eddington-Finkelstein coordinates can be used to simultaneously cover either regions U, A, I, or regions S, T, or region L.

The metric in the double-null coordinate system (u, v, θ, ϕ) becomes

$$\mathrm{d}s^2 = F(r)\;\mathrm{d}u\;\mathrm{d}v + r^2\,\mathrm{d}\Omega^2\,, \tag{3.46}$$

where the function $r = r(u, v)$ is implicitly defined by

$$2r_*(r) = v + u. \tag{3.47}$$

One of the two null coordinates is ill-defined on each horizon, and this coordinate system does not improve the spacetime coverage of the coordinate system (t, r, θ, ϕ).

For the construction of the next section, it is convenient to choose $v = 0$ as the advanced time in which the star's boundary enters the lower outer horizon r_+ and $u = 0$ as the retarded time in which the star's boundary exits the upper outer horizon r_+. That is: the origin of the advanced time in L is determined by the moment the star collapses into its own outer horizon forming a black hole and the origin of the retarded time in U is determined by the moment the star emerges from its own outer horizon ending the white hole.

3.3.4 Shock waves

Given the simplicity of the classical Oppenheimer-Snyder metric in Painlevé-Gullstrand coordinates (see eqs. (1.76) and (1.77)), it is natural to study also the quantum-corrected geometry in the same coordinates. Let us see what happens. The interior metric can be easily written in Painlevé-Gullstrand coordinates by performing the coordinate transformation $r = a(t)\,\tilde{r}$, where $a(t)$ is now the quantum-corrected scale factor. For the metric in the exterior of the star, it is sufficient to know that the differential of the Painlevé-Gullstrand coordinate time $t_{\rm PG}$ satisfies the relation

$$\mathrm{d}t_{\rm PG} = \mathrm{d}t - \frac{\sqrt{1-F}}{F}\,\mathrm{d}r\,. \tag{3.48}$$

The full spacetime metric can then be written as

$$\mathrm{d}s^2 = -\,\mathrm{d}t_{\rm PG}^2 + \Big(\mathrm{d}r + N^r(t_{\rm PG}, r)\,\mathrm{d}t_{\rm PG}\Big)^2 + r^2\,\mathrm{d}\Omega^2\,, \tag{3.49}$$

where

$$N^r(t_{\rm PG}, r) = \begin{cases} -\frac{6r(t_{0,\rm PG}-t_{\rm PG})}{9(t_{0,\rm PG}-t_{\rm PG})^2+A} & r \le r_{\rm b}(t_{\rm PG}) \\ \sqrt{1-F(r)} & r > r_{\rm b}(t_{\rm PG}) \end{cases} \tag{3.50}$$

and

$$r_{\rm b}(t_{\rm PG}) = \left(\frac{9m(t_{0,\rm PG}-t_{\rm PG})^2 + Am}{2}\right)^{1/3}. \tag{3.51}$$

This is exactly the metric found in Kelly et al. [132, 134] by separately studying the quantum corrections to the interior and the exterior metrics directly in Painlevé-Gullstrand coordinates. This proves the overall consistency of the quantum-corrected Oppenheimer-Snyder model.

There is a problem, however. The function $N^r(t_{\rm PG}, r)$ in eq. (3.50) becomes discontinuous for $t_{\rm PG} > 0$. This is immediately seen from the fact that the expression valid in the interior of the star changes sign after the bounce while the expression valid outside the star does not. In Kelly et al. [112, 134] this discontinuity was tentatively interpreted as a physical discontinuity of the gravitational field and it was argued that a shock wave must form as a consequence of it.

We have however now all the ingredients to clarify the reason for the discontinuity of the function $N^r(t_{\rm PG}, r)$. Consider the exterior vacuum region defined by eqs. (3.38) and (3.39) in the absence of the star. The Carter-Penrose diagram of this spacetime is given in fig. 3.4. The Painlevé-Gullstrand coordinate time $t_{\rm PG}$ is the proper time of radially free-falling observers that start at rest at infinity. In Schwarzschild spacetime, such observers all hit the spacelike singularity inside the black hole. But this is no longer the case in the quantum-corrected exterior metric. In the latter, the trajectories of free-falling observers starting at rest at infinity satisfy

$$\dot{r}^2 = 1 - F(r)\,. \tag{3.52}$$

All these trajectories have a turning point at $\dot{r} = \sqrt{1-F} = 0$, which is solved by $r = r_M$ (see eq. (3.4)). This means that instead of hitting the timelike curvature singularity in the interior of the black hole, radially free-falling observers reach a minimum distance from it at $r = r_M$ and then bounce back out of the hole in a second future asymptotically flat region. A few of these trajectories, together with the constant $t_{\rm PG}$ surfaces at the time of their turning point, are plotted in fig. 3.4.

From this discussion, it is clear that the Painlevé-Gullstrand coordinates cannot cover the vacuum spacetime region at $r < r_M$. The Painlevé-Gullstrand coordinate time $t_{\rm PG}$ is the proper time of the radially free-falling observers

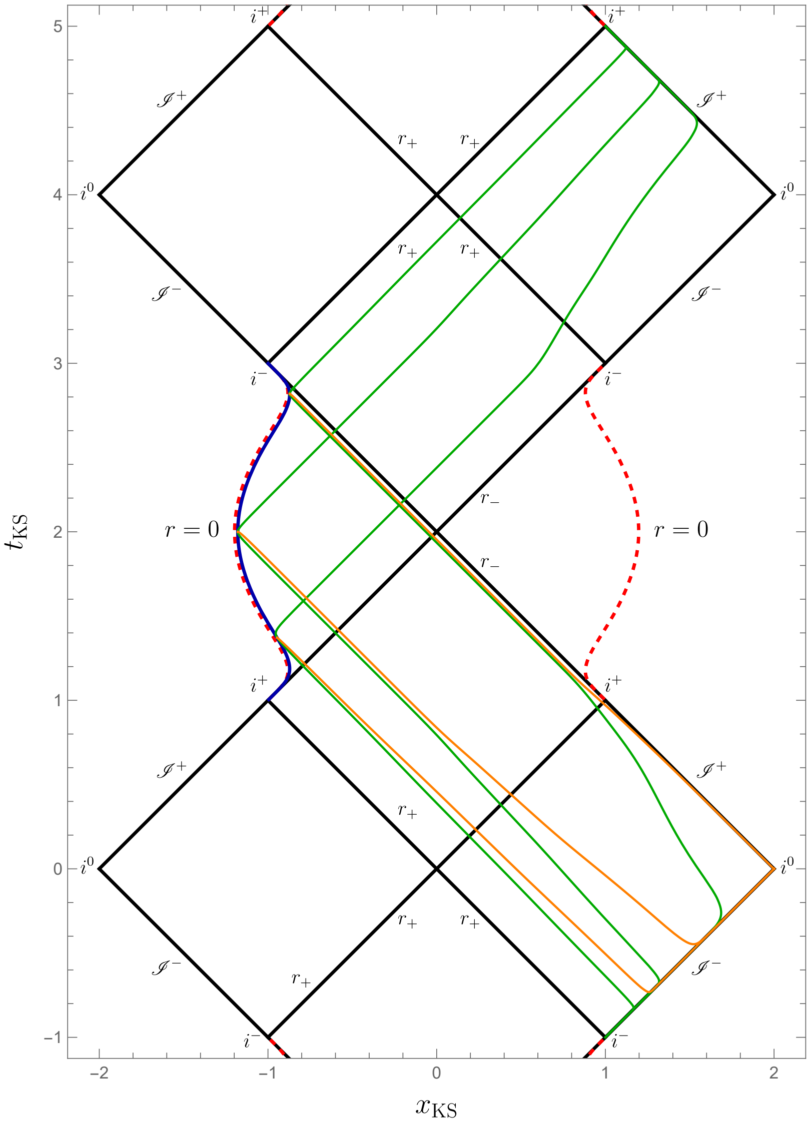

Figure 3.4: Carter-Penrose diagram of the spacetime defined by eqs. (3.38) and (3.39) in the absence of the star with $m = 1$ and $A = 0.99$ (Planck units). The trajectories of three different radially free-falling observers are plotted in green and the constant t_{PG} surfaces at the time of their turning point are plotted in Orange. The blue line represents the turning-point surface $r = r_M$.

and none of these observers penetrates inside the $r = r_M$ surface: there is no Painlevé-Gullstrand coordinate time t_{PG} inside the region at $r < r_M$. This is consistent with the expression of the quantum-corrected metric in Painlevé-Gullstrand coordinates given in eqs. (3.49) and (3.50). In fact, since $N^r(t_{\mathrm{PG}}, r) = \sqrt{1 - F(r)}$, the metric is well defined only for $1 - F(r) > 0$, which is

$$r > r_M. \tag{3.53}$$

This same constraint was found in Kelly et al. [132] during the construction of the quantum-corrected vacuum exterior region from loop quantum gravity first principles. This constraint was interpreted as a physical property of the quantum-corrected spacetime. The discussion above shows that it is an artifact of the specific coordinate system employed.

In fact, this is a general phenomenon. As pointed out in Faraoni and Vachon [135], the Painlevé-Gullstrand coordinates fail wherever the Misner-Sharp mass of the spacetime is negative, as is precisely the case in the metric defined by eqs. (3.38) and (3.39) for $r < r_M$.

Furthermore, fig. 3.4 clearly shows that the Painlevé-Gullstrand coordinates do not cover the full spacetime region traversed by the radially free-falling observers, and hence also by the boundary of the star in the quantum-corrected Oppenheimer-Snyder model, but only the spacetime region they cover before their turning point. There is then no hope for the Painlevé-Gullstrand coordinates to provide a global coordinate patch for the quantum-corrected Oppenheimer-Snyder model, as instead they do in the classical case.

Consider then the interior geometry of the star. The coordinate t_{PG} is the proper time of observers moving at constant comoving radial coordinate $\tilde{r}$, which in the area coordinate r becomes

$$r(t_{\mathrm{PG}}) \propto a(t_{\mathrm{PG}})\,. \tag{3.54}$$

This means that the time coordinate t_{PG} in the interior region is well adapted to bouncing observers, with $t_{\mathrm{PG}} =$ const. surfaces adapted to infalling observers for $t_{\mathrm{PG}} < 0$ and to outgoing observers for $t_{\mathrm{PG}} > 0$. So, while the exterior t_{PG}

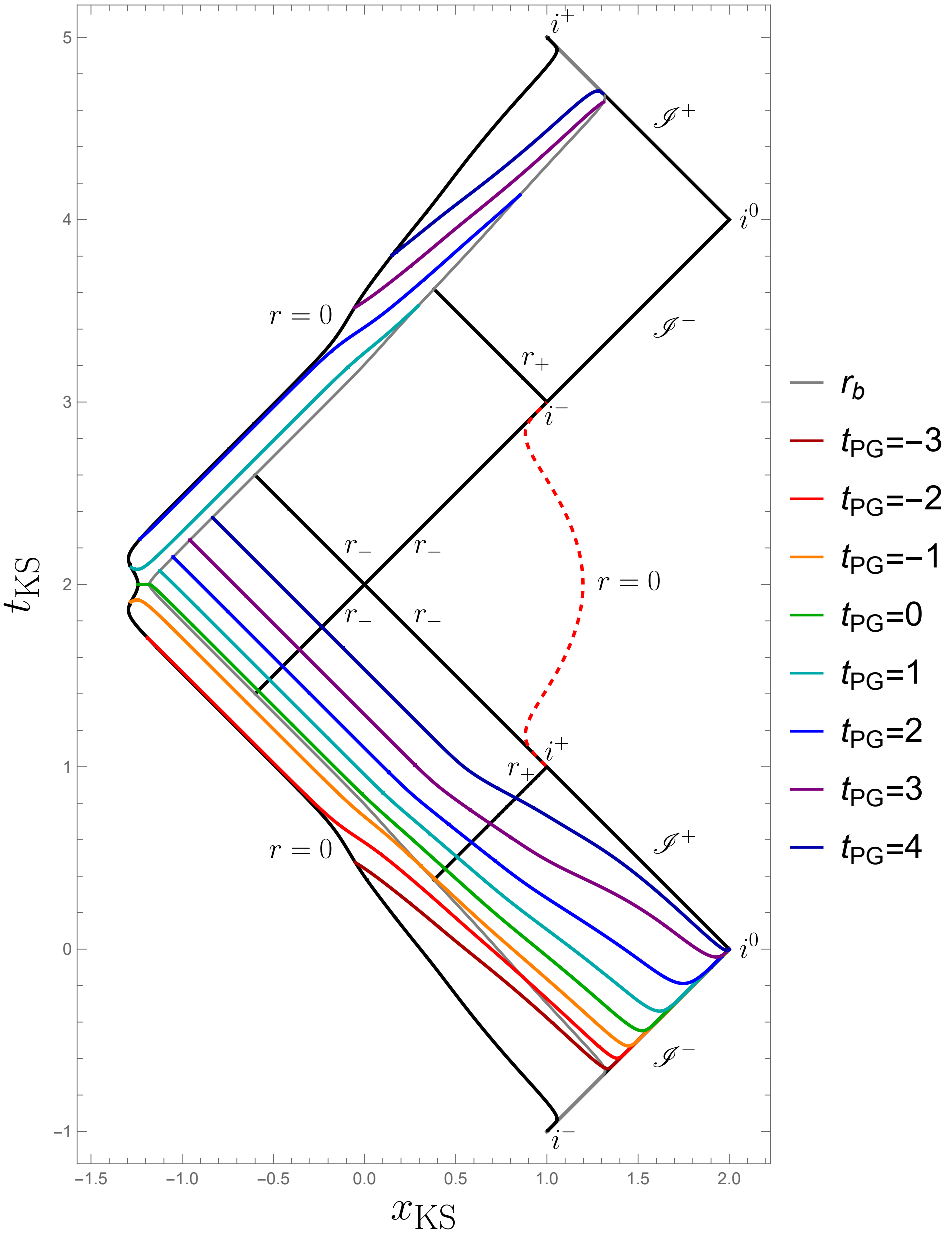

Figure 3.5: Carter-Penrose diagram of the quantum-corrected Oppenheimer-Snyder spacetime with $m = 1$ and $A = 0.99$ (Planck units) and with different surfaces $t_{\mathrm{PG}} = \text{const.}$ shown.

coordinate is only adapted to infalling observers, the interior one is adapted to bouncing observers. This generates a discontinuity in the $t_{\mathrm{PG}} = $ const. surfaces at the star's boundary for $t_{\mathrm{PG}} > 0$, as it can be clearly seen from fig. 3.5. This in turn generates the discontinuity in the metric in eqs. (3.49) and (3.50). This shows that the metric of the quantum-corrected Oppenheimer-Snyder model does not have any discontinuity and no shock wave ever forms.

Interestingly, although shock waves do not form in an Oppenheimer-Snyder model, a recent investigation by Fazzini et al. [136] seems to suggest that this is no longer true in more general collapse scenarios where the interior of the star is modeled using the Lemaître-Tolman-Bondi spacetime. So shock waves might be a general feature of more realistic gravitational collapse models.

3.4 Region $\mathscr{B}$: The physics of the horizon

The spacetime of the quantum-corrected Oppenheimer-Snyder model represented in fig. 3.3 takes into account the quantum physics of regions $\mathscr{A}$ and $\mathscr{C}$. The quantum physics of region $\mathscr{B}$ is still missing. As a consequence, this spacetime cannot be a realistic approximation of the global structure of the spacetime of a black hole because as soon as the Hawking evaporation process is taken into account, the lifetime of the black hole as seen from the lower asymptotically flat region L becomes finite. This is incompatible with the geometry of fig. 3.3, where this lifetime is infinite.

As discussed in section 1.2.4, the dynamics of the horizon at the end of the evaporation process is governed by quantum gravity. The quantum physics of regions $\mathscr{A}$ and $\mathscr{C}$ consistently points towards a transition of the black hole geometry into a white hole geometry. The most natural scenario for region $\mathscr{B}$ compatible with this physics is the existence of a non-vanishing probability for the geometry around the black hole horizon to tunnel into the geometry around a white hole horizon via a local process within a single asymptotic region [43, 121–124]. The computation of the probability for this transition will be performed in the next chapter. A naive analogy with non-relativistic quantum tunneling suggests that the tunneling probability could be of order

$\exp\big(-m^2/\hbar G\big) = \exp\big(-m^2/m_{\rm P}^2\big)$. If so, the transition probability would be highly suppressed until the very last phases of the black hole evaporation, where $m \sim m_{\rm P}$, and the tunneling physics specified below describes the tunneling geometry at the end of the evaporation. If instead the transition probability is not so suppressed at larger m, the tunneling may happen earlier (a heuristic argument in favor of a shorter timescale is given in Haggard and Rovelli [43, 137]).

Notice however that even if we entirely disregard the evaporation process and the consequent decrease of m with time, any non-zero transition probability implies anyway that sooner or later the tunneling happens, because small probabilities pile up with time, as in ordinary radioactivity. So the inclusion of the evaporation process in the analysis should not alter the resulting qualitative picture. For this reason in the following we neglect the evaporation process and we make no assumption about the transition probability of the tunneling, which can be arbitrarily small.

In this section, we construct the spacetime describing the tunneling of the horizon. We do so starting from the quantum Oppenheimer-Snyder spacetime in fig. 3.3, cutting away the part of spacetime that is not consistent with the existence of a transition of the horizon, inserting a new spacetime region in which the quantum tunneling takes place, and gluing some resulting boundaries. This whole construction will be carried out using hand-drawn Carter-Penrose diagrams instead of computer-generated ones. Although the latter ones are more rigorous, hand-drawn diagrams allow us to convey the desired information in a fast and effective way without obsessing over detail.

Let us start by fixing three constants r_α, r_β and r_δ with the dimension of a length and satisfying $r_\alpha < r_- < r_+ < r_\delta < r_\beta$. We shall also use $\delta \equiv r_\delta - r_+ > 0$. The geometry we are going to define is thus based on these four parameters in natural units: $m, r_\alpha, r_\beta, r_\delta$ (plus $A \sim m_{Pl}^2 = \hbar G$ that determines a scale). We are particularly interested in the regime where r_α is close to r_-, and r_β (and so r_δ) is close to r_+.

In region I, consider the $t =$ const. surface containing the bounce point of the star (see fig. 3.6). On this surface, let α be the point with radial coordinate

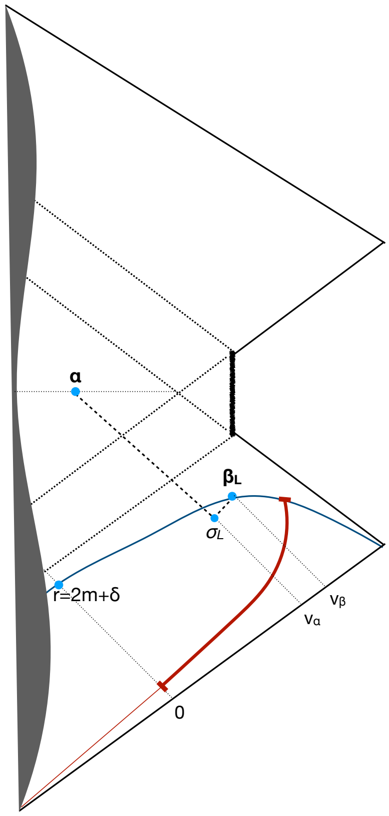

Figure 3.6: Qualitative Carter-Penrose diagram of spacetime showing the points (two-spheres) α, β_L, σ_L. In blue, the surface $t = 0$ and its intersection with $v = 0$. In red, the worldline of an observer at a constant distance.

r_α (the first of the parameters for the geometry we are constructing). Let v_α be the advanced time of α. This is going to be the advanced time at which the horizon transition begins. It is a simple exercise to express v_α as a function of r_α. First, we have to determine the advanced time v_b of the bounce point of the star. This can be determined from a standard calculation in general relativity and it is of order m. The t coordinate of the star's bounce is then

$$t = v_b - r_*(r_b), \tag{3.55}$$

and since α is on the same t surface, we also have

$$t = v_\alpha - r_*(r_\alpha). \tag{3.56}$$

The two relations imply

$$v_\alpha = v_b + r_*(r_\alpha) - r_*(r_b), \tag{3.57}$$

which does not depend on the undetermined integration constant of $r_*(r)$ in I. If r_α approaches r_-, the advanced time v_α can be arbitrarily long, as r_* diverges in r_-. We are particularly interested in this regime, where the time from the collapse of the star to the onset of the horizon tunneling can be arbitrarily long. The radial coordinate r_α is going to be the maximum radius on the $t =$ const. surface in region I for which the metric constructed in section 3.3 is a good approximation of the spacetime of a black hole.

Next, observe that all constant-t time surfaces in the L region intersect the line $v = 0$ outside the outer horizon. Recall in fact that $v = 0$ is the advanced time of the point where the boundary of the star enters the outer horizon. We insist on this detail because it is a counter-intuitive feature of classical general relativity. The later the time t, the closer to the horizon the constant-t surface intersects $v = 0$. Consider the constant time surface that intersects $v = 0$ at the radius $r_\delta = r_+ + \delta$ (the second of the parameters that we introduce). An arbitrarily small δ determines an arbitrarily late t. Later on, this time t will determine the reflection surface under time inversion. Without loss of generality, we can call this surface $t = 0$, because this simply amounts to fixing once and for all the integration constant of $r_*(r)$ in region L, and representing it in a qualitative Carter-Penrose diagram of spacetime as in fig. 3.7. Explicitly, the intersection has coordinates $v = t = 0$ and $r \sim 2m + \delta$. Therefore eq. (3.43) fixes $r_*(r_\delta) = 0$.

Consider then the point β_L with radius r_β (the third parameter we introduce) on the $t = 0$ surface. Let v_β be its advanced time. We assume that the constants we have introduced are such that $v_\beta > v_\alpha$. Given r_α and r_β, this is always possible by taking δ small enough. We are particularly interested in the regime

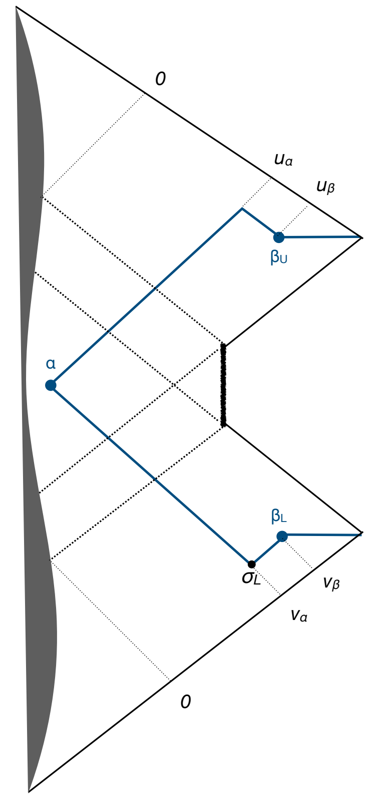

Figure 3.7: The blue line is the boundary of the region that is excised because it is not a good approximation of the spacetime of a physical black hole. The two horizontal portions of the blue line are identified; the excised region is replaced by a non-singular geometry.

in which r_β is close to r_+. Since $r_\beta > r_\delta = 2m + \delta > r_+$, this means that δ must be small. Let σ_L be the intersection of the past outgoing radial null geodesic originating in β_L and the past ingoing radial null geodesic originating in α. These null geodesics are represented as dashed lines in fig. 3.6 and as blue lines in fig. 3.7.

The above construction in the regions L, T, I can be repeated symmetrically in the upper regions U, A, I. See fig. 3.7. By symmetry, the retarded time coordinate u of α in the upper region is $u_\alpha = v_\alpha$. We consider a constant-t surface in the upper region U as well, which we can call $t = 0$ by fixing the integration constant of $r_*(r)$ in region U, and a point β_U with radius r_β. Its retarded time is $u_\beta = v_\beta$.

With these definitions in place, we now come to the key point of the construction. We excise from the spacetime the entire region surrounded by the blue line in fig. 3.7. We identify β_L with β_U and the $(t = 0, r > r_\beta)$ surface in the lower asymptotic region with the $(t = 0, r > r_\beta)$ surface in the upper asymptotic region. The gluing is possible since these are isometric surfaces with vanishing extrinsic curvature in the two isometric outer regions. Call $\mathscr{B}$ the spacetime diamond defined by α, $\beta \equiv \beta_L = \beta_U$, σ_L, and σ_U, and discard any previous information about the metric inside $\mathscr{B}$. The resulting spacetime is the black-to-white hole spacetime we were looking for and it has the qualitative Carter-Penrose diagram depicted in fig. 3.8.

The geometry outside the $\mathscr{B}$ region depicted in fig. 3.8 is everywhere locally isomorphic to the geometry in the exterior of the blue lines depicted in fig. 3.7, but the two are not globally isomorphic. The interior region S bounded by a timelike singularity discovered in the spacetime constructed in section 3.3 is not present in the black-to-white hole spacetime. There is a unique asymptotic region in the exterior of both black and white holes. As we shall see below, a non-singular metric can be assigned to the region $\mathscr{B}$. This will be done below, in Section 3.7.

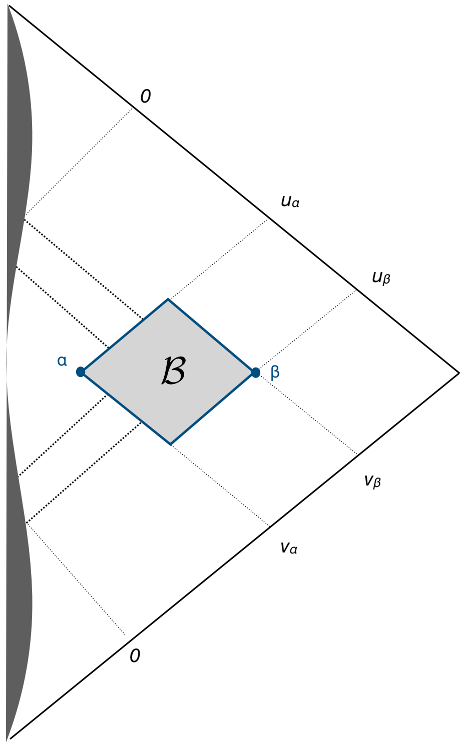

Figure 3.8: Qualitative conformal diagram of the black-to-white hole spacetime.

3.5 Physical interpretation and large scale geometry

Let us pause to discuss the physical interpretation and the logic of this construction and of the new parameters introduced. The advanced-time v_α is the time at which the horizon transition is triggered. The radial coordinate r_α, which is uniquely specified by v_α and vice versa, is the maximum radius on the $t =$ const. surface in region I containing the bounce point of the star for which the metric constructed in section 3.3 is a good approximation of the spacetime of a black hole. The radial coordinate r_σ is the maximum radius on the $v = v_\alpha$ surface for which the quantum physics of the horizons is non-negligible. The metric constructed in section 3.3 is not a good approximation of the spacetime of a black hole in the future lightcone of σ_L, because it neglects the possibility of tunneling. Since the black-to-white hole spacetime has a unique asymptotic region, the metric constructed in section 3.3 must not be a good approximation of the spacetime of a real black hole also in the future of some surface reaching spacelike infinity in the lower region L. This is the $t = 0$ surface identified by δ which intersects the outgoing component of the future light cone of σ_L in β_L. The radius r_σ is completely specified once r_α and r_β are given.

Let's now consider the features of this geometry that can be measured at a large radius. At first sight, since the geometry at a large distance from the hole is the Schwarzschild geometry, one might think that the only parameter measurable at a large distance is the mass m, but this is wrong.

Consider an observer that remains at distance $R \gg 2m$ from the hole. Consider their proper time T between their $v = 0$ advanced time and their $u = 0$ retarded time (that is from the advanced time in which the star enters its horizon and the retarded time in which the star exits it). Their worldline is shown in red in fig. 3.9. By symmetry, T is twice the proper time along this worldline between the $v = 0$ advanced time and the $t = 0$ surface, namely the proper time of the worldline in red in fig. 3.6. This is approximately the negative t-coordinate t_R of the observer at $v = 0$, that is

$$T/2 \sim -t_R = r_*(R) - v = r_*(R). \tag{3.58}$$

For $R \gg m \gg m_{\mathrm{P}}$, recalling that we have fixed $r_*(r_\delta) = 0$, we have

$$r_*(R) \sim R + 2m\ln(R - 2m) - 2m\ln\delta. \tag{3.59}$$

Using this,

$$T \sim 2R + 4m\ln(R - 2m) - 4m\ln\delta. \tag{3.60}$$

The first two terms of this expression depend on R. Not so the last term

$$\mathcal{T} \equiv -4m\ln\delta. \tag{3.61}$$

This is independent from the observer and is large and positive when δ is small.

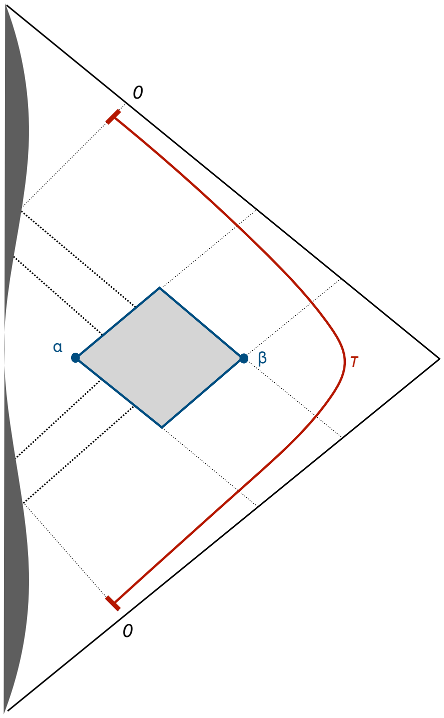

Figure 3.9: In red is the worldline of an observer moving at a constant distance $R \gg 2m$ in the qualitative Carter-Penrose diagram of the black-to-white hole spacetime.

This means that δ can be measured by comparing the proper times of two distant observers.

Let's see this more explicitly since it is a key point. The first term in eq. (3.60), namely $2R$, is the travel time of light from an observer at radius R to the center and back, in flat spacetime. The second (logarithmic) term is a relativistic correction to this travel time in the Schwarzschild geometry. This can be seen by comparing T with the corresponding proper time T' of a second distant observer at a constant radius R' satisfying $R \gg R' \gg 2m$. The difference between these proper times is

$$\begin{aligned} T - T' &\sim 2R - 2R' + 2m\ln(R-2m) - 2m\ln(R'-2m) \\ &\sim R + 2m\ln(R-2m), \end{aligned} \tag{3.62}$$

which shows that the first two terms in eq. (3.60) simply account for the back and forward travel-time of light and they are not related to the actual lifetime of the hole.

The quantity $\mathcal{T}$ is, therefore, a parameter that can be measured from a distance and characterizes the intrinsic duration of the full process of formation of the black hole, tunneling into a white hole, and dissipation of the white hole. We can therefore properly call the quantity $\mathcal{T}$ the duration of the bounce, or "bounce time". We have thus found the geometrical interpretation of δ in terms of the total bounce time $\mathcal{T}$:

$$\delta = e^{-\frac{\mathcal{T}}{4m}}. \tag{3.63}$$

Notice that δ, unlike r_α and r_β and in spite of being small, is a macroscopic parameter. Namely, it is a parameter of the global geometry that can be determined by measurements at a large distance from the hole. The gluing of the upper and lower regions in fig. 3.7 introduces this global parameter, in the same manner in which gluing two portions of flat space can introduce the radius of a cylinder: a global parameter not determined by the local geometry. The two other parameters r_α and r_β determine only the location of the $\mathscr{B}$ region, without affecting the observations at large distances. Large distance observations are therefore determined by two parameters only: the mass m of the star and δ, or the bounce time $\mathcal{T} = -4m\ln\delta$.

3.6 Global coordinate chart for the black-to-white hole spacetime

Using eqs. (3.43) and (3.47) the advanced time coordinate v can be defined everywhere except for the region specified by $v \in [v_\alpha, v_\beta]$ and $u \in [u_{star}(v), u_\alpha]$,

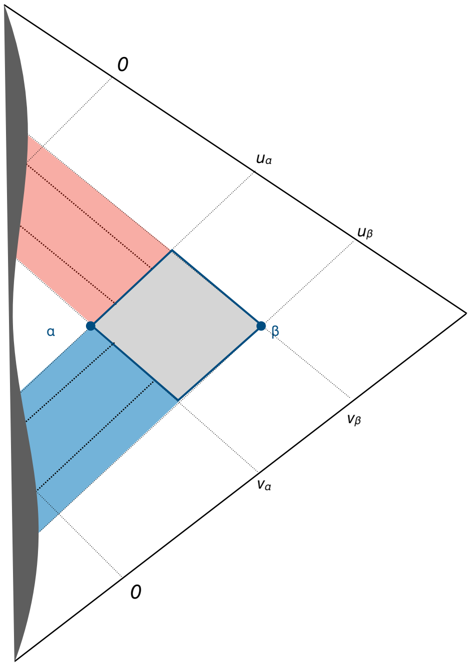

Figure 3.10: In red, the region defined by $v \in [v_\alpha, v_\beta]$ and $u \in [u_{star}(v), u_\alpha]$. In blue, the region defined by $u \in [u_\alpha, u_\beta]$ and $v \in [v_{star}(u), v_\alpha]$.

where $u_{star}(v)$ represent the wordline of the boundary of the star in (u, v) coordinates. This region is depicted in red in fig. 3.10. If we continue the v coordinate into this red region, it diverges on the two horizons. Similarly, the u coordinate is well defined everywhere except for the region specified by $u \in [u_\alpha, u_\beta]$ and $v \in [v_{star}(u), v_\alpha]$, represented in blue in fig. 3.10. In this section, we construct a regular global coordinate chart for the entire spacetime outside region $\mathscr{B}$ (and outside the star). This will also allow us to write a regular and non-singular metric inside region $\mathscr{B}$ in the next section.

Starting from the coordinate v, introduce a smooth function $f(v)$ such that $f(v) = v$ for $v < v_\alpha$ and $v > v_\beta$, while for $v \in [v_\alpha, v_\beta]$ the function $f(v)$ ranges in $[v_\alpha, \infty) \cup (\infty, -\infty) \cup (-\infty, v_\beta]$, diverging logarithmically in two points, that we call v_+ and v_-. Specifically, let

$$f(v) = v + R(v) \tag{3.64}$$

where $R(v) = 0$ outside the interval $v \in [v_\alpha, v_\beta]$, and in this interval is defined as

$$R(v) = 2h(v)\Big(c_+ \log|v - v_+| + c_- \log|v - v_-|\Big), \tag{3.65}$$

with $v_\alpha < v_- < v_+ < v_\beta$ and $c_\pm = 1/F'(r_\pm)$. The constants $c_\pm$ are the same that multiply the divergent logarithms in the expression of $r_*(r)$ in eq. (3.37). The function $h(v)$ can be chosen to be any function that transitions smoothly between $h(v_\alpha) = h(v_\beta) = 0$ and $h(v_-) = h(v_+) = 1$. A simple example represented in fig. 3.11 is $h(v) = 0$ for $v < v_\alpha$ and $v > v_\beta$, $h(v) = g_\uparrow(v, v_\alpha, v_-)$ for $v \in [v_\alpha, v_-]$, $h(v) = 1$ for $v \in [v_-, v_+]$, and $h(v) = g_\downarrow(v, v_+, v_\beta)$ for $v \in [v_+, v_\beta]$, where $g_{\uparrow\downarrow}(X, a, b)$ are the transition functions defined in chapter 2.

We then define a new v coordinate in the red region by

$$f(v) = 2r_*(r) - u\,, \tag{3.66}$$

instead than eq. (3.43). The coordinate v defined in this way covers the red region in its range $v \in [v_\alpha, v_\beta]$ and matches with the v coordinate defined elsewhere. Notice that $2r_*(r) - u$ diverges on the horizons, but v, so defined, does not: on the horizons it takes the finite values v_- and v_+. Hence u and (this newly defined) v are finite and smooth coordinates in the red region. For v to be a good coordinate for the region, we also need to check that the metric is well-defined there. This can be done as follows.

The line element in the red region reads

$$\mathrm{d}s^2 = F(r(u,v))f'(v)\,\mathrm{d}u\,\mathrm{d}v + r^2(u,v)\,\mathrm{d}\Omega^2. \tag{3.67}$$

Near the horizon $r = r_\pm$ the function $F(r)$ has a zero of the form $r - r_\pm$ while $f'(v)$ diverges as the derivative of the logarithm, namely $1/(v - v_\pm)$. In

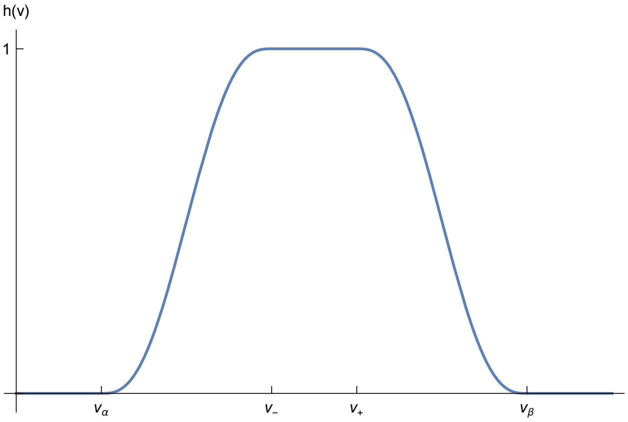

Figure 3.11: Plot of the smooth transition function $h(v)$.

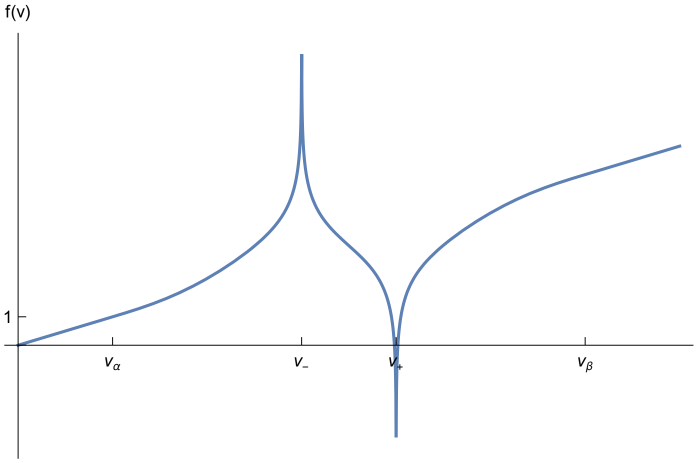

Figure 3.12: Plot of the function $f(v)$ defined in eqs. (3.64) and (3.65).

particular, the g_{uv} component of the metric behaves as

$$g_{uv} = \frac{F(r)f'(v)}{2} \sim \frac{r - r_\pm}{v - v_\pm} \tag{3.68}$$

near the horizon $r = r_\pm$. Let us now study the transformation in eq. (3.66) around the horizons. For $r \sim r_\pm$, eq. (3.37) gives

$$r_*(r) \sim c_\pm \log|r - r_\pm| + \mu_1 \,, \tag{3.69}$$

with

$$\begin{aligned} \mu_1 =& r_\pm + c_\mp \log|r_\pm - r_\mp| + \frac{c_1}{2}\log\bigl(r_\pm^2 + a r_\pm + b\bigr) \\ &+ \frac{(2c_1/c_2 - a)}{\sqrt{b - a^2/4}} \tan^{-1}\left(\frac{r_\pm + a/2}{\sqrt{b - a^2/4}}\right) + K \,. \end{aligned} \tag{3.70}$$

If $v \sim v_\pm$, then eqs. (3.64) and (3.65) give

$$f(v) \sim 2c_\pm \log|v - v_\pm| + \mu_2 \,, \tag{3.71}$$

with

$$\mu_2 = c_\mp \log|v_\pm - v_\mp| . \tag{3.72}$$

This means that near the horizon $r = r_\pm$ eq. (3.66) reads

$$2c_\pm \log|v - v_\pm| + \mu_2 - 2c_\pm \log|r - r_\pm| - 2\mu_1 \sim u \,, \tag{3.73}$$

namely

$$\frac{r - r_\pm}{v - v_\pm} \sim e^{-\frac{2\mu_1 - \mu_2}{2c_\pm}} e^{-\frac{u}{2c_\pm}} \,. \tag{3.74}$$

The metric component g_{uv}, and so the complete metric, is thus well-behaved around the horizons.

The same construction can be performed in the symmetric blue region. Given the values $u_\pm \equiv v_\pm$, and remembering that $u_\alpha = v_\alpha$ and $u_\beta = v_\beta$ by construction, we define a new u coordinate in the blue region by

$$f(u) = 2r_*(r) - v\,, \tag{3.75}$$

where the function f is given in eqs. (3.64) and (3.65). The coordinate u defined in this way covers the blue region in its range $u \in [u_\alpha, u_\beta]$ and matches with the u coordinate defined elsewhere. The line element in the blue region reads

$$\mathrm{d}s^2 = F(r(u,v))f'(u)\ \mathrm{d}u\ \mathrm{d}v + r^2(u,v)\,\mathrm{d}\Omega^2 \tag{3.76}$$

and it is well behaved everywhere. This completes the construction of a global coordinate chart for the black-to-white hole spacetime.

Summarizing, the line element of the black-to-white hole spacetime in this global double-null coordinate system (u, v, θ, ϕ) is given by

$$\mathrm{d}s^2 = g(u,v)\ \mathrm{d}u\ \mathrm{d}v + r^2(u,v)\,\mathrm{d}\Omega^2. \tag{3.77}$$

In the white regions of fig. 3.10, namely where

$$u \in [u_\beta, +\infty) \quad \text{and} \quad v \in [v_{star}(u), +\infty)\,, \tag{3.78}$$

$$u \in [u_{star}(v), +\infty) \quad \text{and} \quad v \in [v_\beta, +\infty)\,, \tag{3.79}$$

$$u \in [u_{star}(v_\alpha), u_\alpha] \quad \text{and} \quad v \in [v_{star}(u), v_\alpha]\,, \tag{3.80}$$

we have

$$g(u,v) = F(r(u,v)) \tag{3.81}$$

and the radius $r(u,v)$ is implicitly given by

$$2r_*(r) = v + u\,. \tag{3.82}$$

In the red region specified by

$$u \in [u_{star}(v), u_\alpha] \quad \text{and} \quad v \in [v_\alpha, v_\beta]\,, \tag{3.83}$$

we have

$$g(u,v) = F(r(u,v))f'(v) \tag{3.84}$$

and the radius $r(u,v)$ is implicitly given by

$$2r_*(r) = f(v) + u = v + u + R(v). \tag{3.85}$$

In the blue region specified by

$$u \in [u_\alpha, u_\beta] \quad \text{and} \quad v \in [v_{star}(u), v_\alpha]\,, \tag{3.86}$$

we have

$$g(u,v) = F(r(u,v))f'(u) \tag{3.87}$$

and the radius $r(u,v)$ is implicitly given by

$$2r_*(r) = v + f(u) = v + u + R(u). \tag{3.88}$$

This metric is everywhere regular.

3.7 An effective metric in the $\mathscr{B}$ region

Can the $\mathscr{B}$ region be filled with an effective Lorentzian metric that joins regularly with the exterior metric at their boundary? To show that the answer is affirmative, let us now construct one such metric.

The smooth transition function $g_\downarrow(X,a,b)$ can be used to rewrite the metric constructed in the last section in a more compact form. Let in fact $S(X)$ be

$$S(X) = g_\downarrow(X, v_\alpha, v_\beta). \tag{3.89}$$

This allows us to write compactly (see eq. (3.77))

$$g(u,v) = F(r(u,v))\, f(u,v)\,, \tag{3.90}$$

where

$$f(u,v) = \big(1 + S(u)R'(v)\big(\big)\ \big((1 + S(v)R'(u)\big(\big) \tag{3.91}$$

and $r(u,v)$ is implicitly defined by

$$2r_*(r) = v + u + S(u)R(v) + S(v)R(u)\,. \tag{3.92}$$

The transition function $S(x)$, so far, serves only to simplify notation: it does not actually affect the metric, which for the moment does not cover the $\mathscr{B}$ region defined by

$$u \in [u_\alpha, u_\beta] \quad \text{and} \quad v \in [v_\alpha, v_\beta]\,. \tag{3.93}$$

To extend the metric to the $\mathscr{B}$ region, the idea is to simply extend eqs. (3.77), (3.90) and (3.92) to the $\mathscr{B}$ region. The global coordinate system (u, v, θ, ϕ) constructed in the last section extends naturally to this region because the coordinate intervals of the null coordinates are the same on the opposite sides of the diamond boundary of the $\mathscr{B}$ region. Furthermore, thanks to the properties of the function $R(X)$, the functions $f(u,v)$ and $r(u,v)$ defined on the whole black-to-white hole spacetime (outside the star) join regularly at the boundary of the region $\mathscr{B}$.

Equations (3.77), (3.90) and (3.91) can then be used to extend the metric to the complete black-to-white hole spacetime outside the star, thus providing an (arbitrary) effective Lorentzian metric describing the interior of the region $\mathscr{B}$.

3.8 Spacetime horizons

Finally, we study the structure of the horizons defined by the Lorentzian metric we have constructed in the region $\mathscr{B}$.

There are no event horizons: the past of future null infinity is the entire spacetime.

There are no global Killing horizons. This is due to the fact that the local Killing symmetry is broken in the $\mathscr{B}$ region (and in the star). This can be shown as follows. The norm $|\xi|$ of a Killing field ξ is conserved along its own

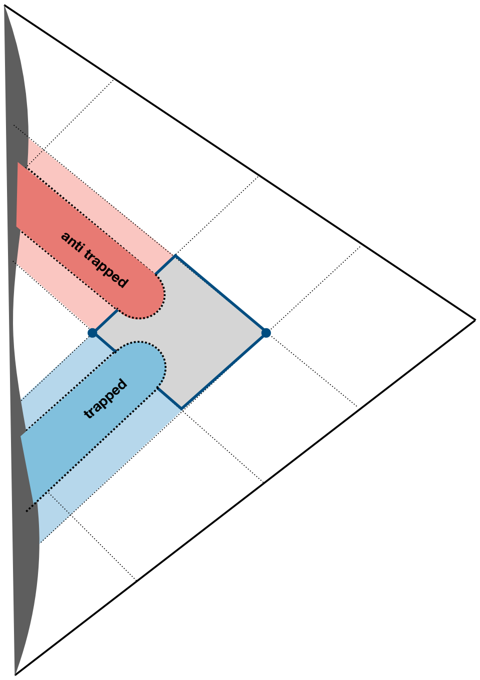

Figure 3.13: One of the possible qualitative behaviors of the apparent horizons.

integral lines because the Lie derivative $\mathcal{L}_\xi|\xi| = \mathcal{L}_\xi(g_{ab}\xi^a\xi^b)$ vanishes, as the Lie derivative of each factor does. Take one of the Killing horizons outside region $\mathscr{B}$, say $u = u_\pm$. It is a null integral line of the Killing field. If the Killing symmetry was respected in $\mathscr{B}$, its integral line would remain null. So, it would follow the radial null geodesic. The radial null geodesic is $u =$ const., so the Killing horizon would have to continue to the outer region through region $\mathscr{B}$. But it does not. Hence, the Killing symmetry is broken inside the $\mathscr{B}$ region and there is no global Killing horizon.

This is comprehensible physically: what happens inside the $\mathscr{B}$ region is a quantum tunneling, and a tunneling breaks stationarity. This, by the way, is why calculations that impose a global Killing symmetry outside the star miss the possibility of the tunneling.

The horizons in the red and blue regions are however not only local Killing

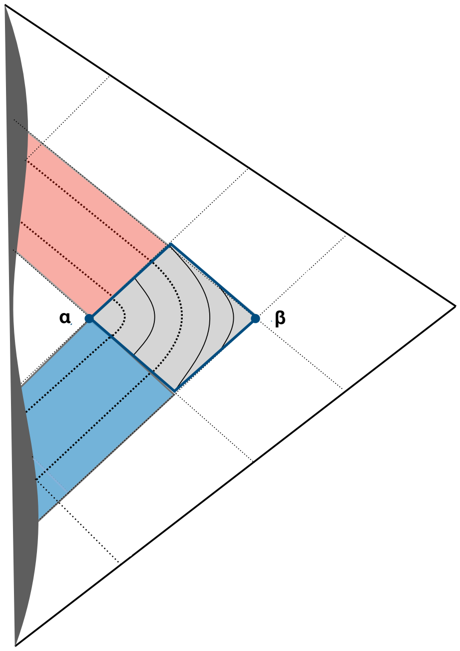

Figure 3.14: One of the possible qualitative behaviors of the surfaces of constant radius.

horizons, but also apparent horizons. That is, they separate trapped, non-trapped, and anti-trapped regions. These regions can be characterized by the causal character of the $r =$ const. surfaces, which are timelike in the non-trapped regions and spacelike in the trapped and anti-trapped regions. By continuity, the apparent horizons must continue inside the $\mathscr{B}$ region. How?

The qualitative way they continue inside $\mathscr{B}$ follows from a topological consideration. The overall spacetime is symmetric under a past-future flip. Call Σ_0 the $u = v$ reflection surface. By reflection symmetry, the $r =$ const. surfaces can only be either parallel or orthogonal to Σ_0. Outside region $\mathscr{B}$ they are clearly orthogonal to Σ_0, both in the asymptotic exterior region and in the interior region where the star's bounce takes place. By continuity, since the $r =$ const. surfaces cannot jump from orthogonal to parallel to Σ_0, they must be (almost) everywhere orthogonal to Σ_0, also inside region $\mathscr{B}$. Given that only timelike surfaces can be orthogonal to Σ_0, the internal non-trapped region is expected to be connected to the external one through the region $\mathscr{B}$. A possible way for this to happen is that the apparent horizons qualitatively behave as in fig. 3.13, making sure that the trapped and anti-trapped regions are compact and do not share a finite boundary. The surfaces of constant radius would then have the qualitative form represented in fig. 3.14.

Chapter 4

Spin foam framework for the black-to-white hole transition

A version of this chapter has been published in Physical Review D as

F. D'Ambrosio, M. Christodoulou, P. Martin-Dussaud, C. Rovelli and F. Soltani. "End of a black hole's evaporation". *Phys. Rev. D* **104** (2021), 066015. DOI: 10.1103/PhysRevD.103.106014. Copyright © 2021 by American Physical Society. All rights reserved.

F. Soltani, C. Rovelli and P. Martin-Dussaud. "End of a black hole's evaporation. II". *Phys. Rev. D* **103** (2021), 106014. DOI: 10.1103/PhysRevD.104.066015. Copyright © 2021 by American Physical Society. All rights reserved.

4.1 Introduction

A concrete spacetime for the black-to-white hole transition has been proposed in chapter 3. The constructed metric describes the entire spacetime except for the quantum region $\mathscr{B}$, where the black hole horizon undergoes a tunneling transition. Although the same construction can be used to naturally assign a non-singular metric also to region $\mathscr{B}$, the latter is ultimately a deep quantum region whose physics must be investigated using a fully-fledged non-perturbative quantum theory of the gravitational field. The covariant formulation of loop quantum gravity introduced in section 1.3.3 is the perfect tool for the job. The transition amplitude for the entire quantum region, that is the entire dark grey region in fig. 3.1, was first roughly estimated using covariant loop quantum gravity in Christodoulou et al. [122, 138, 139]. In this chapter, we use the covariant formulation of loop quantum gravity to begin a more refined study of the physics of region $\mathscr{B}$ alone.

In order to use the spin foam formalism to investigate the physics of region $\mathscr{B}$, the latter needs to be properly discretized. There is no unique or right way to perform the discretization. However, in order to get simpler and clearer calculations throughout the spin foam analysis it is particularly useful to preserve as many symmetries as possible during the procedure. The choice of the boundary for the $\mathscr{B}$ region, together with its intrinsic and extrinsic geometry, is given in section 4.2. The discretization of this boundary is then performed in section 4.3. Section 4.4 is devoted to the construction of the two-complex $\mathcal{C}$ that discretizes the $\mathscr{B}$ region. This two-complex is dual to a cellular complex which is not a four-dimensional triangulation. This choice has the advantage of providing a relatively simple discretization that respects the symmetries of the problem. Finally, the explicit expression of the transition amplitude for the black-to-white tunneling of the horizon is given in section 4.5.

4.2 The boundary of the $\mathscr{B}$ region

The starting point for the spin foam computation performed in this chapter is the black-to-white hole spacetime constructed in chapter 3. Hawking radiation and the subsequent evaporation of the black hole have been completely neglected in this construction. While this provides a good approximation of the qualitative picture of spacetime, as it was argued in chapter 3, it is not clear that it provides also a good first-order approximation of the quantitative physics of region $\mathscr{B}$, where Hawking radiation may very well be quite intense. However, for lack of a better model, we'll content ourselves to investigate the physics of region $\mathscr{B}$ in the absence of Hawking radiation.

Furthermore, as discussed in section 1.2.5, the onset of quantum gravitational effects in the three quantum regions $\mathscr{A}$, $\mathscr{B}$, and $\mathscr{C}$ is triggered by different physical phenomena in causally disconnected regions of spacetime. It should then be possible to study them independently from each other. We will then use this freedom to approximate the geometry around region $\mathscr{B}$ when the horizon transition is triggered by a Schwarzschild metric, up to the existence of a minimum radius r_α in the interior of the black hole in order to be consistent with the interior physics of region $\mathscr{A}$.

4.2.1 Choice of the boundary

The idea to define a boundary for the $\mathscr{B}$ region is to first surround it with a diamond-shaped null surface Σ in the Carter-Penrose diagram of spacetime (like in fig. 3.8), that is a diamond null surface times a two-sphere in spacetime, and then, since an appropriate boundary for computing transition amplitudes must be spacelike, to slightly deform Σ into a spacelike surface. This surface will then be the Heisenberg cut we choose, namely the surface we shall take as the boundary between the quantum and the classical regions.

We want now to concretely specify Σ and compute its intrinsic and extrinsic geometry. Since Hawking radiation has been neglected, the $\mathscr{B}$ region must be time-reversal invariant. The surface Σ can consequently be seen as the union of two surfaces, a past one Σ^p and a future one Σ^f, equal up to time reflection, $\Sigma = \Sigma^p \cup \Sigma^f$. Here, the labels p and f stand for past and future, and later on we shall also use the index $t = \{p, f\}$ (hence Σ^t) where t stands for time. Accordingly, we only need to study the past boundary Σ^p, as the future boundary Σ^f is determined by symmetry.

The metric around the $\mathscr{B}$ region is taken to be well approximated by the Schwarzschild metric up to the existence of a minimum radius r_α in the interior of the black hole in order to be consistent with the interior physics of region $\mathscr{A}$. The past boundary Σ^p is then contained in regions I and II of the Carter-Penrose diagram of Schwarzschild spacetime in fig. 1.2. Since these regions can be simultaneously covered by the ingoing Eddington-Finkelstein coordinates, we

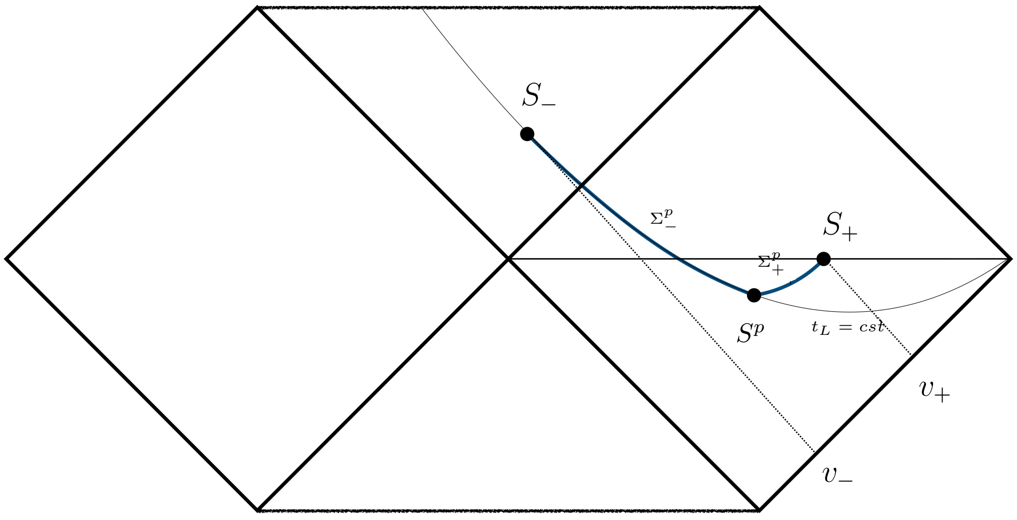

Figure 4.1: The past portion of the boundary surface.

can use these coordinates to define Σ^p. The line element in these coordinates reads

$$\mathrm{d}s^2 = -\left(1 - 2m/r\right)\mathrm{d}v^2 + 2\mathrm{d}r\,\mathrm{d}v + r^2\,\mathrm{d}\Omega^2, \tag{4.1}$$

and the Schwarzschild time coordinate t is related to the ingoing Eddington–Finkelstein coordinates by

$$t = v - r_* = v - r - 2m\ln\left|r/2m - 1\right| \tag{4.2}$$

or

$$\mathrm{d}t = \mathrm{d}v - \frac{\mathrm{d}r}{(1 - 2m/r)}. \tag{4.3}$$

The null past diamond boundary can be defined in the Carter-Penrose diagram of spacetime as follows. Let S_{out} be a point (a two-sphere in spacetime) outside the horizon at advanced time v_+ and Schwarzschild time $t = 0$. Let S_{in} be a point inside the horizon at advanced time $v_- < v_+$ and Schwarzschild radius $r_- = r_\alpha$. The null past diamond boundary is taken to be the union of the outgoing past radial light cone of S_{out} and of the ingoing past radial light cone of S_{in} from their intersection upward. See fig. 4.1.

Note that the presence of a minimum finite radius r_α in the construction fixes the value r_- of the Schwarzschild radius of the point S_{in} consistently with the physics of region $\mathscr{A}$ discussed in chapter 3. Furthermore, being the Schwarzschild radius r a temporal coordinate inside the black hole, while the radius r_+ of S_{out} is a measure of the spatial coordinate distance of S_{out} from the horizon, the radius $r_- = r_\alpha$ must not be interpreted as a measure of the spatial coordinate distance of S_{in} from the horizon but as the minimal internal radius reached by the black hole in region $\mathscr{A}$.

To simplify the notation, in the following we replace the labels *out* and *in* with the index $\pm = \{+,-\} \equiv \{out, in\}$, e.g. $S_+ \equiv S_{out}$ and $S_- \equiv S_{in}$.

Next, we define the spacelike past boundary Σ^p by slightly deforming the null past diamond boundary while keeping fixed S_+ and S_-. A convenient choice of deformation is the following one. Consider the surface Σ^p_- of constant Lemaître time coordinate [140]

$$t_L = t + 2\sqrt{2mr} + 2m \ln \left| \frac{\sqrt{r/2m} - 1}{\sqrt{r/2m} + 1} \right| \tag{4.4}$$

passing by S_- and the surface Σ^p_+ defined by

$$v - \beta r = \text{const.}, \tag{4.5}$$

passing by S_+, for some constant $\beta \in \mathbb{R}$. Let S^p be their intersection as shown in fig. 4.1. We choose the spacelike past boundary Σ^p to be the union of the portion of Σ^p_- between S^p and S_- and the portion of Σ_+ between S^p and S_+. The parameter β can be fixed by requiring the continuity of the normal to Σ^p at S^p.

The spacelike future boundary surface Σ^f is defined to be the time-reversal of the surface Σ^p and the full spacelike boundary surface Σ is then partitioned in the four components Σ^p_+, Σ^p_-, Σ^f_+ and Σ^f_- as in fig. 4.2. The Carter-Penrose diagram of the $\mathscr{B}$ region so constructed consists of two separate portions of the Carter-Penrose diagram of Schwarzschild spacetime which are appropriately joined. This is the same "cutting and pasting" first introduced in Haggard and Rovelli [43] that was used in chapter 3 to construct the black-to-white hole spacetime.

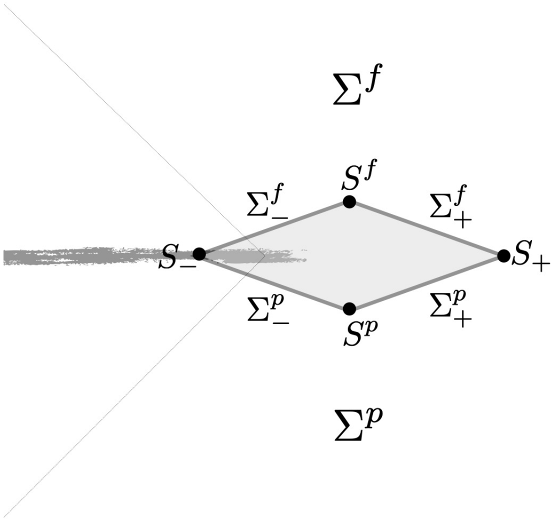

Figure 4.2: Qualitative Carter-Penrose diagram of the $\mathscr{B}$ region with the surface Σ and its components highlighted.

4.2.2 Intrinsic and extrinsic geometry

We now need to determine the intrinsic and the extrinsic geometry of Σ. The intrinsic geometry of Σ^p_+ is obtained by differentiating its defining equation (equation (4.5)),

$$\mathrm{d}v = \beta \mathrm{d}r, \tag{4.6}$$

and inserting the result in the line element in equation (4.1). This gives

$$\mathrm{d}s^2_+ = \beta\left(2 - \beta\left(1 - 2m/r\right)\right)\mathrm{d}r^2 + r^2\,\mathrm{d}\Omega^2. \tag{4.7}$$

To find the intrinsic geometry of Σ^p_-, we rewrite the explicit expression of the Lemaître time coordinate in equation eq. (4.4) in terms of the (v, r) coordinates. Then we differentiate it, finding that on a constant t_L surface the following relation is satisfied:

$$\mathrm{d}v = \frac{\mathrm{d}r}{1+\sqrt{2m/r}}\,. \tag{4.8}$$

Using this relation in the line element in equation (4.1), we obtain that the line element resulting from the intrinsic metric of the Σ_-^p surface is

$$\mathrm{d}s_-^2 = \mathrm{d}r^2 + r^2\,\mathrm{d}\Omega^2. \tag{4.9}$$

That is, Σ_-^p is intrinsically flat.

Next, we want to determine the extrinsic geometry of Σ. Since the two surfaces Σ_+^p and Σ_-^p are both defined by constraint equations of the form $C = 0$, it is easy to compute their normal 1-forms using

$$n_\mu = -\frac{\partial_\mu C}{|\partial^\nu C \partial_\nu C|^{1/2}}. \tag{4.10}$$

In Schwarzschild coordinates, the normals to the surfaces Σ_-^p and Σ_+^p are then given by

$$n_\mu^- = \left(-1, -\frac{\sqrt{2mr}}{r-2m}, 0, 0\right)\,, \tag{4.11}$$

$$n_\mu^+ = \frac{\left(-1, \beta - \left(1-2m/r\right)^{-1}, 0, 0\right)}{\left|\beta\left(\beta - 2 - 2m\beta/r\right)\right|^{1/2}}\,. \tag{4.12}$$

Demanding that the normals match on S^p, uniquely fixes the value of β to

$$\beta = \frac{1}{1+\sqrt{\frac{2m}{r_{S^p}}}}. \tag{4.13}$$

To deal with the extrinsic curvature of the surfaces $\Sigma_\pm^p$ it is easier to express them as systems of parametric equations $x_\pm^\mu = x_\pm^\mu(y_\pm^a)$, where $y_\pm^a$ are some parameters which serve as intrinsic coordinates to the surfaces. Given a generic surface defined by the system of parametric equations $x^\mu = x^\mu(y^a)$ for some y^a, the tangent 1-form to the surface e^μ_a is given by

$$e^\mu_a = \frac{\partial x^\mu}{\partial y^a} \tag{4.14}$$

and the extrinsic curvature tensor k_{ab} of the surface is

$$k_{ab} = e^\mu_a e^\nu_b \nabla_\mu n_\nu \,. \tag{4.15}$$

Let $k^\pm_{ab}$ be the extrinsic curvature of $\Sigma^p_\pm$. Then, a straightforward calculation gives

$$k^- \equiv k^-_{ab}\, \mathrm{d}x^a \mathrm{d}x^b = \sqrt{\frac{m}{2r^3}}\, \mathrm{d}r^2 - \sqrt{2mr}\, \mathrm{d}\Omega^2 \tag{4.16}$$

and

$$\begin{aligned} k^+ \equiv k^+_{ab}\, \mathrm{d}x^a \mathrm{d}x^b =& \frac{m\beta^{3/2}(r(3-\beta)+2m\beta)}{\sqrt{r^5(r(2-\beta)+2m\beta)}}\, \mathrm{d}r^2 \\ &- \frac{r(1-\beta)+2m\beta}{\sqrt{\beta(2-(1-2m/r)\beta)}}\, \mathrm{d}\Omega^2 \,. \end{aligned} \tag{4.17}$$

This completes the computation of the geometry of the boundary of region $\mathscr{B}$. This geometry is entirely determined by four parameters: the mass m, the Schwarzschild radii $r_\pm$ of the spheres $S_\pm$, which by construction satisfy

$$r_- < 2m < r_+ \,, \tag{4.18}$$

and the retarded time $v = v_+ - v-$. The physical interpretation of these four parameters is transparent. The mass m is the mass of the black hole. The retarded time v is the external (asymptotic) time it takes for the transition to happen. The radius r_+ is the minimal external radius where we assume the classical physics to be reliable. The radius r_- is the minimal internal radius reached by the black hole interior in region $\mathscr{A}$. These parameters are basically the same parameters determining the local geometry of the $\mathscr{B}$ region in the black-to-white hole spacetime constructed in chapter 3. This shows that the transition amplitude that will be computed in section 4.5 can be used as a first approximation of the transition amplitude of the $\mathscr{B}$ region in the black-to-white hole spacetime.

4.3 The triangulation of Σ

The topology of the $\mathscr{B}$ region is $S^2 \times [0,1] \times [0,1]$ and the topology of its boundary $\partial\mathscr{B} = \Sigma = \Sigma^p \cup \Sigma^f$ is $S^2 \times S^1$.

We can identify two symmetries of the geometry of Σ and one symmetry of its topology:

- The Z_2 time reversal symmetry that exchanges p and f.
- The SO(3) symmetry inherited by the spherical symmetry of the overall geometry.
- A Z_2 symmetry that exchanges the internal (minimal radius) sphere S_- and the external (maximal radius) sphere S_+. This is a symmetry of the topology, but not of the geometry, since S_- and S_+ have different sizes.

To find a triangulation of Σ we discretize the two spheres S_- and S_+ into regular tetrahedra. This replaces the continuous SO(3) symmetry with the discrete symmetries of a tetrahedron. In particular, we discretize each of the two spheres $S_\pm$ in terms of a tetrahedron $t_\pm$. We label the four vertices of each tetrahedron as $p^\pm_a$ where $a = 1, 2, 3, 4$; and the triangles bounding the tetrahedra as $L^\pm_a$, where the triangle $\ell^\pm_a$ is opposite to the vertex $p^\pm_a$.

Thanks to the Z_2 time-reversal symmetry, the triangulations describing Σ^p and Σ^f must be topologically equivalent. For this reason, the same construction can be applied to both. A convenient triangulation for Σ^t is the following one. The placement of the smaller tetrahedron t_- inside the bigger tetrahedron t_+, which can be chosen arbitrarily, is taken to be as in fig. 4.3 and 4.4, such that the vertex p^-_a lies on the segment linking the centroid of the tetrahedron t_+ (which coincides with the centroid of the tetrahedron t_-) and the centroid of the face L^+_a. Then, each vertex p^+_a of t_+ is linked to the three vertices of the triangle L^-_a, creating 14 tetrahedra in total.

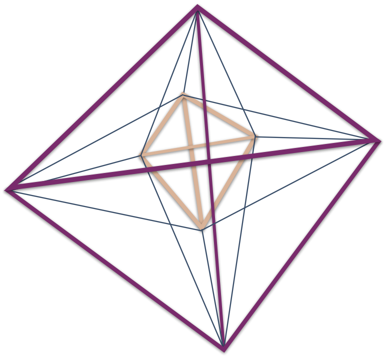

Figure 4.3: The triangulation of Σ^t. The brown tetrahedron t_- is inscribed into the larger violet tetrahedron t_+. The blue segments connect the vertices of the two tetrahedra radially.

We call N_a^{t+} (violet in fig. 4.4) the tetrahedron having L_a^+ as one of its faces and N_a^{t-} (brown in fig. 4.4) the tetrahedron having L_a^- as one of its faces. Each of the six remaining tetrahedra (blue in fig. 4.4) is bounded by two of the N_a^{t+} tetrahedra and two of the N_a^{t-} tetrahedra. Noting that the labels given to the N_a^{t+} and N_a^{t-} tetrahedra are such that each of the six remaining tetrahedra is bounded by a set of tetrahedra N_b^{t+}, N_b^{t+}, N_d^{t-}, and N_e^{t-}, with $b \neq c \neq d \neq e$, we can then label the six remaining tetrahedra as $N_{bc}^t \equiv N_{cb}^t$, where the labels b and c refer to N_b^{t+} and N_b^{t+}. Clearly, from N_{bc}^t one can readily trace back the other two tetrahedra N_d^{t-} and N_e^{t-}.

The full triangulation of Σ is constructed identifying each $L_a^{\pm}$ face of Σ^p with the $L_a^{\pm}$ face of Σ^f. This completely defines the triangulation of Σ. The complexity of the triangulation chosen is due to the non-trivial topology of Σ and from the computational opportunity of choosing a triangulation that respects the symmetries of the problem.

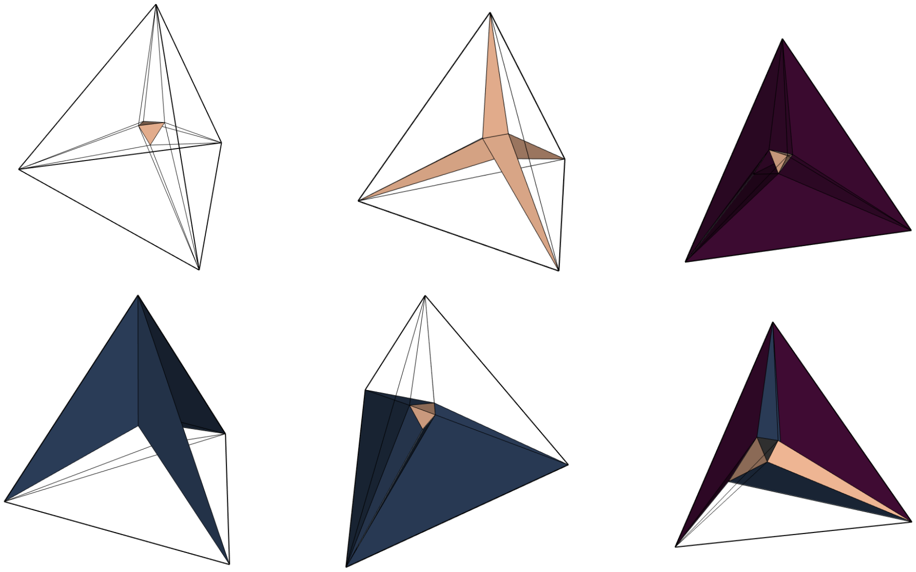

Figure 4.4: All images represent the triangulation of Σ^t, but with different tetrahedra highlighted. In the top left no tetrahedron is highlighted (the tetrahedron t_- is in brown to remind that it is hollowed inside); in the top center the four N_a^{t-} are highlighted; in the top right three N_a^{t+} out of four are highlighted; in the bottom left three N_{ab}^t out of six are highlighted; in the bottom center the remaining three N_{ab}^t are highlighted; in the bottom right two N_a^{t-}, two N_a^{t+} and two N_{cd}^t are highlighted.

4.3.1 The dual of the triangulation

In covariant loop quantum gravity one works with the dual of a cellular decomposition of a spacetime region. More precisely, the spin foam that captures the discretized degrees of freedom of the geometry is supported by the two-skeleton of the dual of the cellular decomposition. The boundary of the spin foam is the boundary spin-network, which is dual to the boundary triangulation.

The spin-network graph Γ dual to the discretization of Σ we have constructed is illustrated in fig. 4.5. Each circle is a node of the spin-network, and represents a tetrahedron, and each link joining two nodes represents a triangle separating two tetrahedra. Intersections of links in this two-dimensional graph representation have no meaning.

Since the information carried by the graph of a spin-network is only in its

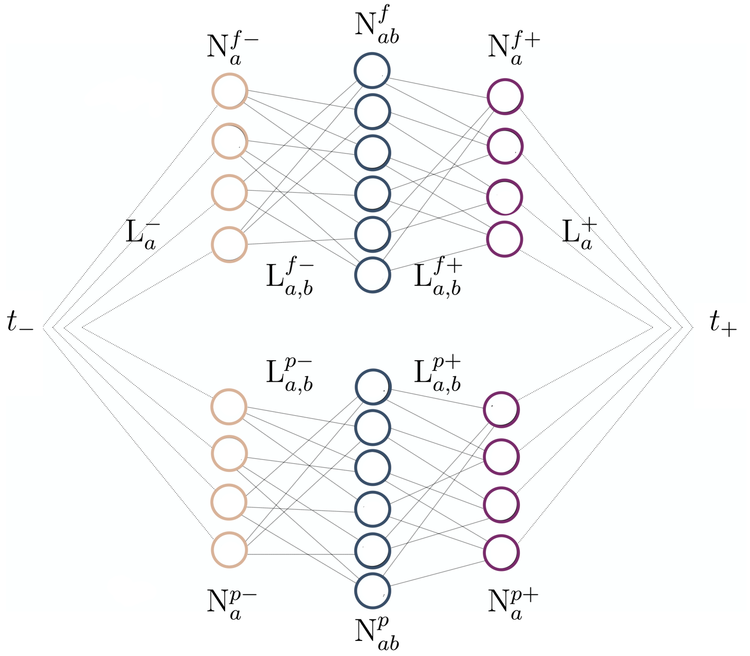

Figure 4.5: Two-dimensional representation of the graph Γ dual to the triangulation of Σ.

topology, as long as the latter remains unchanged, the graph can be deformed at will. Although the graphical representation of the dual graph Γ in fig. 4.5 is completely fine to represent the topological information of the spin-network, it is not the best choice to manifestly represent all of its symmetries. A more symmetrical representation is the one in figs. 4.6 and 4.7.

Although the graph Γ is quite complicated, thanks to the symmetries of the problem it has only two kinds of nodes that are topologically distinct (using the same label to denote dual objects): the $N_a^{t\pm}$ nodes and the N_{ab}^t nodes. The symmetries act by permuting the a indices and exchanging p with f or $+$ with $-$. Geometrically, the N_a^{t+} nodes differ from the N_a^{t-} ones, as the last symmetry is not geometrical. For the same reasons, there are only four kinds of links up to geometrical symmetries (two kinds up to topological symmetries). These correspond to:

- The 4 links L_a^+ dual to triangles forming the discretized sphere S_+.
- The 4 links L_a^- dual to triangles forming the discretized sphere S_-. To-

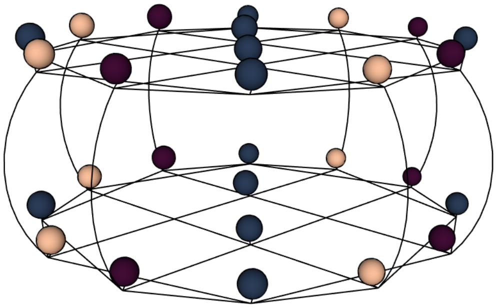

Figure 4.6: Three-dimensional representation of the graph Γ dual to the triangulation of Σ. Each node is represented as a sphere colored consistently with its dual tetrahedron in fig. 4.4.

gether with the L^{+}_{a} links they connect Σ^{p} with Σ^{f} (they are the vertical links in fig. 4.6).

- The 24 links $L^{t+}_{a,b}$ (12 for each t) dual to the internal triangles separating the boundary tetrahedra N^{t+}_{a} (violet) from the internal tetrahedra N^{t}_{ab} (blue).
- The 24 links $L^{t-}_{a,b}$ (12 for each t) dual to the internal triangles separating the boundary tetrahedra N^{t-}_{a} (brown) from the internal tetrahedra N^{t}_{cd} (blue) with $a \neq b \neq c \neq d$.

Notice that in all the expressions with several indices $a, b, \ldots$ these are assumed to be all different, that is $a \neq b$ and so on. Furthermore, unless two indices are separated by a comma, the order of the indices is not relevant, and exchanging the indices results in the same element. If two indices are separated by a comma, exchanging the indices results in a different element.

4.3.2 Discrete geometrical data

The geometrical data that characterizes the discretized geometry are the areas of the triangles and the angles between tetrahedra at these triangles. Hence, the relevant boundary data for the calculation is:

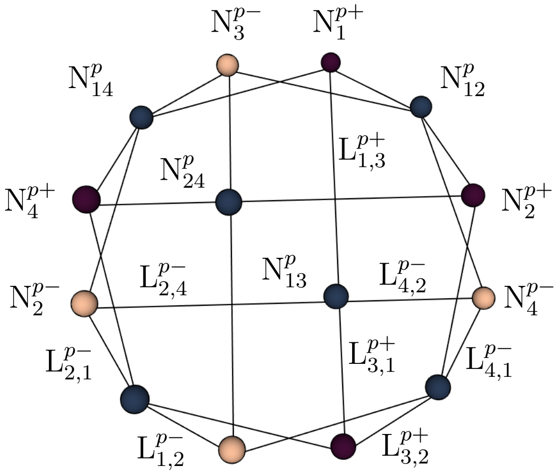

Figure 4.7: Two-dimensional representation of the past component of the graph Γ dual to the triangulation of Σ.

- The 2 areas $a_\pm$ of the internal and the external spheres $S_\pm$, which determine the areas associated to the links $L_a^\pm$.
- The 2 areas $A_\pm$ of the triangles dual to the $L_{a,b}^{t\pm}$ links.
- The 2 angles $k_\pm$ between $\Sigma_\pm^p$ and $\Sigma_\pm^f$ at the internal and external spheres, which determine directly the angles associated with the links $L_a^\pm$;
- The 2 angles $K_\pm$ that depend on the extrinsic curvature of $\Sigma_\pm$ and that are associated to the triangles dual to the $L_{a,b}^{t\pm}$ links. The angles in Σ^p have the opposite sign of the angles in Σ^f.

These eight numbers $c_n = (a_\pm, k_\pm, A_\pm, K_\pm)$ depend on the continuous geometry of Σ described in the previous section. Hence, they depend on the four parameters $m, r_\pm$, and v defined above. From the point of view of the dual graph Γ, the discrete geometry consists of the assignment of an area and an angle to each link of Γ. The area assigned to each link represents the area of the triangle that is dual to the link and the angle assigned to each link represents the extrinsic curvature between the two tetrahedra that share the triangle dual to the link. This geometrical data uniquely specifies a coherent state $\psi_{\rm BW} = \psi_{\rm BW}\big(a_\pm,\, k_\pm,\, A_\pm,\, K_\pm\big) = \psi_{\rm BW}\big(m,\, v,\, r_\pm\big) \in \mathcal{H}_\Gamma$, known as extrinsic coherent state in the covariant loop quantum gravity literature [89], that is peaked on the discrete classical geometry defined by $\big(a_\pm,\, k_\pm,\, A_\pm,\, K_\pm\big)$. The boundary state $\psi_{\rm BW} \in \mathcal{H}_\Gamma$ is the quantum state representing the outcome of the transition taking place in region $\mathscr{B}$. Namely, it is the boundary state representing a past black hole geometry on Σ^p and a future white hole geometry on Σ^f. This leads to the transition amplitude for the black-to-white hole transition as:

$$W(m, r_\pm, v) := W[\psi_{\rm BW}] = W\Big[\psi_{\rm BW}\big(a_\pm,\, k_\pm,\, A_\pm,\, K_\pm\big)\Big]\,. \tag{4.19}$$

In this section, we compute the numbers $c_n(m, r_\pm, v)$.

There is no unique or right way to assign discrete geometrical data to the graph Γ starting from the continuous geometry of Σ. Each choice defines a different approximation of the continuous geometry and it has its own strengths and its own weaknesses. In this section, we will introduce a convenient set of discrete geometrical data approximating the continuous geometry of Σ. We will discuss the discrete geometry of the triangulation approximating Σ^p. The discrete geometry of the triangulation approximating Σ^f is simply related to the first one by a time reversal transformation.

First of all, the area of the spheres $S_\pm$ is directly determined by the radii $r_\pm$. Since the four triangles $L^\pm_a$ bounding the tetrahedra $t_\pm$ that discretize the spheres $S_\pm$ are equal by symmetry, we take their area $a_\pm$ to be one fourth of the area of the spheres, that is

$$a_\pm = \pi r_\pm^2. \tag{4.20}$$

The side length $b_\pm$ of the tetrahedron $t_\pm$ is then trivially given by

$$b_\pm = \sqrt{\frac{4\pi}{\sqrt{3}}}\, r_\pm\,. \tag{4.21}$$

The line element $\mathrm{d}s^2$ on Σ^p can be written as

$$\mathrm{d}s^2 = f^2(r)\, \mathrm{d}r^2 + r^2\, \mathrm{d}\Omega^2\,, \tag{4.22}$$

where

$$f^2(r) = \beta\,[2 - \beta\,(1 - 2m/r)]$$

on Σ^p_+ (see equation (4.7)) and $f^2(r) = 1$ on Σ^p_- (see equation (4.9)). We approximate this line element as

$$\mathrm{d}s^2 = \alpha^2\,\mathrm{d}r^2 + r^2\,\mathrm{d}\Omega^2\,, \tag{4.23}$$

where α is a constant that needs to be determined. In order to do so, let V_{Σ^p} and $V^\alpha_{\Sigma^p}$ be the volume of the surface Σ^p whose intrinsic geometry is given respectively by equation (4.22) and (4.23). The volume V_{Σ^p} is given by

$$\begin{aligned} V_{\Sigma^p} &= \int_{\Sigma^t} \mathrm{d}^3x \sqrt{|\det g^{(3)}|} \\ &= \int_{\Sigma^t_+} \mathrm{d}r\,\mathrm{d}\theta\,\mathrm{d}\phi\, r^2 |\sin\theta| \sqrt{|\beta\,[2 - \beta\,(1 - 2m/r)]|} \\ &\quad + \int_{\Sigma^t_-} \mathrm{d}r\,\mathrm{d}\theta\,\mathrm{d}\phi\, r^2 |\sin\theta| \\ &= 4\pi \int_{\Sigma^t_+} \mathrm{d}r\, r^2 \sqrt{|\beta\,[2 - \beta\,(1 - 2m/r)]|} \\ &\quad + \frac{4\pi}{3}\left(r^3_{S^p} - r^3_-\right)\,. \end{aligned}$$

The integral over Σ^p_+ can be computed explicitly (with computer algebra) in the case in which β is fixed by the continuity at S^p. We do not give the explicit expression here. The volume $V^\alpha_{\Sigma^p}$ is instead given by

$$\begin{aligned} V^\alpha_{\Sigma^p} &= \int_{\Sigma^t} \mathrm{d}^3x \sqrt{|\det g^{(3)}_\alpha|} = \int_{\Sigma^t} \mathrm{d}r\,\mathrm{d}\theta\,\mathrm{d}\phi\, \alpha\, r^2 |\sin\theta| \\ &= \frac{4\pi\alpha}{3}\left(r^3_+ - r^3_-\right)\,. \end{aligned}$$

We fix the value of α by requiring that $V^\alpha_{\Sigma^p} = V_{\Sigma^p}$. This explicitly gives the value of α as a function of the spacetime free parameters (m, r_+, r_-, β).

We can now assign discrete geometrical data to the triangulation starting from the continuous intrinsic geometry in equation (4.23). Let us first consider the $\alpha = 1$ case. When $\alpha = 1$ the line element describes flat space and the intrinsic discrete geometry of the triangulation is completely determined by the side lengths $b_\pm$. Let $\widetilde{d}_p^{t_\pm}$, $\widetilde{d}_L^{t_\pm}$ and $\widetilde{h}_{t_\pm}$ be respectively the distance between the centroid and a vertex of the tetrahedron $t_\pm$, the distance between the centroid and a face of the tetrahedron $t_\pm$ and the height of the tetrahedron $t_\pm$. Basic geometry shows that

$$\widetilde{d}_p^{t_\pm} = \sqrt{\frac{3}{8}}\, b_\pm \,, \quad \widetilde{d}_L^{t_\pm} = \frac{1}{\sqrt{24}}\, b_\pm \,, \quad \widetilde{h}_{t_\pm} = \sqrt{\frac{2}{3}}\, b_\pm \,. \tag{4.24}$$

The height $\widetilde{h}_{N^\pm}$ of a tetrahedron $N_a^{p\pm}$ (they are all equal by symmetry) relative to the base $L_a^\pm$ can be expressed as

$$\widetilde{h}_{N^+} = \widetilde{d}_L^{t_+} - \widetilde{d}_p^{t_-} \quad \text{and} \quad \widetilde{h}_{N^-} = \widetilde{d}_p^{t_+} - \widetilde{d}_L^{t_-} \,. \tag{4.25}$$

It is then possible to define the volumes of all the tetrahedra, except the N_{ab}^p ones, as

$$\widetilde{V}_X = \frac{1}{3}\, \widetilde{h}_X \, a_X \,, \tag{4.26}$$

where $X = \{t_+, t_-, N^+, N^-\}$, $a_{t_+} = a_{N^+} = a_+$ and $a_{t_-} = a_{N^-} = a_-$. Finally, the volume $\widetilde{V}_N$ of a N_{ab}^p tetrahedron (they are all equal by symmetry) is given by

$$\widetilde{V}_N = \frac{1}{6}\left(\widetilde{V}_{t_+} - \widetilde{V}_{t_-} - 4\widetilde{V}_{N^+} - 4\widetilde{V}_{N^-}\right) \,. \tag{4.27}$$

This completely determines the intrinsic discrete geometry of the triangulation in the flat case in terms of $b_\pm$.

When $\alpha \neq 1$ the line element in equation (4.23) describes a three-dimensional cone. We are only interested in the region of the cone in which $r \in [r_-, r_+]$. Hence, in this approximation, Σ^p turns out to be locally flat. However, it cannot be embedded in a flat three-dimensional space in the same way in which a two-dimensional cone cannot be embedded in a flat two-dimensional space.

Let us focus on the three-dimensional curved geometry defined by the line element in equation (4.23). The consequence of the presence of α is simply a stretching of the radial lengths with respect to the geometry discussed in the

$\alpha = 1$ case while the tangential lengths remain fixed. In analogy with the $\alpha = 1$ case we can then define the following quantities:

$$d_p^{t\pm} = \alpha\, \widetilde{d}_p^{t\pm} = \sqrt{\frac{3}{8}}\, \alpha\, b_\pm\,, \tag{4.28}$$

$$d_L^{t\pm} = \alpha\, \widetilde{d}_L^{t\pm} = \frac{1}{\sqrt{24}}\, \alpha\, b_\pm\,, \tag{4.29}$$

$$h_{t_\pm} = \alpha\, \widetilde{h}_{t_\pm} = \sqrt{\frac{2}{3}}\, \alpha\, b_\pm\,, \tag{4.30}$$

$$h_{N^+} = \alpha\, \widetilde{h}_{N^+} = \alpha \left(\widetilde{d}_L^{t+} - \widetilde{d}_p^{t-} \right), \tag{4.31}$$

$$h_{N^-} = \alpha\, \widetilde{h}_{N^-} = \alpha \left(\widetilde{d}_p^{t+} - \widetilde{d}_L^{t-} \right). \tag{4.32}$$

The volumes of all the tetrahedra, except the N_{ab}^p ones, can be then written as

$$V_X = \frac{1}{3}\, h_X\, a_X = \frac{1}{3}\, \alpha\, \widetilde{h}_X\, a_X = \alpha\, \widetilde{V}_X\,, \tag{4.33}$$

where $X = \{t_+, t_-, N^+, N^-\}$, $a_{t_+} = a_{N^+} = a_+$ and $a_{t_-} = a_{N^-} = a_-$. Furthermore, since the curved counterpart of equation eq. (4.27) must still be valid, we can write

$$\begin{aligned} V_N &= \frac{1}{6} \left(V_{t_+} - V_{t_-} - 4V_{N^+} - 4V_{N^-} \right) \\ &= \frac{\alpha}{6} \left(\widetilde{V}_{t_+} - \widetilde{V}_{t_-} - 4\widetilde{V}_{N^+} - 4\widetilde{V}_{N^-} \right) \\ &= \alpha\, \widetilde{V}_N\,. \end{aligned} \tag{4.34}$$

The intrinsic discrete geometry of the triangulation is thus completely determined in terms of $b_\pm$ and α.

We are interested in the value of the areas $A_\pm$ of the triangles dual to the $L_{a,b}^{t\pm}$ links. These values are given by

$$A_\pm = \frac{1}{2} b_\pm h_\pm\,, \tag{4.35}$$

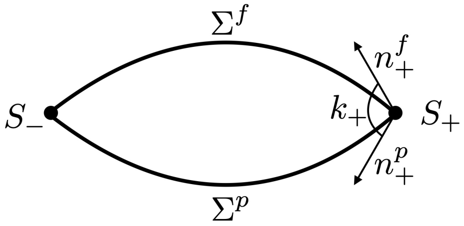

Figure 4.8: Definition of the angle k_+

where $h_\pm$ is the height of the triangles dual to $L^{t\pm}_{a,b}$ relative to $b_\pm$. Basic geometry shows that

$$h_\pm = \sqrt{h^2_{N^\pm} + \frac{1}{12} b^2_\pm} \, . \tag{4.36}$$

So

$$A_\pm = \pi r^2_\pm \sqrt{\frac{\alpha^2}{18}\left(1 - 3\frac{r_\mp}{r_\pm}\right)^2 + \frac{2}{3}} \tag{4.37}$$

With α fixed by the value of the total volume of Σ^p, equation (4.37) explicitly gives the value of the areas $A_\pm$ in terms of the spacetime free parameters (m, r_+, r_-, β).

Let us now focus on the extrinsic discrete geometry. The angles $k_\pm$, which are represented in fig. 4.8, are defined as

$$\cos k_\pm := \left(g^{\mu\nu} n^{\pm f}_\mu n^{\pm p}_\nu\right)\Big|_{S_\pm} \, . \tag{4.38}$$

It is then straightforward to find

$$\cos k_+ = \frac{1 + \left[(1 - 2m/r_+)\,\beta - 1\right]^2}{|\beta(\beta - 2 - 2m\beta/r_+)|(1 - 2m/r_+)} \tag{4.39}$$

and

$$\cos k_- = \frac{1 + 2m/r_-}{1 - 2m/r_-} \, . \tag{4.40}$$

The angles $K_\pm$ bear the extrinsic curvature of $\Sigma_\pm$. We choose to define them as the average of the extrinsic curvature, shared over the 12 triangles $L^{t\pm}_{a,b}$:

$$K_\pm = \frac{1}{12}\int_{\Sigma_\pm} k^a_a. \tag{4.41}$$

We have

$$\begin{aligned}(k^+)^a_a = &\left(1-\frac{2m}{r}\right)\frac{m\beta^{3/2}(r(3-\beta)+2m\beta)}{\sqrt{r^5(r(2-\beta)+2m\beta)}}\\ &-\frac{2}{r^2}\frac{r(1-\beta)+2m\beta}{\sqrt{\beta(2-(1-2m/r)\beta)}}\end{aligned} \tag{4.42}$$

and

$$(k^-)^a_a = -\sqrt{\frac{m}{2r^3}}\left(3+\frac{2m}{r}\right). \tag{4.43}$$

The integral in eq. (4.41)) can then be computed explicitly using computer algebra.

This completes the definition of the discrete geometric data, and with it the definition of the boundary state for the quantum transition. The four areas $a_\pm$ and $A_\pm$ and the four angles $k_\pm$ and $K_\pm$ have been explicitly found as functions of the four parameters $m, r_\pm$ and β (the parameter β can equivalently be traded for v).

4.4 Discretization of region $\mathscr{B}$

In this section, we construct the two-complex $\mathcal{C}$ that discretizes region $\mathscr{B}$. A particularly compact definition of the two-complex $\mathcal{C}$ is its combinatorial definition as a set of vertices, edges, and faces with their boundary relations.

If N_1 and N_2 are nodes, we write $\mathrm{L} = (\mathrm{N}_1, \mathrm{N}_2)$ to denote the oriented link with source N_1 and target N_2. We denote $\mathrm{L}^{-1} = (\mathrm{N}_2, \mathrm{N}_1)$ the same link but with opposite orientation. For the vertices and edges of the two-complex of the spin foam (which form a graph), we use an analogous notation. We denote the vertices as v; the internal edges (bounded by two vertices) as e; the external edges (bounded by one node) as E. Similarly, we denote the internal faces (bounded by internal edges only) as f; the external faces (with one link in the boundary) as F. We write $\mathrm{f} = (\mathrm{e}_1, \dots, \mathrm{e}_n)$ to denote the oriented face f bounded by these edges. The orientation of the face is given by the sequence of edges. These are written oriented accordingly to the orientation the face induces on them.

Let a, b, c, d be indices taking values in the set $\{1,2,3,4\}$, t be an index taking values in the set $\{p, f\}$ and ϵ be an index taking values in the set $\{-,+\}$. In all the expressions with several indices $a, b, \dots$ these are assumed to be all different, that is $a \neq b$ and so on. Unless two indices are separated by a comma, the order of the indices is not relevant, and exchanging the indices results in the same element. If two indices are separated by a comma, exchanging the indices results in a different element.

The combinatorial definition of the graph Γ dual to the three-dimensional triangulation of Σ is given by

Nodes: $\mathrm{N}_a^{t\epsilon}$ and N_{ab}^{t};

$$\text{Links:}\quad \begin{aligned} \mathrm{L}_a^{\epsilon} &= (\mathrm{N}_a^{p\epsilon}, \mathrm{N}_a^{f\epsilon}),\\ \mathrm{L}_{a,b}^{t+} &= (\mathrm{N}_{ab}^{t}, \mathrm{N}_a^{t+}),\\ \mathrm{L}_{a,b}^{t-} &= (\mathrm{N}_{cd}^{t}, \mathrm{N}_a^{t-}). \end{aligned}$$

The two-complex $\mathcal{C}$, whose boundary $\partial\mathcal{C}$ is given by Γ, is then defined as:

Vertices: v_a^{ϵ} and v_{ab};

$$\text{Edges:}\quad \begin{aligned} \mathrm{E}_a^{t\epsilon} &= (\mathrm{v}_a^{\epsilon}, \mathrm{N}_a^{t\epsilon}),\\ \mathrm{E}_{ab}^{t} &= (\mathrm{v}_{ab}, \mathrm{N}_{ab}^{t}),\\ \mathrm{e}_{a,b}^{+} &= (\mathrm{v}_a^{+}, \mathrm{v}_{ab}),\\ \mathrm{e}_{a,b}^{-} &= (\mathrm{v}_a^{-}, \mathrm{v}_{cd}); \end{aligned}$$

$$\text{Faces:}\quad \begin{aligned} \mathrm{F}_a^{\epsilon} &= \big(\mathrm{L}_a^{\epsilon}, (\mathrm{E}_a^{f\epsilon})^{-1}, \mathrm{E}_a^{p\epsilon}\big),\\ \mathrm{F}_{a,b}^{t+} &= \big(\mathrm{L}_{a,b}^{t+}, (\mathrm{E}_a^{t+})^{-1}, \mathrm{e}_{a,b}^{+}, \mathrm{E}_{ab}^{t}\big),\\ \mathrm{F}_{a,b}^{t-} &= \big(\mathrm{L}_{a,b}^{t-}, (\mathrm{E}_a^{t-})^{-1}, \mathrm{e}_{a,b}^{-}, \mathrm{E}_{cd}^{t}\big),\\ \mathrm{f}_{a,b} &\overset{c\leq d}{=} \big(\mathrm{e}_{a,c}^{+}, (\mathrm{e}_{b,d}^{-})^{-1}, \mathrm{e}_{b,c}^{-}, (\mathrm{e}_{a,d}^{+})^{-1}\big). \end{aligned}$$

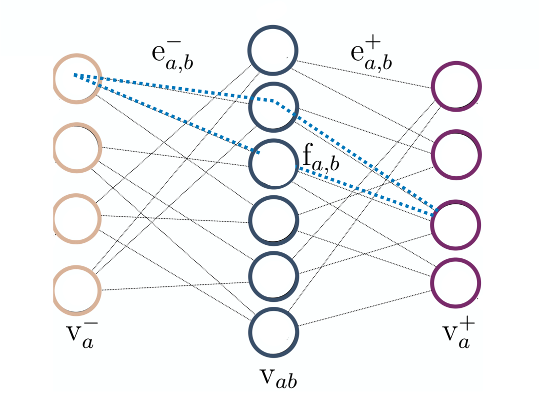

Figure 4.9: Two-dimensional representation of the internal component of the two-complex (see fig. 4.5 for comparison).

This construction automatically defines the orientation of every element of the two-complex. The structure of the vertices and internal edges of the two-complex reproduces the structure of the past (or future) part of the graph Γ. This is depicted in fig. 4.9, using for the vertices the same color codes used for the nodes.

The boundary edges are all "vertical": they connect the vertices in fig. 4.9 with the corresponding past and future nodes in fig. 4.5. All the internal faces are "horizontal": one of them is depicted in figure fig. 4.9. All the boundary faces are "vertical" and they are of course in one-to-one correspondence with the links of the graph Γ. The one-skeleton of the two-complex is represented in fig. 4.10. Careful: in fig. 4.10 the dots of the upper and lower layers are nodes, while those of the intermediate layer are vertices. The past (lower) and the future (upper) layers are in fact the past and the future components of the boundary graph Γ in fig. 4.6. The intermediate layer represents the vertices and the internal edges of the two-complex.

The boundary edges $E^{t\epsilon}_a$ and E^t_{ab} can be recognized in fig. 4.10 as the edges connecting the internal component of the two-complex to both the past and the future components of the boundary. This construction completely specifies the one-skeleton of the two-complex $\mathcal{C}$.

The graphical representation of the boundary faces F^ϵ_a and $F^{t\epsilon}_{a,b}$ is easily

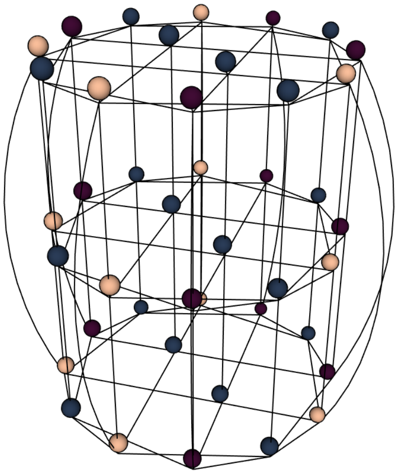

Figure 4.10: Three-dimensional representation of the one-skeleton of the two-complex $\mathcal{C}$. Notice that although the internal vertices and the boundary nodes are graphically depicted in the same way, they are two very distinct objects (the same applies also to edges and links).

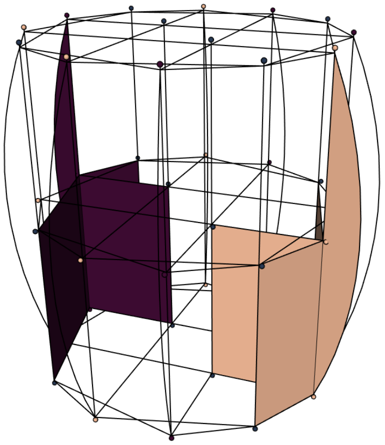

Figure 4.11: Graphical representation of the boundary faces (in red) $\mathrm{F}_{4,1}^{p+}$, $\mathrm{F}_{4,2}^{p+}$, $\mathrm{F}_{4,3}^{p+}$, F_{4}^{+} and (in brown) $\mathrm{F}_{4,1}^{p-}$, $\mathrm{F}_{4,2}^{p-}$, $\mathrm{F}_{4,3}^{p-}$, F_{4}^{-}.

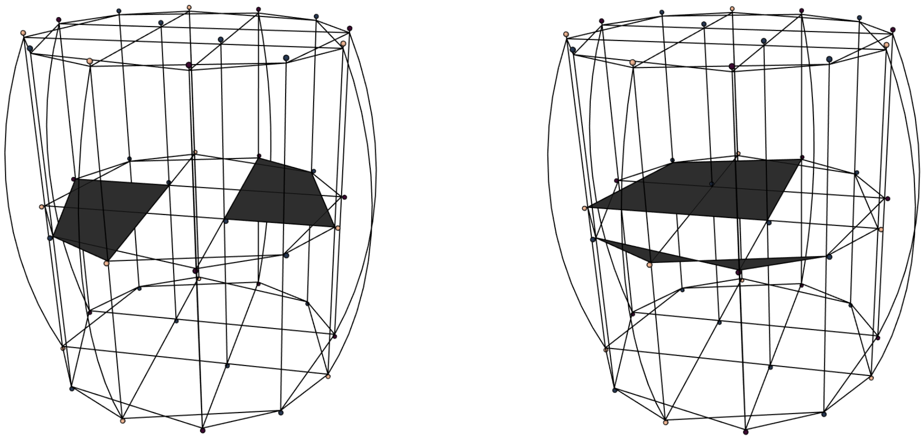

Figure 4.12: Graphical representation of the internal faces $\mathrm{f}_{1,4}$, $\mathrm{f}_{4,1}$ (left) and $\mathrm{f}_{1,2}$, $\mathrm{f}_{3,1}$ (right).

obtained using their definition given in section 4.4. Some of them are depicted in fig. 4.11.

The internal faces, although slightly more difficult to represent, can be found in the same way. Some of them are reported in fig. 4.12. The strange nature of their graphical representation (some of them intersect each other and some of them have strange shapes) is just a consequence of the fact that we are representing a four-dimensional object in three dimensions and it has no physical meaning.

The geometry of $\mathscr{B}$ is invariant under both rotations and the time reversal transformation that swaps Σ^p and Σ^f. The discretization reduces the rotational symmetry to a discrete tetrahedral symmetry, realized by an even permutation of the indices a, b, c, d. The time-reversal symmetry is realized by the swap of the indices p and f.

There is also a combinatorial symmetry defined by the exchange of the exterior and the interior, namely by the exchange of S_+ and S_-. This is realized in the two-complex by the invariance under the swap of the indices $+$ and $-$. This is however not a symmetry of the geometry we want to study, as S_+ and S_- have a different geometry: S_+ is larger.

4.5 Transition amplitude

Given the two-complex discretizing region $\mathscr{B}$, we are finally ready to compute the spin foam transition amplitude for the phenomenon. Following section 1.3.3, we assign group elements to the edges and the links of the two-complex in the following way:

$$\mathrm{L}^{\epsilon}_{a} \longleftrightarrow h^{\epsilon}_{a} \in \mathrm{SU}(2)\,;$$

$$\mathrm{L}^{t\epsilon}_{a,b} \longleftrightarrow h^{t\epsilon}_{a,b} \in \mathrm{SU}(2)\,;$$

$$\mathrm{E}^{t\epsilon}_{a} \longleftrightarrow g^{t\epsilon}_{a} \in \mathrm{SL}(2,\mathbb{C})\,;$$

$$\mathrm{E}^{t}_{ab} \longleftrightarrow g^{t}_{ab} \in \mathrm{SL}(2,\mathbb{C})\,;$$

$$\mathrm{e}^{\epsilon}_{a,b} \longleftrightarrow g^{\epsilon}_{a\to b}\,,\; g^{\epsilon}_{a\leftarrow b} \in \mathrm{SL}(2,\mathbb{C})\,.$$

The group element $g^{\epsilon}_{a\to b}$ is assigned to the oriented half-edge of $\mathrm{e}^{\epsilon}_{a,b}$ having source in the source of $\mathrm{e}^{\epsilon}_{a,b}$ and target in the middle of $\mathrm{e}^{\epsilon}_{a,b}$. The group element $g^{\epsilon}_{a\leftarrow b}$ is assigned to the oriented half-edge of $\mathrm{e}^{\epsilon}_{a,b}$ having source in the target of $\mathrm{e}^{\epsilon}_{a,b}$ and target in the middle of $\mathrm{e}^{\epsilon}_{a,b}$.

It is then straightforward to compute the covariant loop quantum gravity transition amplitude for the black-to-white hole transition by using the expressions reported in eqs. (1.97) to (1.99) applied to the specific two-complex defined above. The two-complex amplitude $W_{\mathcal{C}}$ expressed in terms of face amplitudes is

$$\begin{aligned} W_{\mathcal{C}}\big(h^{\epsilon}_{a}, h^{t\epsilon}_{a,b}\big) = \int_{\mathrm{SL}(2,\mathbb{C})} & \mathrm{d}g^{p\epsilon}_{a}\, \mathrm{d}g^{p}_{ab}\, \mathrm{d}g^{\epsilon}_{a\leftrightarrow b} \\ & \times \prod_{a\epsilon} A^{\epsilon}_{a}(h^{\epsilon}_{a}, g^{t\epsilon}_{a}) \prod_{ab} A_{a,b}(g^{+}_{a\leftrightarrow c}, g^{-}_{b\leftrightarrow c}) \\ & \times \prod_{tab} A^{t+}_{a,b}(h^{t+}_{a,b}, g^{t+}_{a}, g^{t}_{ab}, g^{+}_{a\leftrightarrow b}) \\ & \times \prod_{tab} A^{t-}_{a,b}(h^{t-}_{a,b}, g^{t-}_{a}, g^{t}_{cd}, g^{-}_{a\leftrightarrow b})\,. \end{aligned} \tag{4.44}$$

To regularize the expression in eq. (4.44) we have dropped the integration over one $\mathrm{SL}(2,\mathbb{C})$ element per vertex. We have chosen to drop the integrations over the $g_a^{f\epsilon}$ and g_{ab}^{f} variables. The integral is independent of these. The various face amplitudes read

$$A_a^{\epsilon}(h_a^{\epsilon}, g_a^{t\epsilon}) = \sum_j d_j \ \mathrm{Tr}\left[D^{(\gamma j,j)}\big((g_a^{f\epsilon})^{-1}\, g_a^{p\epsilon}\big) D^{(j)}\big(h_a^{\epsilon}\big)\right], \tag{4.45}$$

$$\begin{aligned} A_{a,b}(g^{+}_{a\leftrightarrow c}, g^{-}_{b\leftrightarrow c}) \overset{c\leq d}{=} \sum_j d_j \,\mathrm{Tr}\Big[& D^{(\gamma j,j)}\big((g^{+}_{a\to d})^{-1}\, g^{+}_{a\to c}\big)\, D^{(\gamma j,j)}\big((g^{+}_{a\leftarrow c})^{-1}\, g^{-}_{b\leftarrow d}\big) \\ & \times D^{(\gamma j,j)}\big((g^{-}_{b\to d})^{-1}\, g^{-}_{b\to c}\big) D^{(\gamma j,j)}\big((g^{-}_{b\leftarrow c})^{-1}\, g^{+}_{a\leftarrow d}\big)\Big], \end{aligned} \tag{4.46}$$

$$\begin{aligned} A^{t+}_{a,b}(h^{t+}_{a,b}, g_a^{t+}, g^{t}_{ab}, g^{+}_{a\leftrightarrow b}) = \sum_j d_j \ \mathrm{Tr}\Big[& D^{(\gamma j,j)}\big((g_a^{t+})^{-1}\, g^{+}_{a\to b}\big) \\ & \times D^{(\gamma j,j)}\big((g^{+}_{a\leftarrow b})^{-1}\ g^{t}_{ab}\big) D^{(j)}\big(h^{t+}_{a,b}\big)\Big], \end{aligned} \tag{4.47}$$

$$\begin{aligned} A^{t-}_{a,b}(h^{t-}_{a,b}, g_a^{t-}, g^{t}_{cd}, g^{-}_{a\leftrightarrow b}) = \sum_j d_j \ \mathrm{Tr}\Big[& D^{(\gamma j,j)}\big((g_a^{t-})^{-1}\, g^{-}_{a\to b}\big) \\ & \times D^{(\gamma j,j)}\big((g^{-}_{a\leftarrow b})^{-1}\ g^{t}_{cd}\big) D^{(j)}\big(h^{t-}_{a,b}\big)\Big]. \end{aligned} \tag{4.48}$$

The transition amplitude for the black-to-white hole transition is then given by

$$\langle W_{\mathcal{C}} | \psi_{\mathrm{BW}} \rangle = \int_{\mathrm{SU}(2)} \mathrm{d}h_a^{\epsilon}\, \mathrm{d}h^{t\epsilon}_{a,b} W_{\mathcal{C}}(h_a^{\epsilon}, h^{t\epsilon}_{a,b})\ \psi_{\mathrm{BW}}(h_a^{\epsilon}, h^{t\epsilon}_{a,b}), \tag{4.49}$$

where $|\psi_{\mathrm{BW}}\rangle \in \mathcal{H}_\Gamma$ is the extrinsic coherent state peaked on the classical boundary geometry of the black-to-white hole transition defined in section 4.3.2. This explicitly gives the transition amplitude W for the process as a function of the four geometric parameters $(m, r_\pm, v)$:

$$W = W(m, r_\pm, v). \tag{4.50}$$

This transition amplitude can then be studied to investigate the quantum physics of region $\mathscr{B}$. As transition amplitudes in quantum gravity are generally not normalizable [141, 142], the amplitude cannot be used to study the probability of the horizon tunneling scenario with respect to any other tentative scenario for the end of the life of a black hole. However, if we restrict our space of possibilities to all the different black-to-white hole spacetimes characterized by the different physical parameters $(m, r_\pm, v)$, then the amplitude in eq. (4.50) gives the relative likelihood of a transition within the space of the parameter considered. Namely, we can use the amplitude in eq. (4.50) to investigate for what combination of parameters $(m, r_\pm, v)$ is the black-to-white hole transition more likely to happen.

A visual representation of the transition amplitude in eqs. (4.44) to (4.48) constructed using the graphical calculus outlined e.g. in Perez [69] is given in fig. 4.13.

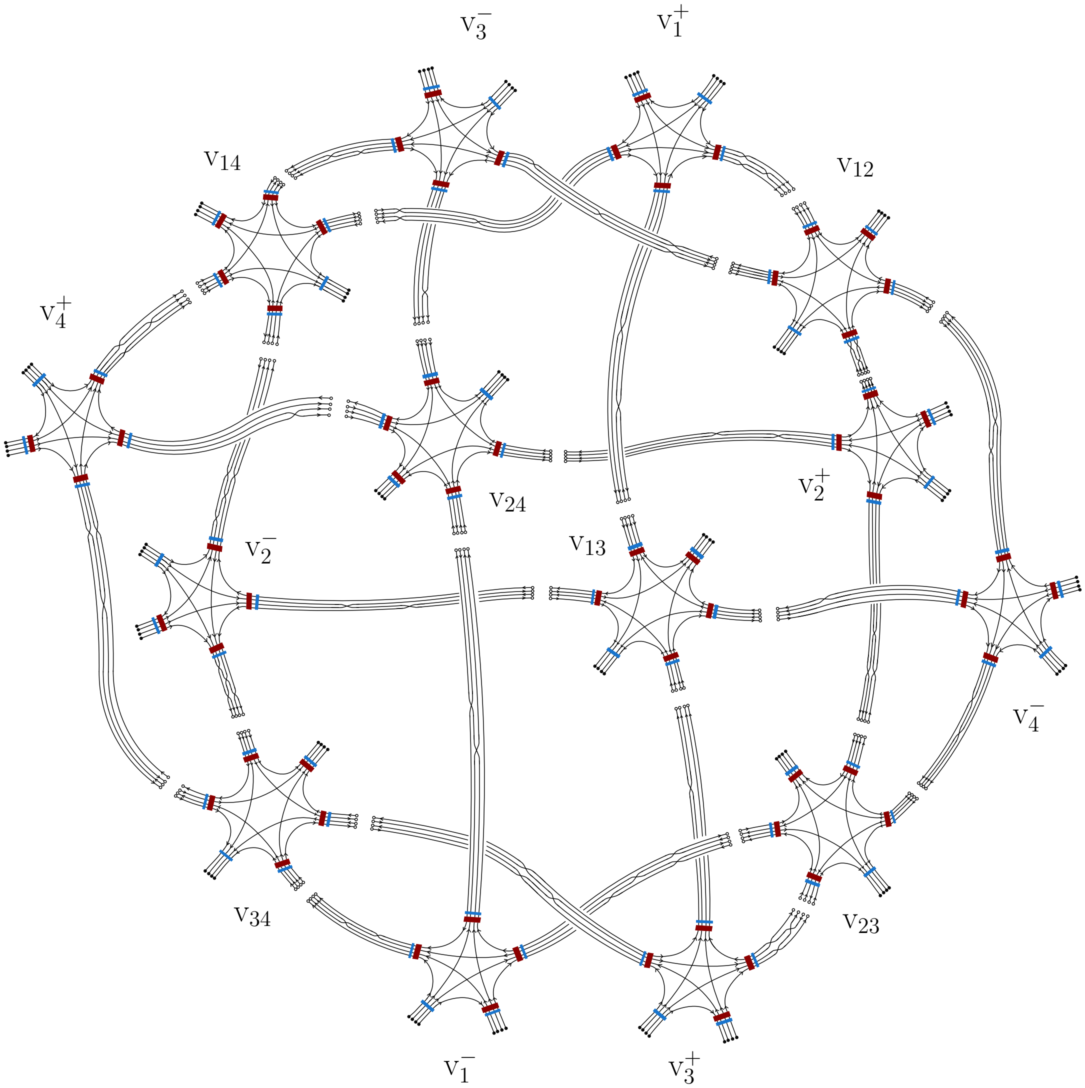

Figure 4.13: Visual representation of the transition amplitude in eqs. (4.44) to (4.48).

Chapter 5

Conclusions

The main objective of this thesis was the systematic investigation of a tentative scenario for the "end of the life" of a black hole: the black-to-white hole transition. This led to the construction of an explicit effective metric describing the entire black-to-white hole spacetime in chapter 3 and to the computation of the transition amplitude of the quantum tunneling of the black hole horizon in chapter 4. Surprisingly, it also leads to the construction of a global Kruskal-Szekeres coordinate chart for strongly spherically symmetric spacetimes in chapter 2.

These coordinates have been explicitly derived for the maximal extension of the Reissner-Nordström geometry, but their generalization to an arbitrary strongly spherically symmetric spacetime is straightforward. This coordinate chart provides a global generalization to the standard inner and outer Kruskal-Szekeres coordinates and a smooth generalization to the C^1 global Kruskal-Szekeres coordinate chart derived in Hamilton [24]. The existence of this coordinate chart, which is an interesting fact in and by itself, provides a simple and regular alternative to the standard coordinate charts for the Carter-Penrose diagram of strongly spherically symmetric spacetimes. The use of this coordinate chart to draw computer-generated Carter-Penrose diagrams proved incredibly useful in the investigation of the quantum-corrected Oppenheimer-Snyder model. The plot of curves of constant Painlevé-Gullstrand time coordinate in fig. 3.5 beautifully shows the discontinuity of the coordinate along the boundary of the star.

The black-to-white hole spacetime constructed in chapter 3 describes the collapse of a spherical pressure-less star, the subsequent formation of a black hole, the bounce of the star, the quantum transition of the black hole into a white hole, and the final expansion of the star out of the white hole. The entire geometry outside the star is given in a single global double-null coordinate chart. Far away from the quantum region the metric approximately satisfies the classical Einstein field equations. If the mass of the star is large compared to the Planck mass, this classical region includes a large portion of the interior of the black and white holes. In the quantum regions of spacetime outside the horizon tunneling region the metric satisfies quantum-corrected equations of motion derived using loop quantum gravity techniques.

The spacetime metric is determined by four parameters (m, $\mathcal{T}$, r_α, r_β). Only two of these parameters can be measured in the classical region: the mass m of the star and the global duration $\mathcal{T}$ of the process, from the collapse of the star into the black hole to its expansion from the white hole. These are the same parameters characterizing the classical black-to-white hole spacetime constructed in Haggard and Rovelli [43] and Christodoulou and D'Ambrosio [138]. Since the duration $\mathcal{T}$ is not determined by the initial conditions and the classical Einstein field equations, it must be determined (probabilistically) by the quantum theory as a function of m and $\hbar$, like the lifetime in a radioactive decay. The computation of the transition amplitude of the horizon tunneling region in chapter 4 is the first step in this direction. The parameters r_α and r_β instead determine the location and the size of the horizon tunneling region and they do not affect measurements at large distances.

The construction of an explicit effective metric for the black-to-white hole spacetime is a result of enormous importance. It allows us to concretely study the physics of the interior of the hole, which in previous investigations was always just considered as a quantum region with no metric attached to it. It has already been used in section 3.8 to qualitatively study the behavior of black and white hole horizons. Work is currently ongoing on a more systematic investigation of this behavior and on the overall physical picture of the horizon tunneling region emerging from this effective metric.

The evaporation process of the black hole has been neglected in the construction of this metric. The aim was in fact to give a first-approximation description of the quantum gravitational physics of a black hole spacetime, not a precise model of a realistic black hole. Taking into account the evaporation of the black hole will change the quantitative physics of the model, but not its qualitative physics. The quantum gravitational effects taken into account in the model are independent of the evaporation process and can be thus studied separately. Actually, the black-to-white hole spacetime constructed in chapter 3 provides a unique opportunity for the investigation of the evaporation process. It represents a background spacetime for the analysis of the evaporation process where quantum gravitational effects are already taken into account and the physics of the interior of the hole is known.

An important topic that was not covered in this thesis is the stability of black-to-white holes. The presence of inner horizons inside the hole makes it susceptible to two known instabilities: the *Cauchy horizon instability* [143, 144] and the *mass-inflation instability* [145, 146]. Consider for concreteness the Reissner-Nordström spacetime represented in fig. 2.4. Every inner horizon of the spacetime, which incidentally is always a *Cauchy horizon* of the initial value problem of the Einstein field equations, sits on either the same retarded time or the same advanced time coordinate of future null infinity of an exterior asymptotically flat region. This means that an observer crossing any inner horizon is hit by infinitely blue-shifted energy coming from outside the hole, effectively creating a singularity at the inner horizon. This instability, known as Cauchy horizon instability, afflicts most black hole spacetimes with inner horizons and it can generally be associated with the existence of event horizons. In the black-to-white hole spacetime constructed in chapter 3, where a collapsing star is present on one side and a unique asymptotically flat region, i.e. no event horizon, on the other, the Cauchy horizon instability does not apply.

A different instability, known as mass inflation instability, shows up as soon as ingoing and outgoing streams of matter perturbations are simultaneously present near the inner horizon. If this is the case, it can be shown that the *Misner-Sharp-Hernandez local mass* of spacetime will undergo a phase of exponential growth near the inner horizon drastically changing the spacetime geometry. While this phenomenon has been extensively studied in the context of non-singular black holes [147–149], all the analyses of the dynamical evolution of the geometry under this phenomenon has been performed using the (semi)classical Einstein field equations. In the black-to-white hole spacetime, the inner horizon is entirely contained in the quantum region of spacetime, where quantum-corrected equations of motion must be used to describe the geometry. It would thus be extremely interesting to study this phenomenon in the black-to-white hole context to see how it behaves in the presence of quantum gravity corrections.

Finally, the problems associated with a white hole spacetime discussed in section 1.2.3 need to be reevaluated in the context of the black-to-white hole spacetime. The problems with their physical interpretation were the presence of a curvature singularity in their past and the unclear process of matter formation from the singularity. Both of these issues are brilliantly taken care of in the black-to-white hole transition, which provides the only tentative astrophysical scenario for the formation of a physical white hole. The stability of these astrophysical white holes under the white hole instabilities discussed in section 1.2.3 strongly depends on the timescales of the black-to-white hole transition [121, 123, 150, 151], which are however left as free parameters in the spacetime constructed in chapter 3. To give a definitive answer to this issue it is then first necessary to understand better the physics of the horizon tunneling region.

This naturally brings us to the work presented in chapter 4, where the transition amplitude for the horizon tunneling region is explicitly computed using covariant loop quantum gravity. This transition amplitude is a function of the free parameters of spacetime affecting the geometry of the boundary of the horizon tunneling region, and it can be used to investigate which of the different scenarios defined by the different values of these parameters is the most likely to happen. The amplitude cannot however be used to study the relative probability of the black-to-white hole transition with respect to alternative scenarios for the end of the life of a black hole.

Covariant loop quantum gravity (see section 1.3.3) provides a clear framework to study this scenario. However, since the theory is properly defined in the discrete setting, the horizon tunneling region needed to be appropriately discretized in order to compute the transition amplitude. From a practical point of view, the discretization needs to be both sufficiently refined to capture the relevant degrees of freedom of the phenomenon and sufficiently simple for the transition amplitude to be explicitly computed and analyzed. The discretization constructed in chapter 4 is the simplest discretization that preserves the symmetries of the continuous geometry. Although the resulting two-complex is rather complicated, its high degree of symmetry allows the transition amplitude to be expressed in a remarkably compact way.

This notwithstanding, due to the severe complexity of spin foam amplitudes, the computed transition amplitude for the horizon tunneling region of the black-to-white hole spacetime is given by a convoluted multiple group integral which is hard to study analytically. On the other hand, the impressive recent developments in the numerical computation of spin foam amplitudes [152–160] will hopefully allow for a numerical investigation of the transition amplitude in the near future. A first step in this direction was recently taken in Han et al. [161].

Notably, the set of internal faces of the two-complex forms a *bubble*, that is they form together a surface without boundary with the topology of a two-sphere. In the absence of a cosmological constant in the theory, it can be shown that the presence of a bubble in a two-complex may in principle lead to a divergence in the corresponding transition amplitude [89]. It would thus be quite interesting to study the behavior of a bubble in a concrete physical application like the black-to-white hole transition. A naive counting of integration variables and constraints appearing in the large spin limit of spin foam amplitudes [162] appears to suggest that the transition amplitude computed in chapter 4 is in fact convergent. This conjecture might find proper grounding in the context of the recent work by Donà et al. [163], where several spin foam amplitudes expected to be divergent were numerically found to be convergent and the degree of convergence was found to depend on the ratio between the number of vertices and the number of internal faces in the two-complex.

In this thesis, the three quantum regions of the black-to-white hole spacetime were analyzed separately. In Christodoulou et al. [122, 138, 139] they were instead treated as a unique quantum region, with no metric attached to it, and a spin foam transition amplitude for this whole quantum region was computed.

The two-complex used to discretize the quantum region was considerably simpler than the one used here for the horizon tunneling region alone, mostly thanks to the simpler topology of the full quantum region. This allowed them to use the spin foam transition amplitude to give an estimate of the lifetime of the black hole in a black-to-white hole scenario where the evaporation process is neglected. This lifetime turned out to be much longer than the timescale of the evaporation process of the black hole, suggesting that Hawking radiation cannot be neglected for quantitative estimates and that the tunneling of the horizon takes place at the end of the evaporation. These results were recently confirmed numerically in Frisoni [164]. However, due to the use of a fairly coarse discretization for the quantum region, it is unclear whether the estimate is reliable. If the same results were to be obtained also from the analysis of the transition amplitude computed in chapter 4, then the evidence in favor of this timescale would be quite convincing. Rovelli and Vidotto [151] showed that if the tunneling of the horizon takes indeed place at the end of the evaporation process, then the resulting remnant would be stabilized by quantum gravity effects and it would have all the right properties to be a component of dark matter.

A precise and reliable estimate of the black-to-white hole transition timescales is very important to study the phenomenology of this scenario [165–170].

References

[1] F. Soltani. “Global Kruskal-Szekeres Coordinates for Reissner-Nordström Spacetime”. *Phys. Rev. D* **108** (2023), 124002. DOI: 10.1103/PhysRevD.108.124002. arXiv:2307.11026[gr-qc].

[2] M. Han, C. Rovelli, and F. Soltani. “Geometry of the Black-to-White Hole Transition within a Single Asymptotic Region”. *Phys. Rev. D* **107** (2023), 064011. DOI: 10.1103/PhysRevD.107.064011. arXiv:2302.03872[gr-qc].

[3] F. Fazzini, C. Rovelli, and F. Soltani. “Painlevé-Gullstrand Coordinates Discontinuity in the Quantum Oppenheimer-Snyder Model”. *Phys. Rev. D* **108** (2023), 044009. DOI: 10.1103/PhysRevD.108.044009. arXiv:2307.07797[gr-qc].

[4] F. D’Ambrosio, M. Christodoulou, P. Martin-Dussaud, C. Rovelli, and F. Soltani. “End of a Black Hole’s Evaporation”. *Phys. Rev. D* **103** (2021), 106014. DOI: 10.1103/PhysRevD.103.106014. arXiv:2009.05016[gr-qc].

[5] F. Soltani, C. Rovelli, and P. Martin-Dussaud. “End of a Black Hole’s Evaporation. II.” *Phys. Rev. D* **104** (2021), 066015. DOI: 10.1103/PhysRevD.104.066015. arXiv:2105.06876[gr-qc].

[6] R. Penrose. “Republication of: Conformal Treatment of Infinity”. *Gen. Rel. Grav.* **43** (2011), 901–922. DOI: 10.1007/s10714-010-1110-5.

[7] B. Carter. “Complete Analytic Extension of the Symmetry Axis of Kerr’s Solution of Einstein’s Equations”. *Phys. Rev.* **141** (1966), 1242–1247. DOI: 10.1103/PhysRev.141.1242.

[8] J. C. Schindler. “The Structure of Evaporating Black Holes”. PhD thesis (UC, Santa Cruz, 2019). URL: `https://inspirehep.net/files/682db2100e661af60fb9172f33ba7382`.

[9] V. P. Frolov, and I. D. Novikov. *Black Hole Physics. Basic Concepts and New Developments* (The Netherlands: Kluwer Academic Publishers, 1998).

[10] A. S. Eddington. “A Comparison of Whitehead’s and Einstein’s Formulæ”. *Nature* **113** (1924), 192–192. DOI: `10.1038/113192a0`.

[11] D. Finkelstein. “Past-Future Asymmetry of the Gravitational Field of a Point Particle”. *Phys. Rev.* **110** (1958), 965–967. DOI: `10.1103/PhysRev.110.965`.

[12] M. Walker. “Block Diagrams and the Extension of Timelike Two-Surfaces”. *Journal of Mathematical Physics* **11** (1970), 2280–2286. DOI: `10.1063/1.1665393`.

[13] J. C. Schindler, and A. Aguirre. “Algorithms for the Explicit Computation of Penrose Diagrams”. *Class. Quant. Grav.* **35** (2018), 105019. DOI: `10.1088/1361-6382/aabce2`. arXiv:`1802.02263[gr-qc]`.

[14] M. D. Kruskal. “Maximal Extension of Schwarzschild Metric”. *Phys. Rev.* **119** (1960), 1743–1745. DOI: `10.1103/PhysRev.119.1743`.

[15] G. Szekeres. “On the Singularities of a Riemannian Manifold”. *Publ. Math. Debrecen* **7** (1960), 285–301.

[16] H. Reissner. “Über Die Eigengravitation Des Elektrischen Feldes Nach Der Einsteinschen Theorie”. *Annalen Phys.* **355** (1916), 106–120. DOI: `10.1002/andp.19163550905`.

[17] G. Nordström. “On the Energy of the Gravitation Field in Einstein’s Theory”. *Koninklijke Nederlandse Akademie van Wetenschappen Proceedings Series B Physical Sciences* **20** (1918), 1238–1245.

[18] LIGO Scientific Collaboration and Virgo Collaboration. “Observation of Gravitational Waves from a Binary Black Hole Merger”. *Phys. Rev. Lett.* **116** (2016), 061102. DOI: 10.1103/PhysRevLett.116.061102. arXiv:1602.03837[gr-qc].

[19] E. H. T. Collaboration et al. “First M87 Event Horizon Telescope Results. I. The Shadow of the Supermassive Black Hole”. *Astrophys. J. Lett.* **875** (2019), L1. DOI: 10.3847/2041-8213/ab0ec7. arXiv:1906.11238[astro-ph.GA].

[20] E. H. T. Collaboration et al. “First Sagittarius A* Event Horizon Telescope Results. I. The Shadow of the Supermassive Black Hole in the Center of the Milky Way”. *Astrophys. J. Lett.* **930** (2022), L12. DOI: 10.3847/2041-8213/ac6674. arXiv:2311.08680[astro-ph.HE].

[21] E. Curiel. “The Many Definitions of a Black Hole”. *Nature Astron.* **3** (2019), 27–34. DOI: 10.1038/s41550-018-0602-1. arXiv:1808.01507[physics.hist-ph].

[22] V. Faraoni. “Evolving Black Hole Horizons in General Relativity and Alternative Gravity”. *Galaxies* **1** (2013), 114–179. DOI: 10.3390/galaxies1030114. arXiv:1309.4915[gr-qc].

[23] K. Schwarzschild. “On the Gravitational Field of a Mass Point According to Einstein’s Theory”. *Sitzungsber. Preuss. Akad. Wiss. Berlin (Math. Phys.)* **1916** (1916), 189–196. arXiv:physics/9905030.

[24] A. J. S. Hamilton. *General Relativity, Black Holes, and Cosmology.* 2021. URL: https://jila.colorado.edu/~ajsh/courses/astr5770_21/grbook.pdf.

[25] J. R. Oppenheimer, and H. Snyder. “On Continued Gravitational Contraction”. *Phys. Rev.* **56** (1939), 455–459. DOI: 10.1103/PhysRev.56.455.

[26] E. Poisson. *A Relativist’s Toolkit. The Mathematics of Black-Hole Mechanics* (Cambridge: Cambridge University Press, 2009). URL: https://doi.org/10.1017/CBO9780511606601.

[27] P. Painlevé. "La Mécanique Classique et La Théorie de La Relativité". *Comptes Rendus de l'Académie des sciences (Paris)* **173** (1921), 677–680.

[28] A. Gullstrand. "Allgemeine Lösung Des Statischen Einkörperproblems in Der Einsteinschen Gravitationstheorie". *Arkiv. Mat. Astron. Fys.* **16** (1922), 1–15.

[29] I. D. Novikov. "Delayed Explosion of a Part of the Fridman Universe, and Quasars". *Soviet Astronomy-AJ* **8** (1965), 857–863.

[30] D. M. Eardley. "Death of White Holes in the Early Universe". *Phys. Rev. Lett.* **33** (1974), 442–444. DOI: `10.1103/PhysRevLett.33.442`.

[31] S. K. Blau. "Dray–'t Hooft Geometries and the Death of White Holes". *Phys. Rev. D* **39** (1989), 2901. DOI: `10.1103/PhysRevD.39.2901`.

[32] A. Ori, and E. Poisson. "Death of Cosmological White Holes". *Physical Review D* **50** (1994), 6150–6157. DOI: `10.1103/PhysRevD.50.6150`.

[33] Y. B. Zel'dovich, I. D. Novikov, and A. A. Starobinsky. "Quantum Effects in White Holes". *Zh. Eksp. Teor. Fiz.* **66** (1974), 1897–1910.

[34] S. W. Hawking. "Black Hole Explosions?" *Nature* **248** (1974), 30–31. DOI: `10.1038/248030a0`.

[35] S. W. Hawking. "Particle Creation by Black Holes". *Commun. Math. Phys.* **43** (1975), 199–220. DOI: `10.1007/BF02345020`.

[36] M. Christodoulou, and C. Rovelli. "How Big Is a Black Hole?" *Phys. Rev. D* **91** (2015), 064046. DOI: `10.1103/PhysRevD.91.064046`. arXiv:`1411.2854[gr-qc]`.

[37] M. Christodoulou, and T. De Lorenzo. "Volume inside Old Black Holes". *Phys. Rev. D* **94** (2016), 104002. DOI: `10.1103/PhysRevD.94.104002`. arXiv:`1604.07222[gr-qc]`.

[38] R. M. Wald. *Quantum Field Theory in Curved Spacetime and Black Hole Thermodynamics* (Chicago: University of Chicago Press, 1994).

[39] P. Martin-Dussaud, and C. Rovelli. "Evaporating Black-to-White Hole". *Class. Quant. Grav.* **36** (2019), 245002. DOI: `10.1088/1361-6382/ab5097`. arXiv:`1905.07251 [gr-qc]`.

[40] S. D. Mathur. "The Information Paradox: A Pedagogical Introduction". *Class. Quant. Grav.* **26** (2009), 224001. DOI: `10.1088/0264-9381/26/22/224001`. arXiv:`0909.1038 [hep-th]`.

[41] T. Banks. "Lectures on Black Holes and Information Loss". *Nucl. Phys. B Proc. Suppl.* **41** (1995), 21–65. DOI: `10.1016/0920-5632(95)00430-H`. arXiv:`hep-th/9412131`.

[42] D. Marolf. "The Black Hole Information Problem: Past, Present, and Future". *Rept. Prog. Phys.* **80** (2017), 092001. DOI: `10.1088/1361-6633/aa77cc`. arXiv:`1703.02143 [gr-qc]`.

[43] H. M. Haggard, and C. Rovelli. "Black Hole Fireworks: Quantum-gravity Effects Outside the Horizon Spark Black to White Hole Tunneling". *Phys. Rev. D* **92**, 104020 (2015), 104020. DOI: `10.1103/PhysRevD.92.104020`. arXiv:`1407.0989 [gr-qc]`.

[44] S. W. Hawking. "Breakdown of Predictability in Gravitational Collapse". *Phys. Rev. D* **14** (1976), 2460–2473. DOI: `10.1103/PhysRevD.14.2460`.

[45] J. C. Schindler, A. Aguirre, and A. Kuttner. "Understanding Black Hole Evaporation Using Explicitly Computed Penrose Diagrams". *Phys. Rev. D* **101** (2020), 024010. DOI: `10.1103/PhysRevD.101.024010`. arXiv:`1907.04879 [gr-qc]`.

[46] W. G. Unruh, and R. M. Wald. "Information Loss". *Rept. Prog. Phys.* **80** (2017), 092002. DOI: `10.1088/1361-6633/aa778e`. arXiv:`1703.02140 [hep-th]`.

[47] D. N. Page. "Information in Black Hole Radiation". *Phys. Rev. Lett.* **71** (1993), 3743–3746. DOI: `10.1103/PhysRevLett.71.3743`. arXiv:`hep-th/9306083`.

[48] C. Rovelli. "Black Hole Entropy from Loop Quantum Gravity". *Phys. Rev. Lett.* **77** (1996), 3288–3291. DOI: 10.1103/PhysRevLett.77.3288. arXiv:gr-qc/9603063.

[49] C. Rovelli. "Black Holes Have More States than Those Giving the Bekenstein-Hawking Entropy: A Simple Argument". arXiv:1710.00218[gr-qc] (2017).

[50] J. Preskill. "Do Black Holes Destroy Information?" In: *Blackholes, Membranes, Wormholes and Superstrings: Proceedings of the International Symposium* (Singapore: World Scientific, 1993). Ed. by S. Kalara, and D. V. Nanopoulos. DOI: 10.1142/1814. arXiv:hep-th/9209058.

[51] S. Kazemian, M. Pascual, C. Rovelli, and F. Vidotto. "Diffuse Emission from Black Hole Remnants". *Class. Quant. Grav.* **40** (2023), 087001. DOI: 10.1088/1361-6382/acc232. arXiv:2207.06978[gr-qc].

[52] P. A. M. Dirac. "The Theory of Gravitation in Hamiltonian Form". *Proc. Roy. Soc. Lond. A* **246** (1958), 333–343. DOI: 10.1098/rspa.1958.0142.

[53] R. Arnowitt, S. Deser, and C. W. Misner. "Canonical Variables for General Relativity". *Phys. Rev.* **117** (1960), 1595–1602. DOI: 10.1103/PhysRev.117.1595.

[54] B. S. DeWitt. "Quantum Theory of Gravity. I. The Canonical Theory". *Phys. Rev.* **160** (1967), 1113–1148. DOI: 10.1103/PhysRev.160.1113.

[55] B. S. DeWitt. "Quantum Theory of Gravity. II. The Manifestly Covariant Theory". *Phys. Rev.* **162** (1967), 1195–1239. DOI: 10.1103/PhysRev.162.1195.

[56] B. S. DeWitt. "Quantum Theory of Gravity. III. Applications of the Covariant Theory". *Phys. Rev.* **162** (1967), 1239–1256. DOI: 10.1103/PhysRev.162.1239.

[57] C. Rovelli. "The Strange Equation of Quantum Gravity". *Class. Quant. Grav.* **32** (2015), 124005. DOI: 10.1088/0264-9381/32/12/124005. arXiv:1506.00927[gr-qc].

[58] A. Ashtekar. "New Hamiltonian Formulation of General Relativity". *Phys. Rev. D* **36** (1987), 1587–1602. DOI: 10.1103/PhysRevD.36.1587.

[59] A. Ashtekar. "New Variables for Classical and Quantum Gravity". *Phys. Rev. Lett.* **57** (1986), 2244–2247. DOI: 10.1103/PhysRevLett.57.2244.

[60] J. F. Barbero G. "Real Ashtekar Variables for Lorentzian Signature Space-Times". *Phys. Rev. D* **51** (1995), 5507–5510. DOI: 10.1103/PhysRevD.51.5507. arXiv:gr-qc/9410014.

[61] C. Rovelli. *Quantum Gravity*. Cambridge Monographs on Mathematical Physics (Cambridge, UK: Cambridge University Press, 2004). DOI: 10.1017/CBO9780511755804.

[62] T. Thiemann. *Modern Canonical Quantum General Relativity* (Cambridge: Cambridge University Press, 2007). URL: https://doi.org/10.1017/CBO9780511755682.

[63] C. Rovelli, and L. Smolin. "Spin Networks and Quantum Gravity". *Phys. Rev. D* **52** (1995), 5743–5759. DOI: 10.1103/PhysRevD.52.5743. arXiv:gr-qc/9505006.

[64] C. Rovelli, and L. Smolin. "Discreteness of Area and Volume in Quantum Gravity". *Nucl. Phys. B* **442** (1995), 593–622. DOI: 10.1016/0550-3213(95)00150-Q. arXiv:gr-qc/9411005.

[65] A. Ashtekar, and J. Lewandowski. "Quantum Theory of Geometry: I. Area Operators". *Class. Quant. Grav.* **14** (1997), A55–A82. DOI: 10.1088/0264-9381/14/1A/006. arXiv:gr-qc/9602046.

[66] A. Ashtekar, and J. Lewandowski. "Quantum Theory of Geometry II: Volume Operators". *Adv. Theor. Math. Phys.* **1** (1998), 388–429. DOI: 10.4310/ATMP.1997.v1.n2.a8. arXiv:gr-qc/9711031.

[67] R. P. Feynman, and A. R. Hibbs. *Quantum Mechanics and Path Integrals* (New York: McGraw-Hill Book Company, 1965).

[68] J. C. Baez. "An Introduction to Spin Foam Models of Quantum Gravity and BF Theory". *Lect. Notes Phys.* **543** (2000), 25–93. DOI: 10.1007/3-540-46552-9_2. arXiv:gr-qc/9905087.

[69] A. Perez. "The Spin-Foam Approach to Quantum Gravity". *Living Rev. Rel.* **16** (2013), 3. DOI: `10.12942/lrr-2013-3`. arXiv:`1205.2019[gr-qc]`.

[70] E. Alesci, T. Thiemann, and A. Zipfel. "Linking Covariant and Canonical Loop Quantum Gravity: New Solutions to the Euclidean Scalar Constraint". *Phys. Rev. D* **86** (2012), 024017. DOI: `10.1103/PhysRevD.86.024017`. arXiv:`1109.1290[gr-qc]`.

[71] T. Thiemann, and A. Zipfel. "Linking Covariant and Canonical LQG II: Spin Foam Projector". *Class. Quant. Grav.* **31** (2014), 125008. DOI: `10.1088/0264-9381/31/12/125008`. arXiv:`1307.5885[gr-qc]`.

[72] J. C. Baez. "Strings, Loops, Knots and Gauge Fields". In: *Knots and Quantum Gravity* (Oxford: Oxford University Press, 1994), pp. 133–168. Ed. by J. C. Baez. arXiv:`hep-th/9309067`. URL: `https://arxiv.org/abs/hep-th/9309067`.

[73] D. Oriti. "Spin Foam Models of Quantum Spacetime". PhD thesis (University of Cambridge, 2003). arXiv:`gr-qc/0311066`.

[74] S. Sen, S. Sen, J. C. Sexton, and D. H. Adams. "Geometric Discretization Scheme Applied to the Abelian Chern-Simons Theory". *Phys. Rev. E* **61** (2000), 3174–3185. DOI: `10.1103/PhysRevE.61.3174`. arXiv:`hep-th/0001030`.

[75] T. Regge. "General Relativity without Coordinates". *Nuovo Cim.* **19** (1961), 558–571. DOI: `10.1007/BF02733251`.

[76] C. Rovelli, and S. Speziale. "Geometry of Loop Quantum Gravity on a Graph". *Phys. Rev. D* **82** (2010), 044018. DOI: `10.1103/PhysRevD.82.044018`. arXiv:`1005.2927[gr-qc]`.

[77] J. Engle, R. Pereira, and C. Rovelli. "Loop-Quantum-Gravity Vertex Amplitude". *Phys. Rev. Lett.* **99** (2007), 161301. DOI: `10.1103/PhysRevLett.99.161301`. arXiv:`0705.2388[gr-qc]`.

[78] J. Engle, E. Livine, R. Pereira, and C. Rovelli. "LQG Vertex with Finite Immirzi Parameter". *Nucl. Phys. B* **799** (2008), 136–149. DOI: `10.1016/j.nuclphysb.2008.02.018`. arXiv:`0711.0146[gr-qc]`.

[79] W. Kamiński, M. Kisielowski, and J. Lewandowski. "Spin-Foams for All Loop Quantum Gravity". *Class. Quant. Grav.* **27** (2010), 095006. DOI: `10.1088/0264-9381/29/4/049502`. arXiv:`0909.0939[gr-qc]`.

[80] Y. Ding, M. Han, and C. Rovelli. "Generalized Spinfoams". *Phys. Rev. D* **83** (2011), 124020. DOI: `10.1103/PhysRevD.83.124020`. arXiv:`1011.2149[gr-qc]`.

[81] J. C. Baez, and J. W. Barrett. "Integrability for Relativistic Spin Networks". *Class. Quant. Grav.* **18** (2001), 4683–4700. DOI: `10.1088/0264-9381/18/21/316`. arXiv:`gr-qc/0101107`.

[82] J. Engle, and R. Pereira. "Regularization and Finiteness of the Lorentzian Loop Quantum Gravity Vertices". *Phys. Rev. D* **79** (2009), 084034. DOI: `10.1103/PhysRevD.79.084034`. arXiv:`0805.4696[gr-qc]`.

[83] F. D'Ambrosio. "Semi-Classical Holomorphic Transition Amplitudes in Covariant Loop Quantum Gravity". PhD thesis (Aix-Marseille Université, 2019). arXiv:`2001.04651[gr-qc]`.

[84] S. Holst. "Barbero's Hamiltonian Derived from a Generalized Hilbert-Palatini Action". *Phys. Rev. D* **53** (1996), 5966–5969. DOI: `10.1103/PhysRevD.53.5966`. arXiv:`gr-qc/9511026`.

[85] C. Rovelli, and T. Thiemann. "Immirzi Parameter in Quantum General Relativity". *Phys. Rev. D* **57** (1998), 1009–1014. DOI: `10.1103/PhysRevD.57.1009`. arXiv:`gr-qc/9705059`.

[86] A. Perez, and C. Rovelli. "Physical Effects of the Immirzi Parameter in Loop Quantum Gravity". *Phys. Rev. D* **73** (2006), 044013. DOI: `10.1103/PhysRevD.73.044013`. arXiv:`gr-qc/0505081`.

[87] F. Cianfrani, O. M. Lecian, M. Lulli, and G. Montani. *Canonical Quantum Gravity. Fundamentals and Recent Developments* (Singapore: World Scientific, 2014).

[88] S. Alexandrov, and P. Roche. “Critical Overview of Loops and Foams”. *Phys. Rept.* **506** (2011), 41–86. DOI: 10.1016/j.physrep.2011.05.002. arXiv:1009.4475[gr-qc].

[89] C. Rovelli, and F. Vidotto. *Covariant Loop Quantum Gravity: An Elementary Introduction to Quantum Gravity and Spinfoam Theory*. Cambridge Monographs on Mathematical Physics (Cambridge University Press, 2014). DOI: 10.1017/CBO9781107706910.

[90] B. Carter. “The Complete Analytic Extension of the Reissner-Nordström Metric in the Special Case $e^2 = m^2$”. *Physics Letters* **21** (1966), 423–424. DOI: 10.1016/0031-9163(66)90515-4.

[91] S. W. Hawking, and G. F. R. Ellis. *The Large Scale Structure of Space-Time* (Cambridge, UK: Cambridge University Press, 2023). DOI: 10.1017/CBO9780511524646.

[92] S. Chandrasekhar. *The Mathematical Theory of Black Holes* (Oxford: Oxford University Press, 1998).

[93] W. Israel. “New Interpretation of the Extended Schwarzschild Manifold”. *Phys. Rev.* **143** (1966), 1016–1021. DOI: 10.1103/PhysRev.143.1016.

[94] D. W. Pajerski, and E. T. Newman. “Trapped Surfaces and the Development of Singularities”. *J. Math. Phys.* **12** (1971), 1929. DOI: 10.1063/1.1665825.

[95] T. Klösch, and T. Strobl. “Explicit Global Coordinates for Schwarzschild and Reissner - Nordstrøm Solutions”. *Class. Quant. Grav.* **13** (1996), 1191–1200. DOI: 10.1088/0264-9381/13/5/029. arXiv:gr-qc/9507011.

[96] L. Modesto. “Disappearance of the Black Hole Singularity in Loop Quantum Gravity”. *Phys. Rev. D* **70** (2004), 124009. DOI: 10.1103/PhysRevD.70.124009. arXiv:gr-qc/0407097.

[97] A. Ashtekar, and M. Bojowald. “Black Hole Evaporation: A Paradigm”. *Class. Quant. Grav.* **22** (2005), 3349–3362. DOI: 10.1088/0264-9381/22/16/014. arXiv:gr-qc/0504029.

[98] M. Campiglia et al. “Loop Quantization of Sphericallysymmetric Midi-Superspaces: The Interior Problem”. *AIP Conf. Proc.* **977** (2008), 52–63. DOI: `10.1063/1.2902798`. arXiv:`0712.0817[gr-qc]`.

[99] R. Gambini, and J. Pullin. “Black Holes in Loop Quantum Gravity: The Complete Space-Time”. *Phys. Rev. Lett.* **101** (2008), 161301. DOI: `10.1103/PhysRevLett.101.161301`. arXiv:`0805.1187[gr-qc]`.

[100] A. Corichi, and P. Singh. “Loop Quantization of the Schwarzschild Interior Revisited”. *Class. Quant. Grav.* **33** (2016), 055006. DOI: `10.1088/0264-9381/33/5/055006`. arXiv:`1506.08015[gr-qc]`.

[101] J. Olmedo, S. Saini, and P. Singh. “From Black Holes to White Holes: A Quantum Gravitational Symmetric Bounce”. *Class. Quant. Grav.* **34** (2017), 225011. DOI: `10.1088/1361-6382/aa8da8`. arXiv:`1707.07333[gr-qc]`.

[102] A. Ashtekar, J. Olmedo, and P. Singh. “Quantum Transfiguration of Kruskal Black Holes”. *Phys. Rev. Lett.* **121** (2018), 241301. DOI: `10.1103/PhysRevLett.121.241301`. arXiv:`1806.00648[gr-qc]`.

[103] A. Ashtekar, J. Olmedo, and P. Singh. “Quantum Extension of the Kruskal Spacetime”. *Phys. Rev. D* **98** (2018), 126003. DOI: `10.1103/PhysRevD.98.126003`. arXiv:`1806.02406[gr-qc]`.

[104] J. Münch. “Effective Quantum Dust Collapse via Surface Matching”. *Class. Quant. Grav.* **38** (2021), 175015. DOI: `10.1088/1361-6382/ac103e`. arXiv:`2010.13480[gr-qc]`.

[105] C. Zhang, Y. Ma, S. Song, and X. Zhang. “Loop Quantum Schwarzschild Interior and Black Hole Remnant”. *Phys. Rev. D* **102** (2020), 041502. DOI: `10.1103/PhysRevD.102.041502`. arXiv:`2006.08313[gr-qc]`.

[106] W. C. Gan, N. O. Santos, F. W. Shu, and A. Wang. “Properties of the Spherically Symmetric Polymer Black Holes”. *Phys. Rev. D* **102** (2020), 124030. DOI: `10.1103/PhysRevD.102.124030`. arXiv:`2008.09664[gr-qc]`.

[107] J. B. Achour, S. Brahma, S. Mukohyama, and J. P. Uzan. "Towards Consistent Black-to-White Hole Bounces from Matter Collapse". *JCAP* **09** (2020), 020. DOI: `10.1088/1475-7516/2020/09/020`. arXiv:`2004.12977 [gr-qc]`.

[108] M. Han, and H. Liu. "Improved Effective Dynamics of Loop-Quantum-Gravity Black Hole and Nariai Limit". *Class. Quant. Grav.* **39** (2022), 035011. DOI: `10.1088/1361-6382/ac44a0`. arXiv:`2012.05729 [gr-qc]`.

[109] M. Han, and H. Liu. "Covariant $\bar{\mu}$-Scheme Effective Dynamics, Mimetic Gravity, and Non-Singular Black Holes: Applications to Spherical Symmetric Quantum Gravity and CGHS Model". arXiv:`2212.04605 [gr-qc]` (2022).

[110] K. Giesel, B. F. Li, and P. Singh. "Nonsingular Quantum Gravitational Dynamics of an Lemaître-Tolman-Bondi Dust Shell Model: The Role of Quantization Prescriptions". *Phys. Rev. D* **104** (2021), 106017. DOI: `10.1103/PhysRevD.104.106017`. arXiv:`2107.05797 [gr-qc]`.

[111] J. F. Barbero G., and A. Perez. "Quantum Geometry and Black Holes". In: *Loop Quantum Gravity: The First 30 Years* (WSP, 2017), pp. 241–279. Ed. by A. Ashtekar, and J. Pullin. DOI: `10.1142/9789813220003_0008`. arXiv:`1501.02963 [gr-qc]`.

[112] V. Husain, J. G. Kelly, R. Santacruz, and E. Wilson-Ewing. "Quantum Gravity of Dust Collapse: Shock Waves from Black Holes". *Phys. Rev. Lett.* **128** (2022), 121301. DOI: `10.1103/PhysRevLett.128.121301`. arXiv:`2109.08667 [gr-qc]`.

[113] V. Husain, J. G. Kelly, R. Santacruz, and E. Wilson-Ewing. "On the Fate of Quantum Black Holes". *Phys. Rev. D* **106** (2022), 024014. DOI: `10.1103/PhysRevD.106.024014`. arXiv:`2203.04238 [gr-qc]`.

[114] A. Ashtekar, and M. Bojowald. "Quantum Geometry and the Schwarzschild Singularity". *Class. Quant. Grav.* **23** (2006), 391–411. DOI: `10.1088/0264-9381/23/2/008`. arXiv:`gr-qc/0509075`.

[115] L. Modesto. "Loop Quantum Black Hole". *Class. Quant. Grav.* **23** (2006), 5587–5602. DOI: `10.1088/0264-9381/23/18/006`. arXiv:`gr-qc/0509078`.

[116] L. Modesto. "Black Hole Interior from Loop Quantum Gravity". *Adv. High Energy Phys.* **2008** (2008), 459290. DOI: `10.1155/2008/459290`. arXiv:`gr-qc/0611043`.

[117] N. Bodendorfer, F. M. Mele, and J. Münch. "Mass and Horizon Dirac Observables in Effective Models of Quantum Black-to-White Hole Transition". *Class. Quant. Grav.* **38** (2021), 095002. DOI: `10.1088/1361-6382/abe05d`. arXiv:`1912.00774 [gr-qc]`.

[118] A. Ashtekar, and J. Olmedo. "Properties of a Recent Quantum Extension of the Kruskal Geometry". *Int. J. Mod. Phys. D* **29** (2020), 2050076. DOI: `10.1142/S0218271820500765`. arXiv:`2005.02309 [gr-qc]`.

[119] N. Bodendorfer, F. M. Mele, and J. Münch. "Effective Quantum Extended Spacetime of Polymer Schwarzschild Black Hole". *Class. Quant. Grav.* **36** (2019), 195015. DOI: `10.1088/1361-6382/ab3f16`. arXiv:`1902.04542 [gr-qc]`.

[120] C. Rovelli, and F. Vidotto. "Planck Stars". *Int. J. Mod. Phys. D* **23** (2014), 1442026. DOI: `10.1142/S0218271814420267`. arXiv:`1401.6562 [gr-qc]`.

[121] T. De Lorenzo, and A. Perez. "Improved Black Hole Fireworks: Asymmetric Black-Hole-to-White-Hole Tunneling Scenario". *Phys. Rev. D* **93** (2016), 124018. DOI: `10.1103/PhysRevD.93.124018`. arXiv:`1512.04566 [gr-qc]`.

[122] M. Christodoulou, C. Rovelli, S. Speziale, and I. Vilensky. "Planck Star Tunneling Time: An Astrophysically Relevant Observable from Background-Free Quantum Gravity". *Phys. Rev. D* **94** (2016), 084035. DOI: `10.1103/PhysRevD.94.084035`. arXiv:`1605.05268 [gr-qc]`.

[123] E. Bianchi, M. Christodoulou, F. D'Ambrosio, H. M. Haggard, and C. Rovelli. "White Holes as Remnants: A Surprising Scenario for the End of a Black Hole". *Class. Quant. Grav.* **35**, 225003 (2018), 225003. DOI: 10.1088/1361-6382/aae550. arXiv:1802.04264[gr-qc].

[124] A. Rignon-Bret, and C. Rovelli. "Black to White Transition of a Charged Black Hole". *Phys. Rev. D* **105** (2022), 086003. DOI: 10.1103/PhysRevD.105.086003. arXiv:2108.12823[gr-qc].

[125] A. Perez. "No Firewalls in Quantum Gravity: The Role of Discreteness of Quantum Geometry in Resolving the Information Loss Paradox". *Class. Quant. Grav.* **32** (2015), 084001. DOI: 10.1088/0264-9381/32/8/084001. arXiv:1410.7062[gr-qc].

[126] A. Ashtekar, T. Pawlowski, and P. Singh. "Quantum Nature of the Big Bang". *Phys. Rev. Lett.* **96** (2006), 141301. DOI: 10.1103/PhysRevLett.96.141301. arXiv:gr-qc/0602086.

[127] I. Agullo, and A. Corichi. "Loop Quantum Cosmology". In: *Springer Handbook of Spacetime* (Berlin, Heidelberg: Springer, 2014), pp. 809–839. Ed. by A. Ashtekar, and V. Petkov. DOI: 10.1007/978-3-642-41992-8_39. arXiv:1302.3833[gr-qc].

[128] J. Lewandowski, Y. Ma, J. Yang, and C. Zhang. "Quantum Oppenheimer-Snyder and Swiss Cheese Models". *Phys. Rev. Lett.* **130** (2023), 101501. DOI: 10.1103/PhysRevLett.130.101501. arXiv:2210.02253[gr-qc].

[129] M. Bobula, and T. Paw\lowski. "Rainbow Oppenheimer-Snyder Collapse and the Entanglement Entropy Production". *Phys. Rev. D* **108** (2023), 026016. DOI: 10.1103/PhysRevD.108.026016. arXiv:2303.12708[gr-qc].

[130] A. Ashtekar, T. Pawlowski, and P. Singh. "Quantum Nature of the Big Bang: An Analytical and Numerical Investigation". *Phys. Rev. D* **73** (2006), 124038. DOI: 10.1103/PhysRevD.73.124038. arXiv:gr-qc/0604013.

[131] R. Gambini, J. Olmedo, and J. Pullin. “Spherically Symmetric Loop Quantum Gravity: Analysis of Improved Dynamics”. *Class. Quant. Grav.* **37** (2020), 205012. DOI: 10.1088/1361-6382/aba842. arXiv:2006.01513[gr-qc].

[132] J. G. Kelly, R. Santacruz, and E. Wilson-Ewing. “Effective Loop Quantum Gravity Framework for Vacuum Spherically Symmetric Space-Times”. *Phys. Rev. D* **102** (2020), 106024. DOI: 10.1103/PhysRevD.102.106024. arXiv:2006.09302[gr-qc].

[133] C. M. Bender, and S. A. Orszag. *Advanced Mathematical Methods for Scientists and Engineers I* (Springer, 1999). DOI: 10.1007/978-1-4757-3069-2.

[134] J. G. Kelly, R. Santacruz, and E. Wilson-Ewing. “Black Hole Collapse and Bounce in Effective Loop Quantum Gravity”. *Class. Quant. Grav.* **38** (2020), 04LT01. DOI: 10.1088/1361-6382/abd3e2. arXiv:2006.09325[gr-qc].

[135] V. Faraoni, and G. Vachon. “When Painlevé–Gullstrand Coordinates Fail”. *Eur. Phys. J. C* **80** (2020), 771. DOI: 10.1140/epjc/s10052-020-8345-4. arXiv:2006.10827[gr-qc].

[136] F. Fazzini, V. Husain, and E. Wilson-Ewing. “Shell-Crossings and Shock Formation during Gravitational Collapse in Effective Loop Quantum Gravity”. arXiv:2312.02032[gr-qc] (2023).

[137] H. M. Haggard, and C. Rovelli. “Quantum Gravity Effects around Sagittarius A*”. *Int. J. Mod. Phys. D* **25** (2016), 1644021. DOI: 10.1142/S0218271816440211. arXiv:1607.00364[gr-qc].

[138] M. Christodoulou, and F. D’Ambrosio. “Characteristic Time Scales for the Geometry Transition of a Black Hole to a White Hole from Spinfoams”. arXiv:1801.03027[gr-qc] (2018).

[139] M. Christodoulou, F. D’Ambrosio, and C. Theofilis. “Geometry Transition in Spinfoams”. arXiv:2302.12622[gr-qc] (2023).

[140] G. Lemaître. "L'Univers En Expansion". *Annales de la Société Scientifique de Bruxelles* **A53** (1933), 51–85.

[141] R. Oeckl. "A "General Boundary" Formulation for Quantum Mechanics and Quantum Gravity". *Phys. Lett. B* **575** (2003), 318–324. DOI: `10.1016/j.physletb.2003.08.043`. arXiv:`hep-th/0306025`.

[142] R. Oeckl. "General Boundary Quantum Field Theory: Foundations and Probability Interpretation". *Adv. Theor. Math. Phys.* **12** (2008), 319–352. DOI: `10.4310/ATMP.2008.v12.n2.a3`. arXiv:`hep-th/0509122`.

[143] M. Simpson, and R. Penrose. "Internal Instability in a Reissner-Nordstrom Black Hole". *Int. J. Theor. Phys.* **7** (1973), 183–197. DOI: `10.1007/BF00792069`.

[144] M. Dafermos. "Stability and Instability of the Cauchy Horizon for the Spherically Symmetric Einstein-Maxwell-Scalar Field Equations". *Ann. Math* **158** (2003), 875–928.

[145] E. Poisson, and W. Israel. "Internal Structure of Black Holes". *Phys. Rev. D* **41** (1990), 1796–1809. DOI: `10.1103/PhysRevD.41.1796`.

[146] A. J. S. Hamilton, and P. P. Avelino. "The Physics of the Relativistic Counter-Streaming Instability That Drives Mass Inflation inside Black Holes". *Phys. Rept.* **495** (2010), 1–32. DOI: `10.1016/j.physrep.2010.06.002`. arXiv:`0811.1926[gr-qc]`.

[147] R. Carballo-Rubio, F. Di Filippo, S. Liberati, C. Pacilio, and M. Visser. "On the Viability of Regular Black Holes". *JHEP* **07** (2018), 023. DOI: `10.1007/JHEP07(2018)023`. arXiv:`1805.02675[gr-qc]`.

[148] R. Carballo-Rubio, F. Di Filippo, S. Liberati, C. Pacilio, and M. Visser. "Inner Horizon Instability and the Unstable Cores of Regular Black Holes". *JHEP* **05** (2021), 132. DOI: `10.1007/JHEP05(2021)132`. arXiv:`2101.05006[gr-qc]`.

[149] C. Barceló, V. Boyanov, R. Carballo-Rubio, and L. J. Garay. “Classical Mass Inflation versus Semiclassical Inner Horizon Inflation”. *Phys. Rev. D* **106** (2022), 124006. DOI: 10.1103/PhysRevD.106.124006. arXiv:2203.13539[gr-qc].

[150] C. Barceló, R. Carballo-Rubio, and L. J. Garay. “Black Holes Turn White Fast, Otherwise Stay Black: No Half Measures”. *JHEP* **01** (2016), 157. DOI: 10.1007/JHEP01(2016)157. arXiv:1511.00633[gr-qc].

[151] C. Rovelli, and F. Vidotto. “Small Black/White Hole Stability and Dark Matter”. *Universe* **4** (2018), 127. DOI: 10.3390/universe4110127. arXiv:1805.03872[gr-qc].

[152] S. Speziale. “Boosting Wigner’s Nj-Symbols”. *J. Math. Phys.* **58** (2017), 032501. DOI: 10.1063/1.4977752. arXiv:1609.01632[gr-qc].

[153] P. Donà, and G. Sarno. “Numerical Methods for EPRL Spin Foam Transition Amplitudes and Lorentzian Recoupling Theory”. *Gen. Rel. Grav.* **50** (2018), 127. DOI: 10.1007/s10714-018-2452-7. arXiv:1807.03066[gr-qc].

[154] P. Donà, M. Fanizza, G. Sarno, and S. Speziale. “Numerical Study of the Lorentzian Engle-Pereira-Rovelli-Livine Spin Foam Amplitude”. *Phys. Rev. D* **100** (2019), 106003. DOI: 10.1103/PhysRevD.100.106003. arXiv:1903.12624[gr-qc].

[155] M. Han, Z. Huang, H. Liu, D. Qu, and Y. Wan. “Spinfoam on a Lefschetz Thimble: Markov Chain Monte Carlo Computation of a Lorentzian Spinfoam Propagator”. *Phys. Rev. D* **103** (2021), 084026. DOI: 10.1103/PhysRevD.103.084026. arXiv:2012.11515[gr-qc].

[156] F. Gozzini. “A High-Performance Code for EPRL Spin Foam Amplitudes”. *Class. Quant. Grav.* **38** (2021), 225010. DOI: 10.1088/1361-6382/ac2b0b. arXiv:2107.13952[gr-qc].

[157] P. Dona, and P. Frisoni. “How-to Compute EPRL Spin Foam Amplitudes”. *Universe* **8** (2022), 208. DOI: 10.3390/universe8040208. arXiv:2202.04360[gr-qc].

[158] P. Frisoni, F. Gozzini, and F. Vidotto. “Markov Chain Monte Carlo Methods for Graph Refinement in Spinfoam Cosmology”. *Class. Quant. Grav.* **40** (2023), 105001. DOI: 10.1088/1361-6382/acc5d6. arXiv:2207.02881 [gr-qc].

[159] P. Dona, M. Han, and H. Liu. “Spinfoams and High-Performance Computing”. In: (2023). DOI: 10.1007/978-981-19-3079-9_100-1. arXiv:2212.14396 [gr-qc].

[160] P. Donà, and P. Frisoni. “Summing Bulk Quantum Numbers with Monte Carlo in Spin Foam Theories”. *Phys. Rev. D* **107** (2023), 106008. DOI: 10.1103/PhysRevD.107.106008. arXiv:2302.00072 [gr-qc].

[161] M. Han, D. Qu, and C. Zhang. “Spin Foam Amplitude of the Black-to-White Hole Transition”. arXiv:2404.02796 [gr-qc] (2024).

[162] P. Donà, and S. Speziale. “Asymptotics of Lowest Unitary SL$(2, \mathbb{C})$ Invariants on Graphs”. *Phys. Rev. D* **102** (2020), 086016. DOI: 10.1103/PhysRevD.102.086016. arXiv:2007.09089 [gr-qc].

[163] P. Donà, P. Frisoni, and E. Wilson-Ewing. “Radiative Corrections to the Lorentzian Engle-Pereira-Rovelli-Livine Spin Foam Propagator”. *Phys. Rev. D* **106** (2022), 066022. DOI: 10.1103/PhysRevD.106.066022. arXiv:2206.14755 [gr-qc].

[164] P. Frisoni. “Numerical Approach to the Black-to-White Hole Transition”. *Phys. Rev. D* **107** (2023), 126012. DOI: 10.1103/PhysRevD.107.126012. arXiv:2304.02691 [gr-qc].

[165] A. Barrau, and C. Rovelli. “Planck Star Phenomenology”. *Phys. Lett. B* **739** (2014), 405–409. DOI: 10.1016/j.physletb.2014.11.020. arXiv:1404.5821 [gr-qc].

[166] A. Barrau, C. Rovelli, and F. Vidotto. “Fast Radio Bursts and White Hole Signals”. *Phys. Rev. D* **90** (2014), 127503. DOI: 10.1103/PhysRevD.90.127503. arXiv:1409.4031 [gr-qc].

[167] A. Barrau, B. Bolliet, F. Vidotto, and C. Weimer. “Phenomenology of Bouncing Black Holes in Quantum Gravity: A Closer Look”. *JCAP* **02** (2016), 022. DOI: `10.1088/1475-7516/2016/02/022`. arXiv:`1507.05424[gr-qc]`.

[168] A. Barrau, B. Bolliet, M. Schutten, and F. Vidotto. “Bouncing Black Holes in Quantum Gravity and the Fermi Gamma-Ray Excess”. *Phys. Lett. B* **772** (2017), 58–62. DOI: `10.1016/j.physletb.2017.05.040`. arXiv:`1606.08031[gr-qc]`.

[169] A. Barrau, K. Martineau, and F. Moulin. “A Status Report on the Phenomenology of Black Holes in Loop Quantum Gravity: Evaporation, Tunneling to White Holes, Dark Matter and Gravitational Waves”. *Universe* **4** (2018), 102. DOI: `10.3390/universe4100102`. arXiv:`1808.08857[gr-qc]`.

[170] F. Vidotto. “Quantum Insights on Primordial Black Holes as Dark Matter”. *PoS* **EDSU2018** (2018), 046. DOI: `10.22323/1.335.0046`. arXiv:`1811.08007[gr-qc]`.